

Homogeneous nucleation and droplet growth in the coexistence region of n-alkane/methane mixtures at high pressures

Citation for published version (APA):

Looijmans, K. N. H. (1995). *Homogeneous nucleation and droplet growth in the coexistence region of n-alkane/methane mixtures at high pressures*. [Phd Thesis 1 (Research TU/e / Graduation TU/e), Applied Physics and Science Education]. Technische Universiteit Eindhoven. <https://doi.org/10.6100/IR437238>

DOI:

[10.6100/IR437238](https://doi.org/10.6100/IR437238)

Document status and date:

Published: 01/01/1995

Document Version:

Publisher's PDF, also known as Version of Record (includes final page, issue and volume numbers)

Please check the document version of this publication:

- A submitted manuscript is the version of the article upon submission and before peer-review. There can be important differences between the submitted version and the official published version of record. People interested in the research are advised to contact the author for the final version of the publication, or visit the DOI to the publisher's website.
- The final author version and the galley proof are versions of the publication after peer review.
- The final published version features the final layout of the paper including the volume, issue and page numbers.

[Link to publication](#)

General rights

Copyright and moral rights for the publications made accessible in the public portal are retained by the authors and/or other copyright owners and it is a condition of accessing publications that users recognise and abide by the legal requirements associated with these rights.

- Users may download and print one copy of any publication from the public portal for the purpose of private study or research.
- You may not further distribute the material or use it for any profit-making activity or commercial gain
- You may freely distribute the URL identifying the publication in the public portal.

If the publication is distributed under the terms of Article 25fa of the Dutch Copyright Act, indicated by the "Taverne" license above, please follow below link for the End User Agreement:

www.tue.nl/taverne

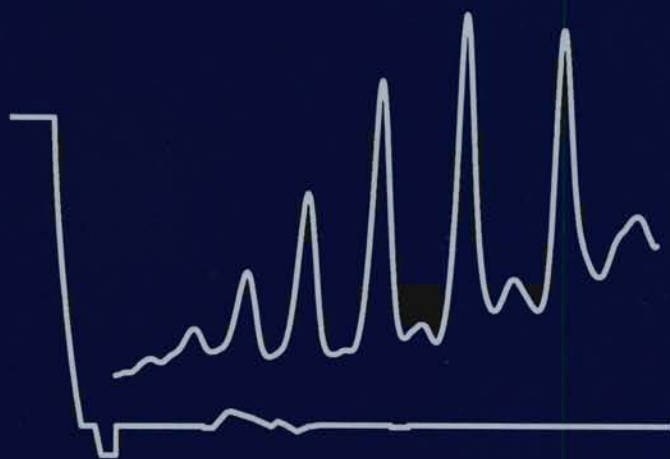
Take down policy

If you believe that this document breaches copyright please contact us at:

openaccess@tue.nl

providing details and we will investigate your claim.

Homogeneous nucleation and droplet growth in the coexistence region of *n*-alkane/methane mixtures at high pressures



K. N. H. Looijmans

Homogeneous nucleation and droplet growth in
the coexistence region of *n*-alkane/methane
mixtures at high pressures

Homogeneous nucleation and droplet growth in
the coexistence region of *n*-alkane/methane
mixtures at high pressures

PROEFSCHRIFT

ter verkrijging van de graad van doctor aan de
Technische Universiteit Eindhoven, op gezag van
de Rector Magnificus, prof.dr. J.H. van Lint,
voor een commissie aangewezen door het College
van Dekanen in het openbaar te verdedigen op
dinsdag 16 mei 1995 om 16.00 uur

door

Karel Nicolaas Helena Looijmans

geboren te Heeze

Dit proefschrift is goedgekeurd
door de promotoren:

Prof.dr.ir. M.E.H. van Dongen
en
Prof.dr.ir. P.P.J.M. Schram.

CONTENTS

| | | |
|----------|--|-----------|
| 1 | Introduction | 1 |
| 1.1 | Background | 1 |
| 1.2 | Homogeneous nucleation | 4 |
| 1.3 | Literature survey | 5 |
| 1.4 | Thesis overview | 7 |
| 2 | Binary Classical Nucleation Theory | 11 |
| 2.1 | Introduction | 11 |
| 2.2 | Binary homogeneous nucleation theory | 12 |
| 2.2.1 | Classical droplet model | 12 |
| 2.2.2 | Kinetics | 15 |
| 2.2.3 | Nucleation rate | 21 |
| 3 | Numerical calculations for n-nonane/methane | 25 |
| 3.1 | Introduction | 25 |
| 3.2 | A real gas model for ΔG | 25 |
| 3.3 | Results and discussion | 29 |
| 3.4 | Conclusions | 34 |
| 4 | Expansion wave tube | 37 |
| 4.1 | Nucleation pulse method | 37 |
| 4.2 | The shock tube | 39 |
| 4.3 | The nucleation pulse expansion tube | 45 |
| 4.3.1 | Gas dynamic aspects | 45 |
| 4.3.2 | Pressure and temperature in the nucleation pulse | 46 |
| 4.3.3 | Numerical simulation and experiment | 47 |
| 5 | Experimental method | 53 |
| 5.1 | Introduction | 53 |
| 5.2 | The nucleation experiment | 53 |
| 5.3 | Expansion tube construction | 53 |
| 5.3.1 | High pressure section and mixing circuit | 53 |
| 5.3.2 | Diaphragm construction | 55 |
| 5.3.3 | Low pressure section including local widening | 56 |
| 5.4 | Experimental techniques | 56 |
| 5.4.1 | Thermodynamic state | 57 |
| 5.4.2 | Optics | 58 |
| 5.4.3 | Mixture composition | 67 |

| | | |
|----------|---|------------|
| 5.5 | Experimental procedure | 72 |
| 6 | Experimental results | 77 |
| 6.1 | Introduction | 77 |
| 6.2 | Homogeneous nucleation and droplet growth of water vapour in nitrogen | 77 |
| 6.3 | Homogeneous nucleation and droplet growth of <i>n</i> -nonane | 83 |
| 6.4 | High pressure nucleation and droplet growth in hydrocarbon mixtures | 86 |
| 6.4.1 | Nucleation and droplet growth in <i>n</i> -nonane/methane | 87 |
| 6.4.2 | Nucleation and droplet growth in <i>n</i> -octane/methane | 92 |
| 7 | Conclusions and discussion | 97 |
| A | Physical properties | 101 |
| B | Random Choice Method | 107 |
| C | Unary nucleation | 111 |
| D | Tables of experimental data | 113 |
| | Symbols | 119 |
| | Summary | 123 |
| | Samenvatting | 125 |
| | Nawoord | 127 |
| | Curriculum Vitae | 128 |

Chapter 1

INTRODUCTION

1.1 Background

Homogeneous condensation is the vapour to liquid phase transition in the absence of foreign particles. The first stage of homogeneous condensation is the nucleation process. A number of vapour molecules come together forming a stable nucleus (critical nucleus), typically of the order of 100 molecules, that can grow further to a macroscopic droplet. This size of a nucleus is in between the scales on which a proper description on the basis of microscopic physics or macroscopic physics can be applied, and therefore very interesting from a fundamental point of view. Although subject of investigation for almost a century, the nature of the critical nucleus is still puzzling. Treating such a small particle as a macroscopic liquid drop, as it is done in the classical nucleation theory, seems rather questionable, whereas attempts to describe the nucleus by statistical mechanics appeared not to be successful either.

Studies on homogeneous nucleation concentrated so far on the transition from the vapour phase to the liquid phase for unary systems like water and *n*-nonane in particular, and binary systems consisting of, for example, aqueous solutions of alcohols and acid–water mixtures. Recently, also the nucleation of metal vapour in the phase transition into the solid state has become topic of research.

Homogeneous condensation plays a role in a wide variety of environmental and industrial processes. In the field of atmospheric sciences homogeneous nucleation is recognized as an important mechanism for droplet formation in the atmosphere. Most of the atmospheric aerosols originate from heterogeneous nucleation on existing nuclei such as ions, dust particles raised by wind, and volcanic dust particles. Investigations of atmospheric aerosols indicated that the production of a considerable part of the droplets (up to 25 % of the total aerosol mass present in the atmosphere) may be attributed to homogeneous condensation. In the upper atmosphere droplets are formed by binary, or heteromolecular, nucleation of sulphuric acid and water molecules.

On a regional scale and short time scale, cloud formation in the atmosphere of course is relevant to weather forecast. But also on a more global, and larger time scale the formation of concentrated sulphuric acid particles is of major importance. The atmospheric ozone depletion is partially attributed to chemical reactions catalysed by nitric acid–water droplets that were originated by condensation on the sulphuric acid–water particles. Because of the relevance to atmospheric processes, a lot of nucleation and condensation studies were dedicated to the sulphuric acid–water and nitric acid–water mixtures [e.g. Mirabel and Clavelin (1978), Wyslouzil

et al. (1991), and Rudolf (1994)].

Examples of homogeneous condensation in industrial processes are condensation of heavier hydrocarbons in natural gas, and the possible cleaning of smoke gas by separation of condensate. We will focus on the first example because it is most relevant to the present study. Natural gas consists mainly of methane (about 80 vol%, composition of Groningen natural gas), and furthermore of about 19 vol% nitrogen, and numerous other substances, mainly heavier hydrocarbons like pentane, nonane, benzene, etc. The phase behaviour of natural gas is determined to a large extent by these heavier hydrocarbons. When the gas mixture is brought into a supersaturated state, homogeneous condensation may take place as was shown by Muijtens *et al.* (1994). They subjected natural gas from initial pressures up to 50 bar to a continuous expansion in an expansion cloud chamber. When the expansion was strong enough dropwise condensation was observed. The measured onset points of condensation, called Wilson points, are shown in the pressure–temperature phase diagram of Fig. 1.1. In the initial state the gas is undersaturated, indicated by the saturation ratio S being smaller than unity¹. During the expansion, the saturation curve is crossed (here $S = 1$), and inside the coexistence curve a supersaturated state is obtained ($S > 1$). The measured Wilson points are situated in the coexistence region of the natural gas mixture above the critical temperature of the main component

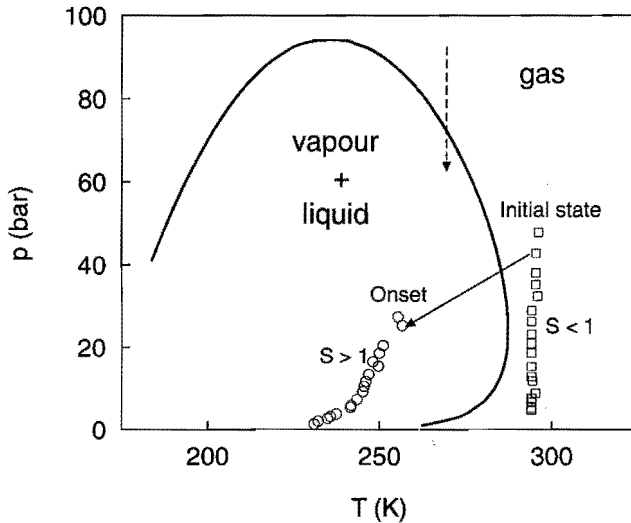


Figure 1.1: Pressure–temperature phase diagram of natural gas with condensation onsets measured by Muijtens *et al.* (1994). Solid curve, Coexistence curve of Groningen natural gas. Squares, state of the natural gas before the expansion. Circles, Measured onset points. Arrow, change of state by an adiabatic expansion. Dashed arrow, example of possible isothermal retrograde condensation.

methane. We will refer to this region as the supercritical region. From the strong deviation

¹For a unary system the saturation ratio is usually taken as the ratio of the actual vapour pressure, and the saturated vapour pressure that prevails over a flat liquid surface. In chapter 2 we shall introduce a definition of the saturation ratio that is applicable to the mixtures that we are dealing with.

from thermodynamic equilibrium of the condensation onset, they concluded that the droplets were formed by the homogeneous nucleation process.

The specific shape of the coexistence region in Fig. 1.1 is a result of real gas properties of the natural gas mixture. The influence of these real gas effects on homogeneous condensation has not been studied so far. The objective of this study is to describe experimentally as well as theoretically homogeneous nucleation in the supercritical region of *n*-alkane/methane mixtures taking into account the typical real gas properties.

For our investigations we chose a binary mixture exhibiting similar condensation behaviour in the supercritical region to that of natural gas. This avoids the complexity of the composition of the natural gas mixture, while the real gas effects approximately remain the same. The mixtures *n*-nonane/methane and *n*-decane/methane proved to be most applicable in our situation. The coexistence region of these mixtures largely overlap the coexistence region of natural gas.

In the mixtures mentioned, at a total pressure above a few bar, interactions between the molecules are no longer negligible, the resulting real gas effects reveal themselves in the condensation behaviour. In the gas phase, the solubility of the heavy hydrocarbon increases with pressure. This is expressed in the shape of the gas-liquid equilibrium curve corresponding to a fixed fraction of the heavy hydrocarbon. At a given temperature, depending on composition, the curve starts bending backwards, into the direction of the critical point of methane. This way it forms an envelope of a two-phase region. Bringing the gas mixture with given composition into a state inside this envelope, condensation will occur until gas-liquid equilibrium is achieved.

A consequence of the shape of the coexistence curve is the possibility of forming condensate by so-called retrograde condensation; i.e. when starting from initial conditions above the phase envelope, and reducing the pressure at constant temperature, the coexistence region is entered. Now, at a further reduction of pressure condensation will occur.

A way to obtain a supersaturated vapour to measure nucleation rates is to subject an initially undersaturated mixture to a sudden expansion. For nucleation studies this is often done in (piston) expansion chambers and shock tubes. When the expansion is fast enough, the change of thermodynamic state develops adiabatically and temperature falls with pressure, the vapour will become supersaturated, and homogeneous nucleation will start. We have built a specially designed pulse expansion tube, which actually is a shock tube, to study homogeneous nucleation at high pressures up to 100 bar². In shock tubes rapid and well defined waves can be generated to create a well shaped nucleation pulse, moreover, no moving parts are necessary, the complications in design and operation that would arise at high pressures can thus be avoided. A major drawback of the pulse expansion tube in comparison with expansion chambers is formed by the necessity of opening the tube to replace the diaphragm after each experiment, through which the purity of the test gas mixture could be influenced disadvantageously. The design and performance of the pulse expansion tube are the subjects of chapters 4 and 5.

²The term high pressure(s) is used throughout the thesis. It refers to the pressures that are typically for the coexistence region of the real gas mixtures studied, i.e. 10 – 100 bar.

1.2 Homogeneous nucleation

The first stage of any condensation process is the nucleation process. When foreign nuclei are present, such as dust particles, irregularities of walls and windows, nucleation can take place at these foreign nuclei very near the state of phase equilibrium. This process is called heterogeneous nucleation. Because in general the supersaturation of the vapour is low, the subsequent condensation proceeds slowly.

In contrast, we speak of homogeneous condensation when no foreign nuclei are present. This is a non-equilibrium process where condensation takes place in the form of droplets. Because first the condensation nuclei must be formed out of vapour molecules, a state of high supersaturation is required to obtain a droplet cloud. Since the saturation ratio is much larger than unity, the growth of droplets will be a fast process.

The following thermodynamic considerations explain why a state of (large) supersaturation is required for homogeneous nucleation to occur. In any equilibrium or undersaturated state of a gas, due to statistical density fluctuations, the gas molecules will form clusters of several molecules. Since the chemical potential of the liquid is higher than the chemical potential of the gas, these clusters tend to disintegrate again. So, a stable size distribution of clusters will be present which is very close to a Boltzmann distribution. When a vapour is in a supersaturated state, the chemical potential of the liquid is lower than the chemical potential of the vapour. In this case it would be favourable for the molecules to be in the liquid. Still, there is a barrier to take before droplets become stable. To create a droplet, also a droplet surface must be formed. The formation energy of a droplet surface is positive and therefore this will hamper the nucleation process.

In Fig. 1.2 the Gibbs free energy of droplet formation ΔG for a one component vapour is

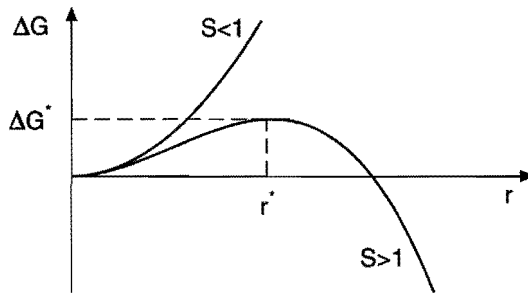


Figure 1.2: Gibbs free energy of droplet formation as a function of droplet radius.

given as a function of cluster size. In the undersaturated state ($S < 1$), ΔG is a monotonically rising function of droplet radius r , because the formation of a surface as well as the formation of bulk liquid require a positive amount of energy. When the vapour is supersaturated ($S > 1$), ΔG will form an energy barrier. In this case, the formation energy of the surface, which is proportional to the surface area of the cluster, and thus proportional to radius squared, is still positive. However, the energy gain by condensation into bulk liquid is proportional to the third power of the radius, and for large droplets this will always exceed the surface term, thus leading to an energy barrier.

The cluster with a size corresponding to the maximum of the ΔG function is called the critical cluster. This cluster is in unstable equilibrium with the vapour. Clusters that are larger than the critical cluster will grow further, while clusters smaller than the critical size tend to evaporate again. In case of multi-components, ΔG is a function of the number of molecules of all components present in the cluster, but the general idea of the energy barrier remains unchanged.

The nucleation rate, i.e. the rate at which droplets are formed per unit time and space, is determined by the number of critical clusters in the vapour formed by statistical fluctuations. Clearly, when a critical cluster collides with another vapour molecule it is over the top of the energy barrier and the droplet will grow further. In general terms the nucleation rate can be expressed as:

$$J = K \exp(-\Delta G^*/k_B T), \quad (1.1)$$

where T is the temperature, k_B Boltzmann's constant, and K a kinetic prefactor. The height of the energy barrier ΔG^* is a function of the supersaturation. When the supersaturation is increased, the energy barrier will become lower, and the critical cluster size will shift to smaller droplets. The nucleation rate appears to be extremely dependent on the supersaturation.

Several nucleation theories have been developed to predict the nucleation rate, for unary systems as well as for multi-component systems. The various theories are especially different in the models applied to calculate ΔG . We adopted the binary Classical Nucleation Theory for our theoretical calculations.

The extreme dependency of nucleation rate on supersaturation will be exploited in our experiment to obtain a nucleation pulse; this will be discussed in chapter 4. Measurements of nucleation rate as a function of supersaturation for different mixtures and at different conditions will be presented in chapter 6.

1.3 Literature survey

The evolution of homogeneous nucleation theory starts with the work of Volmer and Weber (1926), Becker and Döring (1935) and Zeldovich (1943). They developed the classical nucleation theory. The main assumption in the theory is the capillarity approximation; clusters of only 100 molecules or less are treated as macroscopic droplets with a surface tension corresponding to a flat liquid surface. The theory predicts the rate at which critical clusters are formed in a supersaturated vapour. Clusters larger in size than the critical cluster will grow to macroscopic droplets while clusters smaller than the size of a critical cluster tend to evaporate again. Since the introduction of the classical nucleation theory several attempts were made to improve the theory for two reasons: First, the capillarity approximation was considered to be rather unsatisfactory for such small clusters, and second, the success in comparison with experiments turned out to be limited to a restricted number of substances.

The Classical Nucleation Theory was extended to binary mixtures by Reiss (1950). The Gibbs formation free energy is here a function of the two components present in the mixture and the nucleus. The kinetic prefactor given by Reiss appeared not to be appropriate and was later refined by Stauffer (1976).

Several attempts to improve the classical theory have been made. Katz and Wiedersich (1977) modified the kinetic part of the theory in order to avoid the use of Maxwell demons.

Later, Girshic and Chiu (1990) focused on the consistency of the theory. By introducing an ad hoc correction they forced the Gibbs free energy to be zero for clusters of one molecule. Although these modifications seem to reduce the discrepancy between theory and experiment a little, they are still not considered to be satisfactory.

Another way to calculate the free energy of the cluster was proposed by Lothe and Pound (1962) on the basis of arguments from Statistical Mechanics. The success of this approach was limited. Nucleation rates differed by 12 orders of magnitude from the classical theory, but did not always coincide satisfactorily with experimental results.

Recently, some quasi-phenomenological theories were developed. It started with the model of Dillmann and Meier (1991), where the free energy was calculated on the bases of a statistical mechanical model of Fisher (1967). A Tolman length was introduced, and unknown parameters were related to properties of real gases, such as the second virial coefficient and expressions for pressure and density. The new theory proved to be very successful in predicting nucleation rates over a wide range of substances. Variations upon this approach were described by Kalikmanov and Van Dongen (1993), and Laaksonen *et al.* (1993).

Another interesting recent approach is the density functional theory of Zeng and Oxtoby (1991). However, for complicated molecules like *n*-nonane the required intermolecular potentials are not yet available with sufficient accuracy.

Fundamentals of homogeneous nucleation can be found in the book of Abraham (1974). An extensive review on the topic is given by Springer (1978). Recent developments in theory and experiment are covered in a review article by Oxtoby (1992).

The first quantitative experimental investigation of homogeneous nucleation was performed at the end of the 19th century by Wilson (1897). He measured the supersaturation at which droplets were formed out of water vapour in a carrier gas in an expansion cloud chamber. The first binary nucleation experiments were done by Flood (1934) on a water-ethanol mixture. He found fair agreement with a variation on the classical theory in a simple piston expansion chamber. Beside the expansion cloud chambers and piston cloud chambers, nucleation was studied with diffusion cloud chambers, invented by Franck and Hertz (1956), in expansion tubes (Wegener and Lundquist 1951), and supersonic nozzles (Wegener and Pouring 1964). An attractive feature of these latter two gasdynamic techniques is the high cooling rate that can be achieved. During several years a lot of substances were investigated, in particular water, *n*-nonane, other *n*-alkanes, and alcohols.

Until the mid 60's of this century, it was only possible to measure the Wilson points. The supersaturations reported, agreed fairly well with classical theory, mostly within 25%, but due to the enormous sensitivity of nucleation rate to supersaturation, the predictions for nucleation rates still could be very poor.

In 1965 Allard and Kassner (1965) developed a piston expansion chamber in which the initial expansion was followed by a small recompression. This recompression decreased the supersaturation again and therefore the nucleation process was quenched after a short period of time. Because a state of supersaturation was maintained at a lower level, the formed droplets kept on growing until they became of macroscopic size at which they could be detected photographically. This method is known as the nucleation pulse method. Since the number of droplets can be measured, and the duration of the nucleation pulse is known, the actual nucleation rate can be determined. Schmitt (1981) developed an improved piston expansion chamber in which

toluene, and ethanol (Schmitt *et al.* 1982) were studied. Wagner and Strey (1981) refined the nucleation pulse method by employing a two piston cloud chamber. They also measured droplet concentration and size by means of a light scattering method based on Mie theory.

The diffusion cloud chamber for nucleation studies was further refined by Katz and co-workers (Katz and Ostermeier 1967, Katz 1970). A temperature gradient maintains a stationary saturation profile from bottom to top plate. Still, in first instance only critical supersaturations were measured. In 1989 Hung *et al.* reported nucleation rates of *n*-nonane measured in a diffusion cloud chamber.

In 1983 Peters (1983) made the shock tube suitable for measuring nucleation rates by placing a constriction in the low pressure section of the tube. This generated a nucleation pulse in the high pressure section. This idea was further improved (Peters 1987) by moving the observation station to the endwall of the high pressure section. Droplets were detected by a 90° Mie scattering method. Nucleation rates and droplet growth rates of several vapours were reported (Peters and Paikert 1989). Good agreement between droplet growth rates and a droplet model of Gyarmathy (1982) was observed. Looijmans *et al.* (1993) improved the post nucleation pressure history by replacing the constriction by a local widening.

Some of the nucleation studies aimed at the effect of carrier gas on nucleation. In the shock tube study of Barschdorff (1975) nucleation of water in helium, argon and air did not show different carrier gas effects on critical supersaturation. Viisanen *et al.* (1993) measured nucleation rates as a function of supersaturation of water in Argon, Krypton, and Xenon. Also they did not find any influence of carrier gas nature on nucleation. Heist *et al.* (1994) reported a decrease of nucleation rate with total pressure of 1-propanol in helium and in hydrogen, measured in a diffusion cloud chamber at elevated pressures up to 40 bar. They also found that helium has a larger pressure effect on nucleation than hydrogen.

1.4 Thesis overview

The homogeneous nucleation and droplet growth in the mixtures *n*-nonane/methane and *n*-octane/methane at high pressures are subject of this thesis. A theoretical model on the basis of the classical nucleation theory is employed, and the results will be compared with those of high pressure experiments in a new nucleation pulse expansion tube.

In chapter 2 the binary classical nucleation theory will be treated extensively. An extension of the classical nucleation theory is described in chapter 3 to take into account the real gas properties affecting nucleation at high pressure. Numerical results of the new model will be shown.

Chapter 4 describes the experimental method adopted in this study. We developed an expansion tube based on the nucleation pulse method. The nucleation pulse method enables the separation of the nucleation stage from the droplet growth stage in homogeneous condensation. The gas dynamics involved in the nucleation pulse expansion tube will be described.

Chapter 5 deals with experimental set-up and procedure. The design and performance of the nucleation pulse expansion tube will be described. Much attention is paid to the optical techniques for measuring droplet size and concentration. Also a method to determine the initial mixture composition on the bases of the droplet growth will be described.

In chapter 6 the results of high pressure nucleation and droplet growth experiments are

reported. A comparison with the classical nucleation theory, and with a recently developed phenomenological nucleation theory by Kalikmanov and Van Dongen (1995) will be made. Experimental data concerning the composition of critical clusters will be specified.

Discussion and conclusions follow in chapter 7.

References

- ABRAHAM, F.F. 1974. *Homogeneous nucleation theory*. New York and London: Academic Press.
- ALLARD, E.F., & J.L. KASSNER, JR. 1965. New cloud-chamber method for determination of homogeneous nucleation rates. *J. Chem. Phys.* **42**(4):1401–1405.
- BARSCHDORFF, D. 1975. Carrier gas effects on homogeneous nucleation of water vapor in a shock tube. *Phys. Fluids* **18**(5):529–535.
- BECKER, R., & W. DÖRING. 1935. Kinetische Behandlung der Keimbildung in übersättigten Dämpfen. *Ann. Phys.* **5**(24):719–752.
- DILLMANN, A., & G.E.A. MEIER. 1991. A refined droplet approach to the problem of homogeneous nucleation from the vapor phase. *J. Chem. Phys.* **94**(5):3872–3884.
- FISHER, M.E. 1967. The theory of condensation and the critical point. *Physics* **3**:255–283.
- FLOOD, H. 1934. Tröpfchenbildung in übersättigten Äthylalkohol-Wasserdampf-gemischen. *Z. Phys. Chem. Abst. A* **170**:286–294.
- FRANCK, J.P., & H.G. HERTZ. 1956. Messung der kritischen übersättigung von Dämpfen mit der Diffusionsnebelkammer. *Z. Phys.* **143**:559–590.
- GIRSHICK, S.L., & C.-P. CHIU. 1990. Kinetic nucleation theory: A new expression for the rate of homogeneous nucleation from an ideal supersaturated vapor. *J. Chem. Phys.* **93**(2):1273–1277.
- GYARMATHY, G. 1982. The spherical droplet in gaseous carrier streams: review and synthesis. In *Multiphase science and technology, 1*. Washington: Hemisphere Publishing Corporation.
- HEIST, R.H., M. JANJUA, & J. AHMED. 1994. Effects of background gases on the homogeneous nucleation of vapors. 1. *J. Phys. Chem.* **98**(16):4443–4453.
- KALIKMANOV, V.I., & M.E.H. VAN DONGEN. 1993. Self-consistent cluster approach to the homogeneous kinetic nucleation theory. *Phys. Rev. E* **47**:3532–3539.
- KALIKMANOV, V.I., & M.E.H. VAN DONGEN. 1995. Quasi-one-component theory of homogeneous binary nucleation. *Phys. Rev. E* **51**:in press.
- KATZ, J.L. 1970. Condensation of a supersaturated vapor. I. The homogeneous nucleation of the *n*-alkanes. *J. Chem. Phys.* **52**(9):4733–4748.
- KATZ, J.L., & B.J. OSTERMEIER. 1967. Diffusion cloud-chamber investigation of homogenous nucleation. *J. Chem. Phys.* **47**(2):478–487.
- KATZ, J.L., & H. WIEDERSICH. 1977. Nucleation theory without Maxwell demons. *J. Colloid Interface Sci.* **61**(2):351–355.

- LAAKSONEN, A., M. KULMALA, & P.E. WAGNER. 1993. On the cluster composition in the classical binary nucleation theory. *J. Chem. Phys.* **99**(9):6832–6835.
- LOOIJMANS, K.N.H., P.C. KRIESEL, & M.E.H. VAN DONGEN. 1993. Gasdynamic aspects of a modified expansion–shock tube for nucleation and condensation studies. *Exp. Fluids* **15**:61–64.
- LOTHE, J., & G.M. POUND. 1962. Reconsiderations of nucleation theory. *J. Chem. Phys.* **36**:2080–2085.
- MIRABEL, P., & J.L. CLAVELIN. 1978. Experimental study of nucleation in binary mixtures: The nitric acid–water and sulfuric–water systems. *J. Chem. Phys.* **68**(11):5020–5027.
- MUITJENS, M.J.E.H., V.I. KALIKMANOV, M.E.H. v. DONGEN, A. HIRSCHBERG, & P.A.H. DERKS. 1994. On mist formation in natural gas. *Revue de l'Institut Français du Pétrole* **49**(1):63–72.
- OXTOBY, D.W. 1992. Homogeneous nucleation: theory and experiment. *J. Phys.: Condens. Matter* **4**:7627–7650.
- PETERS, F. 1983. A new method to measure homogeneous nucleation rates in shock tubes. *Exp. Fluids* **1**:143–148.
- PETERS, F. 1987. Condensation of supersaturated water vapor at low temperatures in a shock tube. *J. Phys. Chem.* **91**(10):2487–2489.
- PETERS, F., & B. PAIKERT. 1989. Experimental results on the rate of nucleation in supersaturated *n*-propanol, ethanol and methanol vapors. *J. Chem. Phys.* **91**(9):5672–5678.
- REISS, H. 1950. The kinetics of phase transitions in binary systems. *J. Chem. Phys.* **18**(6):840–848.
- RUDOLF, R. 1994. *Experimental investigation on condensation of supersaturated acid–water vapor mixtures by means of laser light scattering in a newly developed expansion chamber*. Ph.d. thesis, Universität Wien, Formal- und Naturwissenschaftlichen Fakultät.
- SCHMITT, J.L. 1981. Precision expansion cloud chamber for homogeneous nucleation studies. *Rev. Sci. Instrum.* **52**(11):1749–1754.
- SCHMITT, J.L., G.W. ADAMS, & R.A. ZALABSKY. 1982. Homogeneous nucleation of ethanol. *J. Chem. Phys.* **77**(4):2089–2097.
- SPRINGER, G.S. 1978. *Advances in heat transfer*. Vol. 14. Academic Press. chapter Homogeneous Nucleation, 281–345.
- STAUFFER, D. 1976. Kinetic theory of two–component (“heteromolecular”) nucleation and condensation. *J. Aerosol Sci.* **7**:319–333.
- VIISANEN, Y., R. STREY, & H. REISS. 1993. Homogeneous nucleation rates for water. *J. Chem. Phys.* **99**(6):4680–4692.
- VOLMER, M., & A. WEBER. 1926. Keimbildung in übersättigten Gebilden. *Z. Phys. Chem.* **119**:277–301.
- WAGNER, P.E., & R. STREY. 1981. Homogeneous nucleation rates of water vapor measured in a two-piston expansion chamber. *J. Phys. Chem.* **85**(18):2694–2700.

- WEGENER, P., & G. LUNDQUIST. 1951. Condensation of water vapor in the shock tube below 150°K. *J. Appl. Phys.* **22**(2):233.
- WEGENER, P.P., & A.A. POURING. 1964. Experiments on condensation of water vapor by homogeneous nucleation in nozzles. *Phys. Fluids* **7**(3):352-361.
- WILSON, C.R.T. 1897. condensation of water vapour in the presence of dustfree air and other gases. *Philos. Trans. R. Soc. London A* **189**:265-307.
- WYSLOUZIL, B.E., J.H. SEINFELD, & R.C. FLAGAN. 1991. Binary nucleation in acid-water systems. II. Sulfuric acid-water and a comparison with methanesulfonic acid-water. *J. Chem. Phys.* **94**(10):6842-6850.
- ZELDOVICH, YA.B. 1943. *Acta Physicochim. (URSS)* **18**.
- ZENG, X.C., & D.W. OXTOPY. 1991. Binary homogeneous nucleation theory for the gas-liquid transition: A nonclassical approach. *J. Chem. Phys.* **95**(8):5940-5947.

Chapter 2

BINARY CLASSICAL NUCLEATION THEORY

2.1 Introduction

Several nucleation theories have been developed since the twenties of this century. They all were based on the idea of an imperfect vapour consisting of single molecules and clusters of various sizes, that are present due to statistical density fluctuations. When the vapour is supersaturated some clusters become that large such that they will grow further to form macroscopic droplets. The oldest and still most frequently used theory is the Classical Nucleation Theory based on the Capillarity Approximation: clusters of several molecules are assumed to have the thermodynamic properties of macroscopic liquid droplets.

In this study the classical theory was chosen to predict nucleation behaviour of the gas mixture subject of investigation, and to compare the calculations with experimental results. Despite the somewhat unsatisfactory capillarity approximation for clusters of 10-100 molecules, it has proven to give reasonable agreement to experimentally obtained nucleation rates for a wide range of substances. The classical theory is rather easy to apply for numerical calculations. Furthermore, the fundamentals of the theory are quite understandable.

The original binary classical theory by Flood (1934) and Volmer (1939) was based on the homomolecular theory of fluctuations. In 1950 Reiss (1950) came to a full extension of the unary classical theory to a binary system, which is referred to as the standard theory. The free energy was calculated as a function of both components present in the cluster. The critical cluster was no longer top of a one-dimensional energy barrier, but it was located on the saddle point in a two-dimensional surface. Growth of clusters beyond the critical saddle point was assumed to follow a path of steepest descent. Later, the kinetic part was improved by Stauffer (1976) who stated that the "current" of clusters was not only determined by steepest descent, but by a combination of kinetics and the shape of the free energy surface.

Some controversy arose about the correct use of the Gibbs-Duhem relation in the standard theory (Renninger *et al.* 1981, Doyle 1981, Wilemski 1984). The discussion motivated Wilemski to formulate a revised version of the classical theory (1984, 1987, 1988). He introduced a droplet model in which a surface layer surrounds the liquid bulk of the droplet, which is based on the description of the gas-liquid interface by Gibbs (1961, 1982). The surface layer is allowed to have a composition different from the bulk. By applying the Gibbs-Duhem relation to the bulk, and the Gibbs absorption relation to the surface, a thermodynamic consistent droplet model was obtained. The composition of the bulk liquid is obtained by solving the Kelvin equations. Although the revised theory gives better results than the standard theory,

it still predicts some unphysical behaviour. For example, in a *n*-propanol/water mixture it predicts a multivalued onset curve of nucleation; a nucleation rate of $10^{11} \text{ cm}^{-3}\text{s}^{-1}$ is found at three different water activities at fixed *n*-propanol activity and temperature. A different droplet model was described by Flageollet–Daniel *et al.* (1983), who developed a lattice model for the cluster surface based on the interface treatment of Guggenheim (1967). A simplification of this model, called the explicit cluster model, was proposed by Laaksonen and Kulmala (1991). This model has appeared successful in predicting nucleation rates, despite it does not obey the Kelvin equations.

In the next sections the binary classical theory will be described based on the approaches by Wilemski for the thermodynamic droplet model, and by Stauffer for the kinetic part of the theory.

2.2 Binary homogeneous nucleation theory

The nucleation rate is the number of droplets formed per unit time and space. It is expressed in the following form:

$$J = K \cdot e^{-\Delta G^*/k_B T}. \quad (1.1)$$

K is a kinetic prefactor, ΔG^* in the exponential is the Gibbs free energy of formation of a critical droplet¹, k_B is Boltzmann's constant, and T is the temperature. The energy of formation $\Delta G(n_1, n_2)$ is a function of the numbers of particles of species 1 and 2 in the droplet. When the gas-vapour mixture is in a supersaturated state, the $\Delta G(n_1, n_2)$ plane exhibits a saddle point (fig. 2.1). The position of this saddle point is considered to represent the critical nucleus. The critical nucleus is in unstable equilibrium with the surrounding vapour, and the saddle point forms the lowest passage over an energy barrier. Clusters passing over this barrier will grow to macroscopic droplets. Different models have been employed to calculate ΔG . In CNT, Gibbs' capillarity approximation is used to describe the clusters on the basis of classical thermodynamics. In the next section the Wilemski approach to the classical droplet model is described.

2.2.1 Classical droplet model

In the macroscopic model of the revised classical theory of a droplet and surrounding binary vapour, the droplet consists of bulk liquid with numbers of bulk molecules n_1^l and n_2^l , and a surface layer with numbers of surface molecules n_1^s and n_2^s (see fig. 2.2). Bulk and surface are considered to be in thermodynamic equilibrium and the droplet is assumed to be incompressible.

¹ ΔG is the Gibbs free energy. Phase transitions generally take place at constant pressure and temperature. In a system with fixed p and T , chemical equilibrium is characterized by an extremum of the Gibbs free energy. When the extremum is a (local) minimum, the system is in a stable equilibrium state, when it is a maximum the system is in a meta-stable state. To find the critical droplet we therefore look for the maximum of ΔG . However, since the pressure in the droplet is larger than in the surrounding gas, the total free energy G is not the sum of the G 's of the subsystems droplet and gas phase. When it is assumed that the vapour pressure p before, and p' after the formation of the droplet are the same, then the Gibbs free energy of droplet formation equals the increase of the Helmholtz free energy ΔF . For summation of the Helmholtz free energy of the subsystems it is only required that T is held constant, p is allowed to be different. It is then possible to write: $\Delta G = F'(\text{vapour-droplet}) - F(\text{vapour})$ (Abraham 1974)

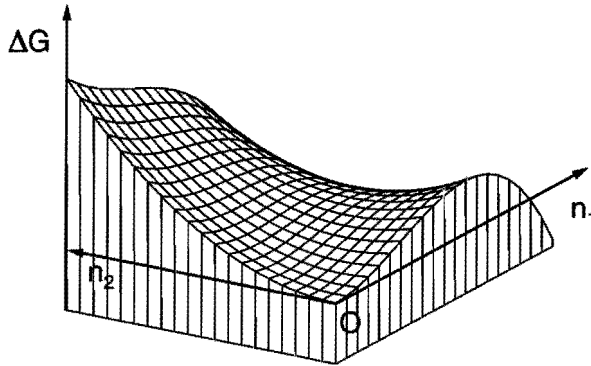


Figure 2.1: Gibbs free energy surface of binary clusters as a function of the numbers of molecules n_1 and n_2 . In this example component 2 is in a supercritical state. The Gibbs free energy of formation of a cluster containing only “2” molecules therefore increases monotonously. The other component shows for $n_2 = 0$ the energy barrier of a supersaturated vapour.

The number of surface molecules is an excess number, defined as $n^s = n - n^l - n^v$, where n is the total number of molecules in the system, and n^v is the number of molecules in the vapour. The excess molecules n_i^s do not contribute to the droplet volume V_l . The presence of the surface layer with surface area A in the droplet model, implicitly takes into account the effect of surface enrichment; the concentration of species 1 and 2 near the surface can differ from the interior composition. According to this droplet model, the free formation energy is (Wilemski 1984):

$$\Delta G = (p - p^l)V^l + \sigma A + \sum_{i=1,2} (\mu_i^l - \mu_i^v)n_i^l + \sum_{i=1,2} (\mu_i^s - \mu_i^v)n_i^s. \quad (2.1)$$

Chemical potentials μ_i^l and μ_i^v are evaluated at pressures p^l in the droplet and p^v of the surrounding vapour respectively. p is the total vapour pressure before the droplet was formed, and σ the surface tension. Because bulk liquid and surface are assumed to be in thermodynamic equilibrium, $\mu_i^s = \mu_i^l$, bulk and surface molecules can be taken together in Eq. (2.1):

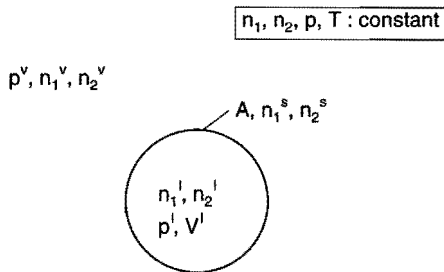


Figure 2.2: Droplet model in the revised binary classical theory with a gas-liquid surface layer of excess molecules according to Gibbs (1961).

$n_i^t = n_i^l + n_i^s$. If we define the difference in chemical potential between droplet and vapour as $\Delta\mu_i = \mu_i^l(p^l, T) - \mu_i^v(p^v, T)$, and furthermore assume that the formation of clusters does not lead to a change of vapour pressure p (i.e. $p^v = p$), then ΔG can be written as

$$\Delta G = (p^v - p^l)V^l + \sigma A + \sum_{i=1,2} \Delta\mu_i n_i^t. \quad (2.2)$$

The saddle point of this ΔG plane is determined by

$$\left. \frac{\partial \Delta G}{\partial n_i^t} \right|_{sp} = 0, \quad i = 1, 2. \quad (2.3)$$

Combining Eqs. (2.2) and (2.3) together with the Gibbs-Duhem relation for the bulk,

$$S^l dT - V^l dp^l + \sum_{i=1,2} n_i^l d\mu_i^l(p^l, T) = 0, \quad (2.4)$$

and the Gibbs adsorption equation for the surface,

$$S^s dT + A d\sigma + \sum_{i=1,2} n_i^s d\mu_i^s = 0, \quad (2.5)$$

we arrive at:

$$\Delta\mu_i = 0. \quad (2.6)$$

In deriving the last result, we used the Laplace relation $p^l = p^v + 2\sigma/r$, and the expressions for the volume and surface area of a spherical droplet, $V^l = \sum_i n_i^l v_i = \frac{4}{3}\pi r^3$ and $A = 4\pi r^2$.

Using the incompressible fluid approximation $\mu_i^l(p^l, T) = \mu_i^v(p^v, T) + v_i(p^l - p^v)$ in which v_i is the partial molecular volume of species i , one arrives at the so-called Gibbs-Thomson or Kelvin equations:

$$\Delta^* \mu_i + \frac{2\sigma v_i}{r} = 0. \quad (2.7)$$

In this equation $\Delta^* \mu_i = \mu_i^l(p^v, T) - \mu_i^v(p^v, T)$.

As stated by Wilemski (1987), all variables in these equations are functions of bulk composition only. Therefore, at the saddle point only the bulk composition can be obtained from these equations. The method described by Laaksonen *et al.* (1993) to calculate n_i^s and n_i^l can not be applied here because the surface molecules do not contribute to the droplet volume in this model. The Gibbs free energy of formation of a critical cluster at the saddle point follows from Eq. (2.2), with $\Delta\mu_i = 0$, because the critical cluster is in (unstable) equilibrium with the surrounding vapour:

$$\Delta G_{sp} = \frac{1}{3} \sigma A. \quad (2.8)$$

To obtain this result, again the Laplace relation, and the expressions for the droplet volume and surface area were substituted in Eq. (2.2).

2.2.2 Kinetics

In the preceding section an expression for the formation Gibbs free energy of a critical cluster was derived on the basis of the classical droplet model. As was explained in the introduction, the nucleation rate is proportional to a Boltzmann factor $\exp(-\Delta G^*/k_B T)$, multiplied by a kinetic prefactor K . This kinetic prefactor takes into account the deviation from a pure (equilibrium) Boltzmann distribution of the number of critical clusters in a supersaturated vapour, and the possibility that clusters of a size larger than the critical size still may evaporate.

The kinetics of binary nucleation was first considered by Reiss (1950). He only considered growth and evaporation taking place by addition and loss of single molecules, and he assumed the “trajectory” of the growing droplets through the saddle point of the ΔG function in (n_1, n_2) -space to follow the direction of steepest descent. Katz (1966) extended the kinetic factor of the unary kinetics to associated vapours, whereby cluster growth can take place by addition of small clusters as will be the case with methanol vapour. The kinetics of binary nucleation theory was modified by Stauffer (1976). He generalised the kinetic factor of Reiss by considering associated vapours, and demonstrated that the assumption of steepest descent was invalid. In this section an expression of the kinetic prefactor for binary nucleation is derived following Stauffer’s approach.

The microscopic–small clusters present in the binary gas mixture will contain molecules of both components. In theory, any configuration of n_1 molecules of species “1”, and n_2 molecules of species “2”, forming a (n_1, n_2) -cluster, is conceivable. The ensemble of all clusters forms a two-dimensional lattice in (n_1, n_2) -space. Continuous processes of collisions of clusters with single molecules, or, less likely, with other clusters, and dissociation of clusters change the size of the clusters involved. A (n_1, n_2) -cluster can be formed by coalescence of two smaller clusters, or by dissociation of a larger cluster. A (n_1, n_2) -cluster can disappear by coalescence with another cluster, or by dissociation into smaller clusters. These reactions will take place all over the (n_1, n_2) -lattice. If the gas mixture is in an equilibrium state, all the processes cancel, thus maintaining a stable size distribution of clusters.

In the case of a nucleation or condensation process the reactions do not cancel any more, thereby forming a net current $\vec{J} = \vec{J}_1 + \vec{J}_2$ over the lattice surface (Fig. 2.3). Our objective is to calculate this current in the neighbourhood of the (n_1, n_2) values corresponding to the saddle point in the ΔG surface, as this is considered to be related to the nucleation rate.

The change of the actual time dependent concentration of (n_1, n_2) -clusters $C(n_1, n_2)$ due to the coalescence and dissociation processes is given by the equation:

$$\frac{dC(n_1, n_2)}{dt} = \sum_i \sum_j \{ \beta_{ij} A(n_1 - i, n_2 - j) C(n_1 - i, n_2 - j) - \beta_{ij} A(n_1, n_2) C(n_1, n_2) - \gamma_{ij} A(n_1, n_2) C(n_1, n_2) + \gamma_{ij} A(n_1 + i, n_2 + j) C(n_1 + i, n_2 + j) \}. \quad (2.9)$$

In this equation β_{ij} is the impingement rate on a unit area of clusters of size (i, j) . When they behave like ideal gas molecules, $\beta_{ij} = C(i, j) \sqrt{k_B T / 2\pi m_{ij}}$, with m_{ij} the mass of the cluster. $A(n_1, n_2)$ is the surface area of a (n_1, n_2) -cluster, γ_{ij} gives the rate of evaporation per unit cluster surface area. The first and last term in the equation represent the formation of (n_1, n_2) -clusters, while the second and third term describe the destruction of these clusters (see fig 2.4).

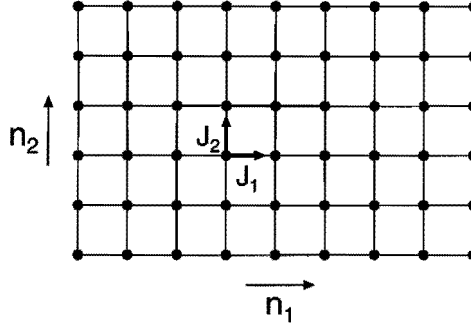


Figure 2.3: The (n_1, n_2) -lattice.

In our treatment we will take the condensation coefficient, which is the fraction of the colliding (i, j) -clusters that will stick to the (n_1, n_2) -cluster, to be unity. This assumption is usually made in the literature for the simple reason that real values are unknown. The evaporation coefficient γ_{ij} is unknown. It can be determined by referring to the equilibrium state. In equilibrium no net change of cluster concentration of any size takes place; the detailed balance condition requires that each forward process has to be balanced by its reverse process:

$$\gamma_{ij} A(n_1+i, n_2+j) c(n_1+i, n_2+j) = \beta_{ij} A(n_1, n_2) c(n_1, n_2). \quad (2.10)$$

In this equation $c(n_1, n_2)$ represents the equilibrium concentration of (n_1, n_2) -clusters, and it is expressed by the Boltzmann expression,

$$c(n_1, n_2) = N \exp(-\Delta G/k_B T), \quad (2.11)$$

where N is the number of single molecules in the gas mixture. Since we are dealing with a supersaturated state, this can not be a real equilibrium. After all, for clusters larger than the

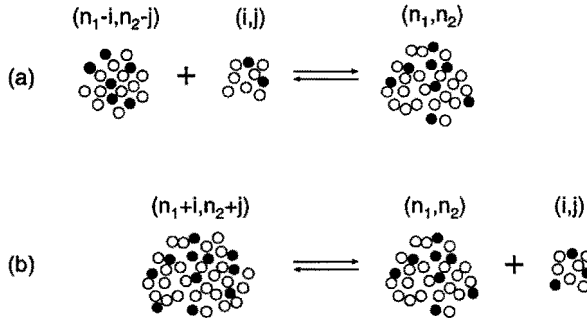


Figure 2.4: Formation of a (n_1, n_2) -cluster by coalescence (a) and dissociation (b).

critical size, the equilibrium concentration $c(n_1, n_2)$ is a function increasing with cluster size according to the Boltzmann expression, as ΔG decreases with cluster size. To force the system to remain in equilibrium, so-called Maxwell demons are introduced to remove all clusters above a certain size, larger than the critical size, from the system, dissociate them, and put them back as single molecules. This way a constrained equilibrium is obtained.

Substitution of γ_{ij} , obtained by applying the detailed balance condition Eq. (2.10) to the constraint equilibrium state, in Eq. (2.9) leads to:

$$\frac{dC(n_1, n_2)}{dt} = \sum_i \sum_j \beta_{ij} \left\{ A(n_1 - i, n_2 - j) c(n_1 - i, n_2 - j) \left[\frac{C(n_1 - i, n_2 - j)}{c(n_1 - i, n_2 - j)} - \frac{C(n_1, n_2)}{c(n_1, n_2)} \right] - A(n_1, n_2) c(n_1, n_2) \left[\frac{C(n_1, n_2)}{c(n_1, n_2)} - \frac{C(n_1 + i, n_2 + j)}{c(n_1 + i, n_2 + j)} \right] \right\}. \quad (2.12)$$

Cluster-cluster interactions are less likely than clusters growing by addition of single molecules or by addition of small other clusters containing only a few molecules. The change in size may then be regarded as continuous and the following expansion can be made for small i and j :

$$f(x - i, y - j) - f(x, y) = -i \frac{\partial f(x, y)}{\partial x} - j \frac{\partial f(x, y)}{\partial y} \quad (2.13)$$

Rewriting Eq. (2.12) with Eq. (2.13) yields:

$$\begin{aligned} \frac{dC(n_1, n_2)}{dt} = & - \sum_i \sum_j i \beta_{ij} \frac{\partial}{\partial n_1} \left\{ A(n_1, n_2) c(n_1, n_2) \left[\frac{C(n_1, n_2)}{c(n_1, n_2)} - \frac{C(n_1 + i, n_2 + j)}{c(n_1 + i, n_2 + j)} \right] \right\} \\ & - \sum_i \sum_j j \beta_{ij} \frac{\partial}{\partial n_2} \left\{ A(n_1, n_2) c(n_1, n_2) \left[\frac{C(n_1, n_2)}{c(n_1, n_2)} - \frac{C(n_1 + i, n_2 + j)}{c(n_1 + i, n_2 + j)} \right] \right\}. \end{aligned} \quad (2.14)$$

The concentration C is a function of time t , n_1 , and n_2 . Eq. (2.14) can be considered as a conservation law; write $\vec{J} = \vec{J}_1 + \vec{J}_2$, and $\nabla_n = \left(\frac{\partial}{\partial n_1}, \frac{\partial}{\partial n_2} \right)$, so

$$\frac{\partial C}{\partial t} + \nabla_n \cdot \vec{J} = 0, \quad (2.15)$$

with

$$\begin{aligned} J_1(n_1, n_2) &= - \sum_i \sum_j i \beta_{ij} A(n_1, n_2) c(n_1, n_2) \left[\frac{C(n_1, n_2)}{c(n_1, n_2)} - \frac{C(n_1 + i, n_2 + j)}{c(n_1 + i, n_2 + j)} \right] \\ J_2(n_1, n_2) &= - \sum_i \sum_j j \beta_{ij} A(n_1, n_2) c(n_1, n_2) \left[\frac{C(n_1, n_2)}{c(n_1, n_2)} - \frac{C(n_1 + i, n_2 + j)}{c(n_1 + i, n_2 + j)} \right]. \end{aligned}$$

Applying again the expansion of Eq. (2.13) the equations convert to

$$\begin{aligned} J_1(n_1, n_2) &= - \sum_i \sum_j i^2 \beta_{ij} A(n_1, n_2) c(n_1, n_2) \frac{\partial}{\partial n_1} \left(\frac{C(n_1, n_2)}{c(n_1, n_2)} \right) \\ &\quad - \sum_i \sum_j i j \beta_{ij} A(n_1, n_2) c(n_1, n_2) \frac{\partial}{\partial n_2} \left(\frac{C(n_1, n_2)}{c(n_1, n_2)} \right) \end{aligned}$$

$$\begin{aligned}
J_2(n_1, n_2) &= -\sum_i \sum_j ij \beta_{ij} A(n_1, n_2) c(n_1, n_2) \frac{\partial}{\partial n_1} \left(\frac{C(n_1, n_2)}{c(n_1, n_2)} \right) \\
&\quad - \sum_i \sum_j j^2 \beta_{ij} A(n_1, n_2) c(n_1, n_2) \frac{\partial}{\partial n_2} \left(\frac{C(n_1, n_2)}{c(n_1, n_2)} \right).
\end{aligned} \tag{2.16}$$

We now recovered the nucleation rate expression of Stauffer (1976),

$$\vec{J} = -c(n_1, n_2) \mathbf{R}(n_1, n_2) \cdot \nabla_n \left(\frac{C(n_1, n_2)}{c(n_1, n_2)} \right). \tag{2.17}$$

The two-dimensional tensor $\mathbf{R}(n_1, n_2)$ is the so called growth rate tensor:

$$\mathbf{R} = \begin{pmatrix} R_{11} & R_{12} \\ R_{21} & R_{22} \end{pmatrix}. \tag{2.18}$$

The elements of \mathbf{R} are given by:

$$\begin{aligned}
R_{11} &= \sum_i \sum_j i^2 \beta_{ij} A(n_1, n_2) \\
R_{12} &= \sum_i \sum_j ij \beta_{ij} A(n_1, n_2) = R_{21} \\
R_{22} &= \sum_i \sum_j j^2 \beta_{ij} A(n_1, n_2).
\end{aligned} \tag{2.19}$$

The off diagonal elements arise from incorporation of mixed clusters with “1” molecules as well as “2” molecules. When only interaction with monomers takes place, \mathbf{R} becomes diagonal, i.e. $R_{12} = R_{21} = 0$, and also $R_{11} = \beta_1 A(n_1, n_2)$, $R_{22} = \beta_2 A(n_1, n_2)$, with impingement rates of single molecules β_1 and β_2 .

The nucleation rate is given by the solution of Eq. (2.17), which is a time dependent equation. An analytic solution of this equation can be obtained by considering the steady state nucleation rate, which is of particular interest. A quasi steady state will be maintained as long as the nucleation process does not alter much the initial number of single molecules in the gas mixture. Then the (n_1, n_2) -cluster concentration is constant for each cluster size:

$$\frac{\partial C(n_1, n_2)}{\partial t} = 0. \tag{2.20}$$

Studies concerning the relaxation time required to attain the steady state, predict values of the order of microseconds (Abraham 1974). Since the time scales of our interest are much larger, but still small enough not to cope with vapour depletion, we shall assume the nucleation process to be quasi-steady.

The steady-state nucleation is described by the equations:

$$\nabla_n \cdot \vec{J} = 0, \text{ and } \vec{J} = -c(n_1, n_2) \mathbf{R}(n_1, n_2) \cdot \nabla_n \left(\frac{C(n_1, n_2)}{c(n_1, n_2)} \right), \tag{2.21}$$

subject to the boundary conditions:

$$\lim_{n_{1,2} \downarrow 0} \left(\frac{C}{c} \right) = 1; \quad \lim_{n_{1,2} \rightarrow \infty} \left(\frac{C}{c} \right) = 0. \quad (2.22)$$

The first boundary condition expresses the fact that for very small clusters the steady state solution will approximate the equilibrium distribution. The other boundary condition represents the removal of large clusters from the system to preserve the steady state. It is called the Szilard boundary condition. The steady-state solution is very insensitive to the cluster size at which the condition is applied.

When the inverse of \mathbf{R} exists, the identity $\nabla \times \nabla \phi = 0$, and the curl of Eqs. (2.21) lead to:

$$\nabla_n \times \left(\frac{1}{c} \mathbf{R}^{-1} \cdot \vec{J} \right) = 0. \quad (2.23)$$

Using the expression for the equilibrium distribution Eq. (2.11), this can be rewritten as

$$\nabla_n \times \left(\mathbf{R}^{-1} \cdot \vec{J} \right) = \left(\mathbf{R}^{-1} \cdot \vec{J} \right) \times \nabla_n (\Delta G / k_B T). \quad (2.24)$$

This equation has to be solved to obtain the direction of the cluster current or nucleation rate \vec{J} near the saddle point.

To be able to proceed we make the assumption that the direction of \vec{J} is constant in the neighbourhood of the saddle point. Also the variation of the kinetic matrix \mathbf{R} near the saddle point is neglected. Furthermore, for calculational convenience we assume \mathbf{R} to be diagonal, i.e. no ‘‘mixed’’ clusters are involved in the nucleation process. Stauffer (1976) makes plausible that this latter assumption does not have consequences for the final result of the derivation.

The ‘‘saddle point region’’ is defined as the region where the Taylor expansion up to the second order is a sufficient approximation:

$$\Delta G(n_1, n_2) - \Delta G(n_{1,sp}, n_{2,sp}) = m_1 D_{11} m_1 + m_1 D_{12} m_2 + m_2 D_{21} m_1 + m_2 D_{22} m_2. \quad (2.25)$$

Here $m_1 = n_1 - n_{1,sp}$ and $m_2 = n_2 - n_{2,sp}$, and the tensor \mathbf{D} contains the second derivatives of the free energy G evaluated at the saddle point (e.g. $2D_{12} = \partial^2 G / \partial n_1 \partial n_2 = 2D_{21}$). It is convenient to introduce a rotated coordinate system with the x - and y -axis parallel and perpendicular, respectively, to the direction of the saddle point current \vec{J}_{sp} :

$$x = m_1 \cos \phi + m_2 \sin \phi; \quad y = -m_1 \sin \phi + m_2 \cos \phi. \quad (2.26)$$

Since we assumed the direction of the saddle point current \vec{J}_{sp} to be constant in the saddle point region, the x -component becomes $J_x = J_{sp}$, whereas the y -component vanishes. In the steady state $\nabla_n \cdot \vec{J} = 0$, and therefore J_x must be independent of x , so $J_x(y)$ is only a function of y in the saddle point region. Now the following ‘‘Ansatz’’ is made for the saddle point region:

$$J_x = J_{sp} \exp(-W y^2); \quad J_y = 0, \quad (2.27)$$

with W a width factor that has to be determined.

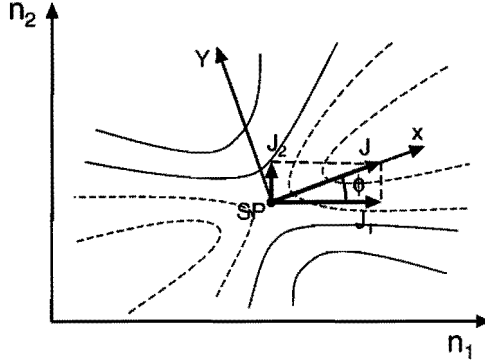


Figure 2.5: Rotated (x, y) -coordinate system with the origin in the saddle point SP of the ΔG surface. The curves correspond to constant levels of ΔG .

First, we will determine the angle ϕ . For this purpose we expand Eq. (2.24) into

$$\frac{\partial}{\partial m_1} (R_{22}^{-1} J_2) - \frac{\partial}{\partial m_2} (R_{11}^{-1} J_1) = R_{11}^{-1} J_1 \frac{\partial}{\partial m_2} \left(\frac{\Delta G}{k_B T} \right) - R_{22}^{-1} J_2 \frac{\partial}{\partial m_1} \left(\frac{\Delta G}{k_B T} \right). \quad (2.28)$$

Since \mathbf{R} is constant, $J_1 = J_{sp} e^{-W y^2 / k_B T} \cos \phi$, and $J_2 = J_{sp} e^{-W y^2 / k_B T} \sin \phi$; Eq. (2.28) can be rewritten as

$$\begin{aligned} & -R_{22}^{-1} J_{sp} e^{W y^2 / k_B T} (-2W y / k_B T) \sin^2 \phi - \\ & R_{11}^{-1} J_{sp} e^{W y^2 / k_B T} (-2W y / k_B T) \cos^2 \phi = \\ & R_{11}^{-1} J_{sp} e^{W y^2 / k_B T} \cos \phi (2m_1 D_{12} + 2m_2 D_{22}) / k_B T - \\ & R_{22}^{-1} J_{sp} e^{W y^2 / k_B T} \sin \phi (2m_1 D_{11} + 2m_2 D_{12}) / k_B T. \end{aligned}$$

After dividing by $2J_{sp} e^{-W y^2 / k_B T} / k_B T$ this yields

$$\begin{aligned} -R_{22}^{-1} W (-m_1 \sin \phi + m_2 \cos \phi) \sin^2 \phi - R_{11}^{-1} W (-m_1 \sin \phi + m_2 \cos \phi) \cos^2 \phi = \\ R_{11}^{-1} \cos \phi (m_1 D_{12} + m_2 D_{22}) - R_{22}^{-1} \sin \phi (m_1 D_{11} + m_2 D_{12}). \end{aligned}$$

This can be rewritten after the introduction of the dimensionless ratios $r = R_{22} / R_{11}$, $w = -W / D_{12}$, $d_1 = -D_{11} / D_{12}$, and $d_2 = -D_{22} / D_{12}$ as

$$\begin{aligned} -w (-m_1 \sin \phi + m_2 \cos \phi) \sin^2 \phi - w r (-m_1 \sin \phi + m_2 \cos \phi) \cos^2 \phi = \\ r \cos \phi (m_1 - m_2 d_2) - \sin \phi (-m_1 d_1 + m_2). \end{aligned}$$

After some rearrangements we obtain

$$\begin{aligned} (w \sin^3 \phi + w r \sin \phi \cos^2 \phi - r \cos \phi - d_1 \sin \phi) m_1 + \\ (-w \sin \phi \cos^2 \phi - w r \cos^3 \phi + r d_2 \cos \phi + \sin \phi) m_2 = 0. \end{aligned}$$

So, Eq. (2.24) has become of the form $F_1 m_1 + F_2 m_2 = 0$ which is supposed to be valid in the whole saddle point region. Since m_1 and m_2 vary independently, both F_1 and F_2 must

vanish:

$$\begin{aligned} F_1 &\equiv -w \sin^3 \phi - wr \sin \phi \cos^2 \phi + r \cos \phi + d_1 \sin \phi = 0 \\ F_2 &\equiv -wr \cos^3 \phi - w \sin^2 \phi \cos \phi + rd_2 \cos \phi + \sin \phi = 0. \end{aligned} \quad (2.29)$$

These equations are solved by

$$\begin{aligned} w &= (\sin \phi \cos \phi)^{-1} (\tan \phi + rd_2) / \tan \phi + r / \tan \phi \\ \tan \phi &= s + \sqrt{s^2 + r}, \end{aligned} \quad (2.30)$$

where $s = \frac{1}{2}(d_1 - rd_2)$.

The steepest descent approximation of Reiss (1950) would give $\cot 2\phi = (d_1 - d_2)/2$, as a result of $\partial D_{xx}/\partial \phi = 0$, with $D_{xx} = D_{11} \cos^2 \phi + 2D_{12} \cos \phi \sin \phi + D_{22} \sin^2 \phi$. This only corresponds to the solution of Eq. (2.30) if $r = 1$, i.e. the impingement rates of “1” and “2” molecules are exactly equal.

2.2.3 Nucleation rate

The direction of the nucleation current is known in the saddle point region, its magnitude is left to be determined. We return to Eq. (2.17).

After multiplying this equation by $\mathbf{R}^{-1} \left(\frac{1}{c} \right)$, and transforming to the (x, y) -coordinate system, we calculate the line integral of the x -component of the equation, over a path parallel to the x -axis, i.e. parallel to the saddle point current \vec{J}_{sp} , across the “mountain ridge” of the ΔG surface:

$$\int_0^{+\infty} (\mathbf{R}^{-1} \cdot \vec{J})_x \frac{1}{c(x, y)} dx = - \int_0^{+\infty} \frac{\partial}{\partial x} \left(\frac{C(x, y)}{c(x, y)} \right) dx = 1, \quad (2.31)$$

where $(\mathbf{R}^{-1} \cdot \vec{J})_x$ denotes to the x -component of the vector $(\mathbf{R}^{-1} \cdot \vec{J})$. The lower integral bound 0 corresponds to small clusters near the origin of the (n_1, n_2) -plane, and the upper bound ∞ refers to large clusters at the other side of the “mountain ridge”. These bounds correspond to the boundary conditions of Eq. (2.22). The result 1 of the integral can easily be understood by applying the boundary conditions to the second integral in Eq. (2.31).

Because of the appearance of the factor $\frac{1}{c}$ in the integral, the neighbourhood of the saddle point will have the largest contribution to the integral. Accordingly, the lower bound of the integral can be extended to minus infinity. Applying again the assumptions for the saddle point region, (\mathbf{R} is constant, and $\vec{J} = J_x \vec{e}_x$), Eq. (2.31) can be transformed into:

$$1 = (J_x/R_{av}) \int_{-\infty}^{+\infty} \frac{1}{c(x, y)} dx, \quad (2.32)$$

where an “average growth rate” R_{av} is introduced:

$$R_{av} = J_x / (\mathbf{R}^{-1} \cdot \vec{J})_x = \det(\mathbf{R}) / (R_{11} \sin^2 \phi + R_{22} \cos^2 \phi - 2R_{12} \sin \phi \cos \phi), \quad (2.33)$$

which results from transforming the inverse \mathbf{R}^{-1} matrix from the original (n_1, n_2) - to (x, y) -coordinates.

The factor W is given by $W = \det(\mathbf{D}^r)/D_{xx}^r = \det(\mathbf{D})/D_{xx}^r$. Writing $W' = -D_{xx}^r$, and keeping in mind that the first derivative of $\Delta G(x, y)$ with respect to x is equal to zero on the ridge, we obtain: $\Delta G(x, y) - \Delta G_{sp}(x, y) = Wy^2 - W'x^2$. After substituting this in Eq. (2.35), the Zeldovich factor can be evaluated easily:

$$Z = \int_{-\infty}^{+\infty} e^{-Wy^2/k_B T} dy / \int_{-\infty}^{+\infty} e^{-W'x^2/k_B T} dx = \left(\frac{W'}{W} \right)^{1/2}. \quad (2.39)$$

The final result $J_{tot} = R_{av} c_{sp} Z$ is the same result as the one found in one-component systems, but now an average growth rate is present:

$$R_{av} = \det(\mathbf{R}) / (R_{11} \sin^2 \phi + R_{22} \cos^2 \phi - 2R_{12} \sin \phi \cos \phi), \quad (2.40)$$

$$c_{sp} = N \exp(-\Delta G_{sp}/k_B T), \quad (2.41)$$

and

$$Z = -\frac{1}{2} \left(\partial^2 \Delta G(x, y) / \partial x^2 \right)_{sp} / (-\det \mathbf{D})^{1/2}. \quad (2.42)$$

Note: In the limit that the saddle point approaches either the n_1 or the n_2 axis, the kinetic prefactor does not turn into the kinetic prefactor of the unary theory. This error is due to the integration over the nucleation fluxes near the saddle point. If the pass over the saddle point is too steep, which will occur in the limit of unary condensation, this continuous treatment fails. A second problem in the limit of unary nucleation is the error introduced by setting the lower bound of the integration over y to $-\infty$ which cannot be appropriate here. Wilemski (1975) proposed an ad hoc correction to satisfy the limit. Shugard *et al.* (1974) dealt with this problem by not integrating over the nucleation fluxes near the saddle point, but keeping the summations in the calculation. They found a dependence of the nucleation rate on summation boundaries.

References

- ABRAHAM, F.F. 1974. *Homogeneous nucleation theory*. New York and London: Academic Press.
- DOYLE, G.J. 1981. Response to the comment on "Self-nucleation in the sulfuric acid-water system". *J. Chem. Phys.* **75**(3):1585-1586.
- FLAGEOLLET-DANIEL, C., J.P. GARNIER, & P. MIRABEL. 1983. Microscopic surface tension and binary nucleation. *J. Chem. Phys.* **78**(5):2600-2606.
- FLOOD, H. 1934. Tröpfchenbildung in übersättigten Äthylalkohol-Wasserdampf-gemischen. *Z. Phys. Chem. Abst. A* **170**:286-294.
- GIBBS, J.W. 1961. *The scientific papers of J.W. Gibbs*. Vol. 1. New York: Dover.
- GUGGENHEIM, E.A. 1967. *Thermodynamics*. Amsterdam: North-Holland.
- KATZ, J.L., H. SALTSBURG, & H. REISS. 1966. Nucleation in associated vapors. *J. Colloid and Interface Sci.* **21**:560-568.

- LAAKSONEN, A., & M. KULMALA. 1991. Explicit cluster model for binary nuclei in water-alcohol systems. *J. Chem. Phys.* **95**(9):6745-6748.
- LAAKSONEN, A., M. KULMALA, & P.E. WAGNER. 1993. On the cluster composition in the classical binary nucleation theory. *J. Chem. Phys.* **99**(9):6832-6835.
- REISS, H. 1950. The kinetics of phase transitions in binary systems. *J. Chem. Phys.* **18**(6):840-848.
- RENNINGER, R.G., F. CHARLES HILLER, & R.C. BONE. 1981. Comment on "Self-nucleation in the sulfuric acid-water system". *J. Chem. Phys.* **75**(3):1584-1585.
- ROWLINSON, J.S., & B. WIDOM. 1982. *Molecular theory of capillarity*. Oxford: Clarendon Press.
- SHUGARD, W.J., R.H. HEIST, & H. REISS. 1974. Theory of vapor phase nucleation in binary mixtures of water and sulfuric acid. *J. Chem. Phys.* **61**(12):5298-5305.
- STAUFFER, D. 1976. Kinetic theory of two-component ("heteromolecular") nucleation and condensation. *J. Aerosol Sci.* **7**:319-333.
- VOLMER, M. 1939. *Kinetik der Phasenbildung*. Dresden-Leipzig: Steinkopff.
- WILEMSKI, G. 1975. Binary nucleation. I. Theory applied to water-ethanol vapors. *J. Chem. Phys.* **62**(9):3763-3771.
- WILEMSKI, G. 1984. Composition of the critical nucleus in multicomponent vapor nucleation. *J. Chem. Phys.* **80**(3):1370-1372.
- WILEMSKI, G. 1987. Revised classical binary nucleation theory for aqueous alcohol and acetone vapors. *J. Phys. Chem.* **91**(10):2492-2498.
- WILEMSKI, G. 1988. Some issues of thermodynamic consistency in binary nucleation theory. *J. Chem. Phys.* **88**(8):5134-5136.

Chapter 3

NUMERICAL CALCULATIONS FOR n-NONANE/METHANE

3.1 Introduction

In chapter 2 the binary classical theory was outlined. The theory has been applied mainly to aqueous solutions, and mixtures of alcohols [e.g. Flageollet–Daniel *et al.* (1983), Mirabel and Clavelin (1978), Strey and Viisanen (1993), Zahoransky and Peters (1985)]. In these studies the gas phase was assumed to behave as an ideal gas. Non-ideal behaviour was present only in vapour activities not satisfying Raoult's law, while the vapour phase activities could be calculated on the basis of thermodynamic consistency equations, e.g. the van Laar equations. Furthermore, in these studies both components in the vapour phase were in a supersaturated state, far below their critical temperature.

This chapter describes an extension of the binary CNT. The Redlich-Kwong-Soave equation of state (RKS) has been implemented in the droplet model of CNT. In this way, both non-ideal behaviour of the gas phase and real gas properties of the vapour-liquid phase transition are dealt with. With the extended model nucleation rates can be calculated of mixtures at high pressures, and at conditions that one of the components is in a supercritical state. Numerical results are presented of the mixture *n*-nonane/methane, in the coexistence region at temperatures where retrograde condensation is possible.

3.2 A real gas model for ΔG

Calculation of the nucleation rate according to CNT requires a thermodynamic description for the gas and liquid mixture taking into account all real gas effects involved in the nucleation process.

To calculate ΔG of the critical nucleus, we have to tackle two problems. First, the thermodynamic properties of the two phases must be described by an equation of state (EOS). Then, by solving a linear combination of the Kelvin equations (2.7), the bulk composition of the critical droplet can be found:

$$v_2 \Delta^* \mu_1 - v_1 \Delta^* \mu_2 = 0. \quad (3.1)$$

For given p and T , all quantities in this equation are known functions of droplet bulk composition only, which follow from the EOS.

Second, it is not possible to evaluate mixture properties from the properties of the pure substances; methane is in a state in which no pure liquid methane can exist. Surface tension, which is a very important parameter determining the height of the energy barrier ΔG in Eq. (1.1), will thus be estimated by using an empirical correlation known as the Parachor method.

From several available equations of state we selected the Redlich-Kwong-Soave and the Lee-Kesler-Plöcker (LKP) equations (Reid *et al.* 1987), because they proved to be well applicable to alkanes. The RKS equation is of the cubic type and therefore relatively simple from a calculational point of view. The LKP equation of state is a transcendental one, thus computationally more complex. It is applicable, however, over a wider range of reduced temperatures. To compare both EOS to test their suitability to our application, we calculated the equilibrium molar volume of the liquid as a function of temperature and pressure. The molar volume is a very important parameter in our model because of its appearance in the Kelvin equations and in the surface tension correlation. The results obtained were compared with experimental data of Shipman *et al.* (1966). Although RKS is known for its poor prediction of liquid molar volume, results obtained by RKS when Peneloux' correction (Reid *et al.* 1987) was included turned out to be far better than LKP results in predicting the molar volumes (RKS, less than 0.8 % deviation from experimental data; LKP, up to 6 % deviation). For this reason, the RKS equation of state was used for all thermodynamic calculations throughout this work.

The RKS equation has the following form:

$$p = \frac{RT}{V_{RKS} - a} - \frac{b}{V_{RKS}(V_{RKS} + a)}, \quad (3.2)$$

where

$$a = \frac{0.08664RT_c}{p_c}$$

and

$$b = \frac{0.42748R^2T_c}{p_c} \left[1 + f(\omega) \left(1 - \sqrt{\frac{T}{T_c}} \right) \right]^2,$$

with

$$f(\omega) = 0.48 + 1.574\omega - 0.176\omega^2.$$

In these equations, R is the universal gas constant, V_{RKS} is the molar volume (subscript m is left out to avoid confusion with mixture properties in the remainder of this text), ω is Pitzer's acentric factor, and the subscript c refers to the critical point. For a mixture, a and b are evaluated from the pure component values using the mixing rules

$$a_m = \sum_i y_i a_i,$$

$$b_m = \sum_i \sum_j y_i y_j (b_i b_j)^{1/2} (1 - k_{ij}).$$

The quantities y_i in the above expressions denote the molar fractions of the components, both in the vapour and liquid phases. From now on, however, we will use x_i for the liquid molar fractions. In the last mixing rule, the interaction parameter k_{ij} is introduced. Its value is determined by a fit to experiments (Knapp *et al.* 1982). Numerical data are found in appendix A.

The RKS equation is known to yield too large values for the liquid molar volume V . The correction term proposed by Peneloux (Reid *et al.* 1987) reads

$$V = V_{RKS} - c, \quad (3.3)$$

where V is the corrected molar volume and

$$c = 0.40768(0.29441 - Z_{RA}) \frac{RT_c}{p_c}.$$

Z_{RA} is the Rackett compressibility factor of the substance under consideration. For a mixture, the correction term is obtained by using the conventional mixing rule

$$c_m = \sum_i x_i c_i.$$

From the above equations, an expression for the chemical potential can be derived in analytical form in a standard way by integration of the pressure with respect to volume keeping T and n_i constant (obtaining the free energy F as a result), and then taking the derivative with respect to n_i . In this way an expression of the form $\mu = f(T, V, y_i)$ is obtained. For the liquid, of course, y_i is replaced by x_i .

The partial molecular volumes are found by substituting the mixing rules into the RKS equation and applying standard expressions from thermodynamics for the partial volumes (N_A denotes Avogadro's number),

$$N_A v_1 = V_{RKS} - x_2 \frac{\partial V_{RKS}}{\partial x_2} - c_1, \quad (3.4)$$

$$N_A v_2 = V_{RKS} + x_1 \frac{\partial V_{RKS}}{\partial x_2} - c_2. \quad (3.5)$$

In these equations the Peneloux correction has been used. Because of the use of the incompressible fluid approximation in deriving the Kelvin equations (2.7), the molecular liquid volume has to be calculated at pressure p_v outside the droplet. Using chemical potentials and molecular volumes obtained from Eqs. (3.2) – (3.5) in Eq. (3.1), a solution for the droplet bulk composition is found, and $\Delta^* \mu_i$ and v_i are known.

With this result, it is possible to calculate the droplet radius from either one of the Kelvin equations written in the form

$$r = - \frac{2\sigma v_i}{\Delta^* \mu_i}. \quad (3.6)$$

The critical free energy barrier, ΔG_{sp} , is now obtained from Eq. (2.8), provided that the surface tension is known.

Several correlations exist for the surface tension, most of which need the pure component values as their input. Since relevant temperatures are above the critical temperature of methane, these correlations can not be used for the mixture under consideration. A relation that can be used for our purposes is the Macleod–Sugden correlation (Reid *et al.* 1987), an expression obtained by the best fit to experiments. It reads

$$\sigma^{1/4} = \sum_i [P_i] \left(\frac{x_i}{V^l} - \frac{y_i}{V^v} \right) \quad (3.7)$$

in which superscripts l and v refer to liquid and vapour, respectively. The parameters P_i are the so-called parachors of the components. Originally, Macleod suggested to calculate these from molecular structures; however, better agreement with experiments can be obtained by empirically fitting the parachor values to measurements. For our calculations, the values obtained by Deam and Maddox (1970) are used. We note that the parachor method is a fit on bulk composition. This is consistent with the fact that, as a solution of the Kelvin equations, bulk compositions are obtained which are substituted into Eq. (3.7) in order to find the surface tension of the droplet. A limitation of this method is the lack of a proper correction for the curvature of the droplet surface which is still subject of discussion in literature (Tolman 1949, Thompson *et al.* 1984, Nijmeijer *et al.* 1992).

What remains to be calculated, is the kinetic prefactor K of expression (1.1) in which the second derivatives of ΔG at the saddle point position with respect to the total numbers of molecules, n_1^l and n_2^l are present. As was already pointed out in section 2.2.2, we have no information concerning the excess numbers n_1^s and n_2^s . According to Wilemski (1987), the best one can do is using Reiss' original expression for ΔG , i.e.,

$$\Delta G(n_1^l, n_2^l) = \sum_{i=1,2} n_i^l \Delta^* \mu_i + \sigma A \quad (3.8)$$

keeping σ constant at the value of the critical droplet¹. The shape of the ΔG surface obtained in this way is approximately correct in the vicinity of the saddle point.

For the impingement rates β_i present in the growth rate tensor \mathbf{R} [Eq. (2.18)], the ideal expression $\beta_i = \rho_i / \sqrt{k_B T / 2\pi m_i}$ is used, where ρ_i is the number density of monomers of species i , and m_i is the molecular mass. It is expected that the values of β_i only have a slight effect on the nucleation rate.

No special attention has been paid to the limiting case of unary nucleation. It may be expected that a small overestimate of the nucleation rate appears, when the position of the saddle point is too close to the n_1 -axis. This might occur in the low pressure limit, in which only a little methane will be dissolved in the droplets. A more extensive treatment of this matter is given by Wilemski (1975).

Finally, we introduce a supersaturation S , which will be used in presenting results of our calculations

$$S = \frac{y_1}{y_{1,eq}}, \quad (3.9)$$

where y_1 and $y_{1,eq}$ are the molar vapour fractions of n-nonane² in the supersaturated state and at equilibrium, respectively. The equilibrium molar fraction is calculated by equating the chemical potentials in the vapour and the liquid for both components at given p and T . We emphasize that this definition is not used in the calculation of nucleation rates. The reason

¹Recently, Oxtoby and Kashchiev (1994) established a method to determine the total numbers of molecules n_i^c in the critical clusters on the basis of Thermodynamics. Combination of this method with CNT yields in addition to the number of bulk molecules n_i^l , the number of "surface" molecules n_i^s in the critical cluster. With this knowledge it is possible to construct a more consistent kinetic prefactor than described in this chapter.

²Regarding all binary mixtures subject of study in this thesis, the following convention is made: component 1 is the less volatile component of the mixture; in the case of a vapour and inert carrier gas, component 1 represents the vapour component.

for using the supersaturation ratio in representing the results is that S is considered to be the driving force behind the condensation process.

The calculations described are implemented in a FORTRAN numerical code. Calculations can be performed for n -alkanes (up to n -dodecane) with several carrier gases. The numerical data for the mixture n -nonane/methane, used in the present calculations, are listed in the appendix A. The program code is available upon request.

3.3 Results and discussion

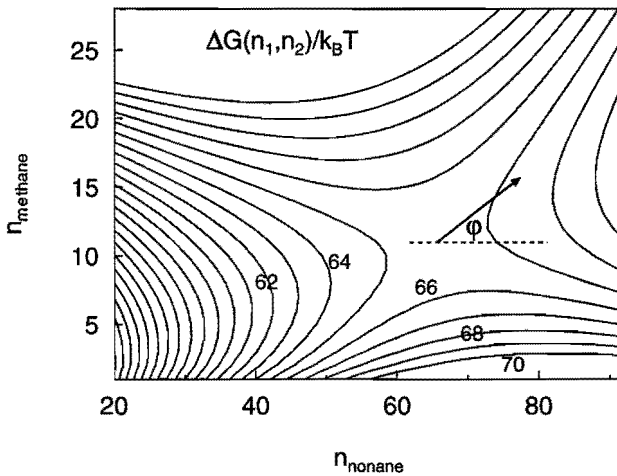


Figure 3.1: Contour plot of the free energy surface in the vicinity of the saddle point. $T = 240$ K, $p = 40$ bar, and $y_1 = 1 \times 10^{-4}$ ($S \simeq 8$). The value of ΔG at the saddle point is $65.5 k_B T$; contours correspond to increment steps of $1 k_B T$.

A plot of a typical free energy surface according to Eq. (3.8) for the n -nonane/methane mixture is shown in Fig. 3.1. The conditions are: $T = 240$ K, $p = 40$ bar and the molar fraction of n -nonane in the gas $y_1 = 1 \times 10^{-4}$ corresponding to a saturation ratio $S \simeq 8$. The critical cluster consists of 66 nonane molecules and 11 methane molecules. During nucleation, the saddle point is passed in the direction φ indicated by the arrow.

Figures 3.2 and 3.3 show the nucleation rate as a function of supersaturation with the pressure as a parameter for two different temperatures. The model predicts a large effect of total pressure on the nucleation rate. At fixed supersaturation, increasing pressure induces an increase of nucleation rate by several orders of magnitude demonstrating real gas effects in homogeneous nucleation. Apart from this phenomenon, the generally observed exponential dependence of nucleation rate on supersaturation at given total pressure and temperature can also be seen in the figures.

The interaction of nonane and methane in the nucleation process also comes forward when the composition of the critical cluster is considered. The saddle point of Fig. 3.1 already indicated the presence of methane in the critical cluster. In Fig. 3.4 the molar fractions of

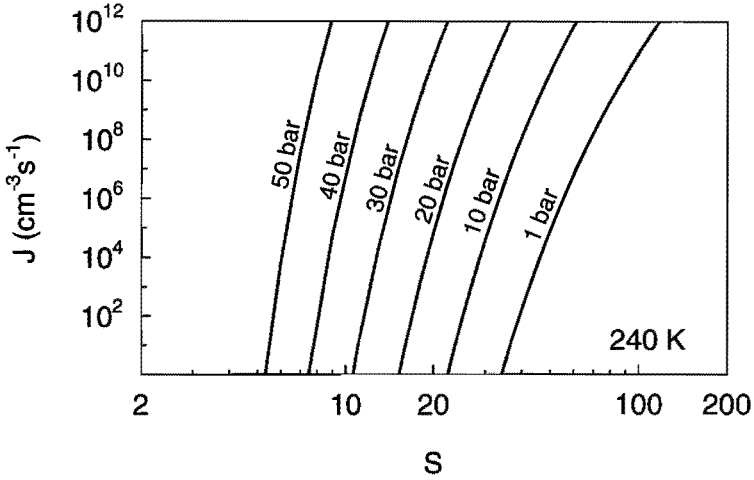


Figure 3.2: Nucleation rate in the mixture *n*-nonane/methane as a function of supersaturation with the total pressure as a parameter, $T = 240$ K.

methane in the critical cluster and in the corresponding equilibrium liquid state are plotted as a function of pressure at fixed supersaturation and temperature. The methane molar fraction increases from approximately 0 at low pressure to 0.11 at 40 bar. The methane fraction in the critical cluster is less than in the equilibrium liquid composition at the same conditions. In Fig. 3.5 the surface tension of the critical cluster is shown as a function of total pressure, at fixed temperature and supersaturation. The increasing amount of methane in the critical

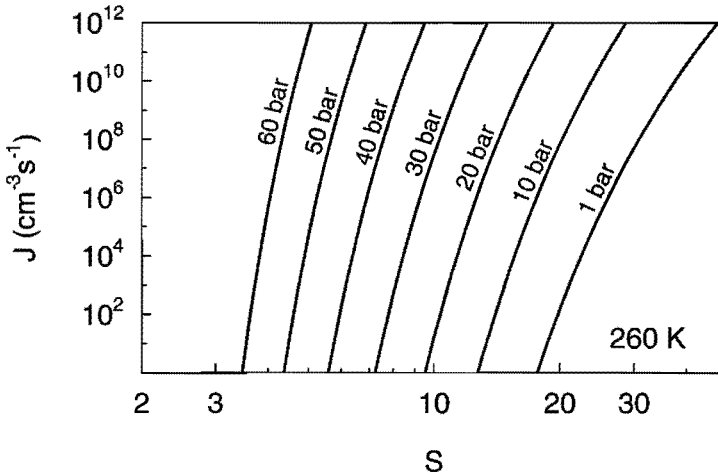


Figure 3.3: Nucleation rate in the mixture *n*-nonane/methane as a function of supersaturation with the total pressure as a parameter, $T = 260$ K.

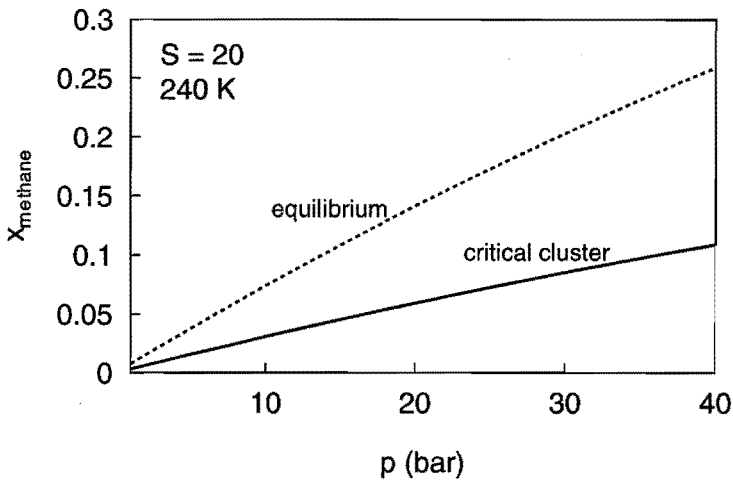


Figure 3.4: Methane liquid fraction as a function of total pressure. The solid curve represents the composition of the critical droplet at supersaturation $S = 20$. The dashed curve refers to equilibrium liquid; $T = 240$ K.

cluster lowers the surface tension from 2.7×10^{-2} N/m to 1.9×10^{-2} N/m at 40 bar. The height of the energy barrier ΔG_{sp} , which depends on the cluster composition, and in particular on the surface tension, decreases also with total pressure at fixed temperature and supersaturation. This explains the increase of nucleation rate with total pressure.

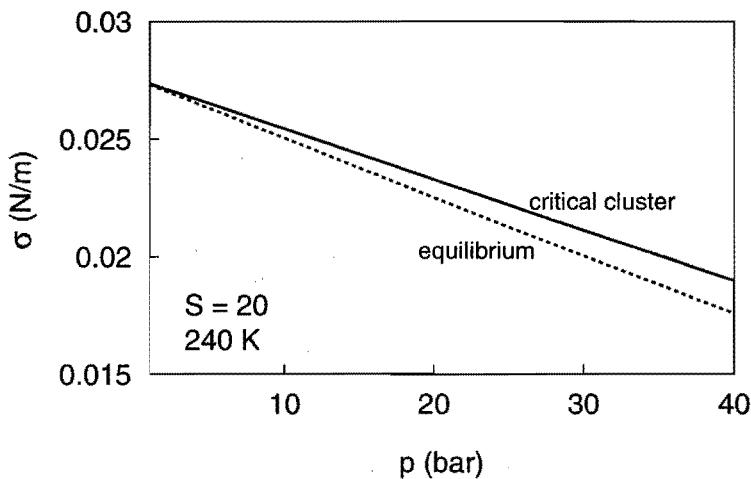


Figure 3.5: Surface tension as a function of pressure for fixed values of supersaturation and temperature. The solid curve corresponds to the critical droplet composition; the dashed curve refers to the equilibrium composition.

In Figs. 3.2 and 3.3 the nucleation rate was plotted as a function of supersaturation S . It has to be realized here that the saturated nonane vapour density itself depends on the mixture

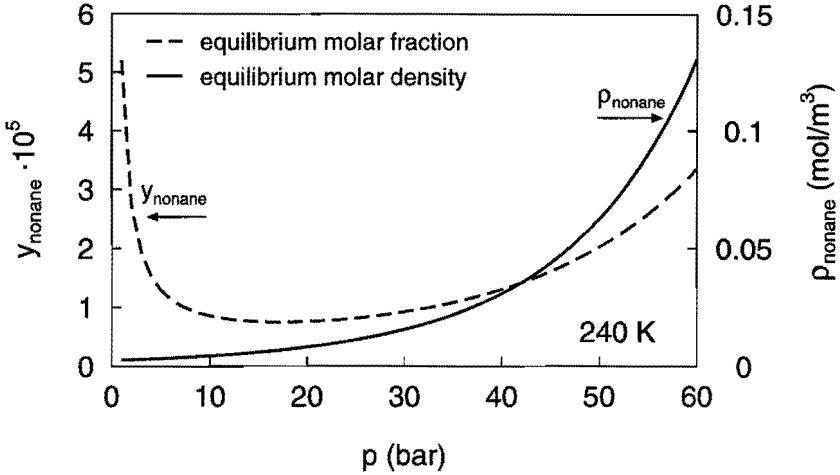


Figure 3.6: Pressure dependence of the equilibrium gas composition of the mixture *n*-nonane/methane. Dashed curve, nonane molar fraction in the gas phase at vapour–liquid equilibrium at 240 K as a function of the mixture total pressure. Solid curve corresponding equilibrium *n*-nonane vapour density.

total pressure, as is shown in Fig. 3.6. Due to real gas effects, the solubility of nonane in the gas phase increases, resulting in an increase of the equilibrium nonane concentration $y_{1,eq}$ and therefore an even stronger increase of equilibrium nonane vapour density $\rho_{1,eq}$, at pressures above 20 bar. So, S is not a measure for the actual nonane vapour density when nucleation rate curves at different pressures are compared. In Fig. 3.7 the nucleation rate is plotted as a function of nonane vapour density ρ_1 which is obtained from the relation $\rho_1 = y_1/V^v$, where V^v is the molar volume of the gas mixture. The $J - \rho$ -curves shift to the right at higher total pressures. The nucleation rate does not decrease monotonously with pressure at fixed *n*-nonane density. In the range of nucleation rates plotted in the diagram, the 1 bar curve crosses the 10 bar curve at 0.17 mol/m^3 , and the 20 bar curve at 0.28 mol/m^3 . The non-monotonous behaviour of nucleation rate with total pressure at fixed *n*-nonane density can also be observed in Fig. 3.8. In this plot the nucleation rate is given as a function of pressure (solid curve) with a fixed nonane vapour density of $\rho_1 = 0.25 \text{ mol m}^{-3}$. The dashed curve shows the nucleation rate if not methane, but an inert carrier gas is added. The pronounced difference between binary nucleation under real gas conditions and unary nucleation with an inert carrier gas is clear. Adding methane to nonane first shows a strong increase of nucleation rate, due to the lowering of surface tension caused by the presence of methane in the critical cluster. So, initially this effect dominates the effect of decreasing supersaturation with pressure. At higher pressures, the situation is reversed and finally, when pressure is high enough, thermodynamic equilibrium is attained again. Adding an inert component to a nonane vapour of fixed density shows a monotonically decreasing nucleation rate with (inert) gas pressure, this being a result of a

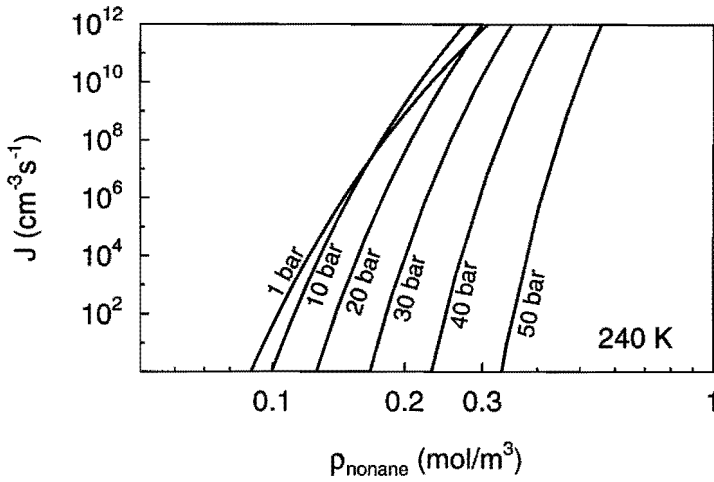


Figure 3.7: Nucleation rate in the mixture *n*-nonane/methane as a function of nonane vapour density for different total pressures at $T = 240$ K.

higher energy barrier due to the increase of liquid chemical potential, while vapour chemical potential is not changed much, this is known as the Kelvin-Helmholtz effect. Recently, a reduction of the nucleation rate with increasing total pressure of 1-propanol in helium and in hydrogen was experimentally found by Heist *et al.* (1994) in a special high pressure diffusion

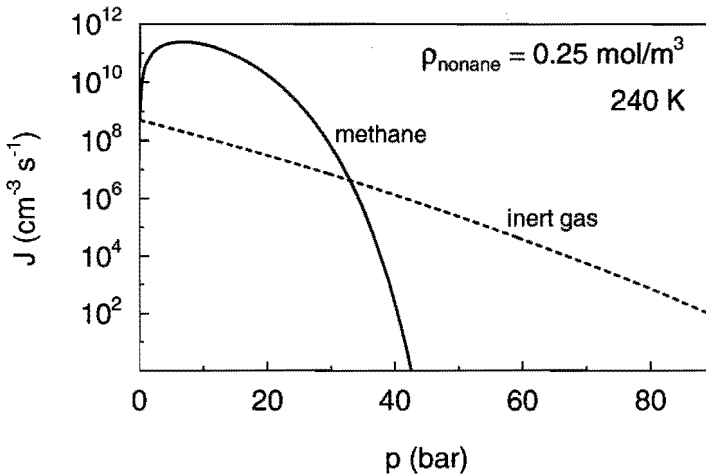


Figure 3.8: Nucleation rate as a function of pressure for a fixed nonane vapour density $\rho_1 = 0.25 \text{ mol m}^{-3}$. Solid curve, *n*-nonane/methane mixture calculated with binary nucleation theory. Dashed-curve, CNT for *n*-nonane with an inert carrier gas; $T = 240$ K.

cloud chamber.

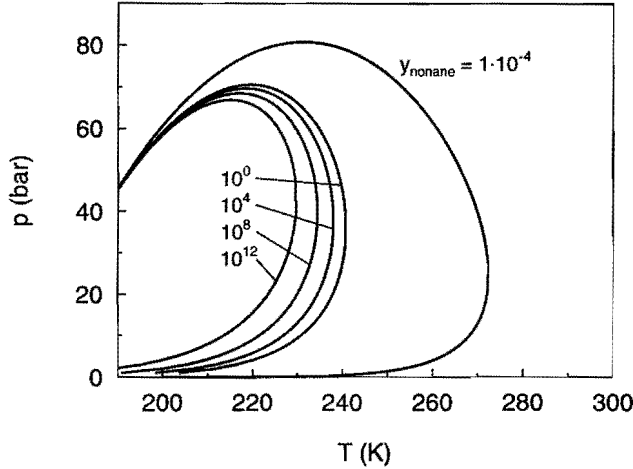


Figure 3.9: $p - T$ diagram with lines of constant nucleation rate for a gas mixture with molar fraction *n*-nonane $y_1 = 1 \times 10^{-4}$. The outer curve corresponds to vapour-liquid equilibrium for given nonane fraction. The labels denote the nucleation rate in $\text{cm}^{-3} \text{s}^{-1}$.

Finally, in Fig. 3.9 a $p - T$ phase diagram is shown of a *n*-nonane/methane mixture with a nonane molar fraction of 1×10^{-4} . The outer curve, on which the gas mixture with given nonane concentration is in equilibrium with the liquid phase, forms the boundary of the two-phase coexistence region. Inside this envelope, lines of constant nucleation rate are drawn, lines representing higher nucleation rates are found further inwards the coexistence region. Furthermore, lines of given nucleation rate form “retrograde curves”, and they all appear to converge to the critical point of the mixture.

3.4 Conclusions

The classical binary nucleation theory has been extended with a thermodynamic model taking into account real gas effects. For calculating chemical potentials and molar volumes the RKS equation of state was applied, surface tension was modeled with the Parachor method. This model allows the theoretical study of homogeneous nucleation of real gas mixtures in the coexistence region, such as the *n*-nonane/methane mixture, subject of the calculations presented in this thesis. The model predicts for this mixture an increase of nucleation rate with pressure when supersaturation and temperature are fixed. Due to real gas effects, an increasing amount of methane is present in the critical droplet with increasing pressure, as also occurs in equilibrium condensation. The presence of methane in the critical cluster lowers the surface tension, and therefore the free energy of formation is lowered, leading to an enhanced nucleation rate.

We have only presented calculations for the *n*-nonane/methane mixture. However, it is to be expected that similar results are found in other mixtures at high pressures, when interactions

between the mixture components are present. An example is the *n*-nonane/nitrogen mixture.

References

- DEAM, J.R., & R.N. MADDOX. 1970. Interfacial tension in hydrocarbon systems. *J. Chem. Eng. Data* **15**(2):216–222.
- FLAGEOLLET-DANIEL, C., J.P. GARNIER, & P. MIRABEL. 1983. Microscopic surface tension and binary nucleation. *J. Chem. Phys.* **78**(5):2600–2606.
- HEIST, R.H., M. JANJUA, & J. AHMED. 1994. Effects of background gases on the homogeneous nucleation of vapors. 1. *J. Phys. Chem.* **98**(16):4443–4453.
- KNAPP, H., R. DÖRING, L. OELLRICH, U. PLÖCKER, & J.M. PRAUSNITZ. 1982. *Vapor-Liquid Equilibria for Mixtures of Low Boiling Substances*. Frankfurt am Main: Deutsche Gesellschaft für Chemisches Apparatewesen.
- MIRABEL, P., & J.L. CLAVELIN. 1978. Experimental study of nucleation in binary mixtures: The nitric acid–water and sulfuric–water systems. *J. Chem. Phys.* **68**(11):5020–5027.
- NIJMEIJER, M., C. BRUIN, A.B. VAN WOERKOM, A.F. BAKKER, & J.M.J. VAN LEEUWEN. 1992. Molecular dynamics of the surface tension of a drop. *J. Chem. Phys.* **96**(1):565–576.
- OXTOBY, D.W., & D. KASHCHIEV. 1994. A general relation between the nucleation work and the size of the nucleus in multicomponent nucleation. *J. Chem. Phys.* **100**(10):7665–7671.
- REID, R.C., J.M. PRAUSNITZ, & B.E. POLING. 1987. *The Properties of Gases and Liquids*. New York: McGraw-Hill Book Company.
- SHIPMAN, L.M., & J.P. KOHN. 1966. Heterogeneous phase and volumetric equilibrium in the methane–*n*-nonane system. *J. Chem. Eng. Data* **11**(2):176–180.
- STREY, R., & Y. VIISANEN. 1993. Measurement of the molecular content of binary nuclei. Use of the nucleation rate surface for ethanol–hexanol. *J. Chem. Phys.* **99**(6):4693–4704.
- THOMPSON, S.M., K.E. GUBBINS, J.P.R.B. WALTON, R.A.R. CHANTRY, & J.S. ROWLINSON. 1984. A molecular dynamics study of liquid drops. *J. Chem. Phys.* **81**(1):530–542.
- TOLMAN, R.C. 1949. The effect of droplet size on surface tension. *J. Chem. Phys.* **17**(3):333–337.
- WILEMSKI, G. 1975. Binary nucleation. I. Theory applied to water–ethanol vapors. *J. Chem. Phys.* **62**(9):3763–3771.
- WILEMSKI, G. 1987. Revised classical binary nucleation theory for aqueous alcohol and acetone vapors. *J. Phys. Chem.* **91**(10):2492–2498.
- ZAHORANSKY, R.A., & F. PETERS. 1985. Binary nucleation at low temperatures. *J. Chem. Phys.* **83**(12):6425–6431.

Chapter 4

EXPANSION WAVE TUBE

4.1 Nucleation pulse method

introduction

One of the powerful techniques to measure homogeneous nucleation rates in a supersaturated vapour is the nucleation pulse method. The principle of this method is the separation of the initial nucleation stage from the droplet growth stage. By applying a proper history of the thermodynamic state, the nucleation stage is limited to a very short time interval, the nucleation pulse. After this stage a state of supersaturation is maintained over a longer time interval which causes the nucleated drops to grow to macroscopic sizes. By doing so, detection and counting of droplets is simplified, since all droplets are of nearly the same size.

In diagram 4.1 the desired saturation profile belonging to a nucleation pulse is schematically drawn. Initially, the vapour is undersaturated ($S < 1$). During a short time interval Δt ,

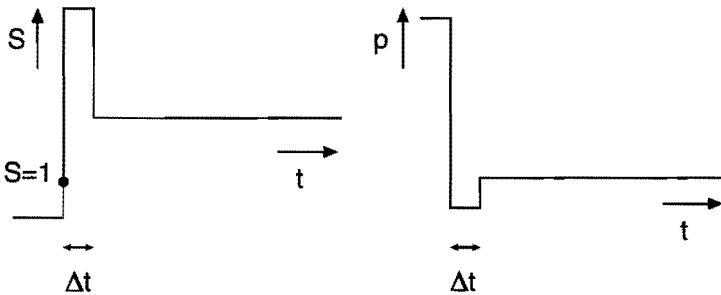


Figure 4.1: Schematic saturation history and accompanying pressure history required to produce a nucleation pulse.

a state of critical supersaturation (generally $S \gg 1$) prevails, and homogeneous nucleation takes place. Critical supersaturation is the term that refers to the maximum supersaturation in the nucleation pulse, which is chosen such that the number of droplets formed falls in the detection limit of the apparatus used. Therefore it is not an objective measure, but device dependent; the critical supersaturation in diffusion cloud chambers for instance is lower than in expansion chambers. Then supersaturation is lowered, so that the nucleation process is

quenched, but because a supersaturated state is maintained, the microscopic droplets formed during the nucleation pulse grow further to macroscopic droplets.

The desired saturation profile can be achieved by gasdynamic means. Subjecting a vapour to a fast adiabatic expansion by which also the temperature is lowered leads to the increase of the saturation up to the critical supersaturation. The subsequent reduction of supersaturation is produced by a small recompression. In order to keep the supersaturation as well as possible at a constant level during the nucleation pulse, the condensing droplets are not allowed to affect the thermodynamic state by vapour depletion or heat release. Therefore the nucleation rate is limited to an upper bound (in our situation this is always satisfied), while the duration of the nucleation pulse must be very limited in time (of the order of milliseconds).

The nucleation rate J is determined by

$$J = \frac{c}{\Delta t}, \quad (4.1)$$

where c is the droplet concentration which is measured after the droplets acquired a detectable size.

Allard and Kassner (1965) first applied the nucleation pulse method to homogeneous nucleation in a supersaturated vapour in a piston expansion chamber. During an experimental run, a programmed piston expanded and recompressed the gas/vapour mixture, resulting in a nucleation pulse duration of about 10 ms, and typical nucleation rates of $10^0 - 10^5 \text{ cm}^{-3}\text{s}^{-1}$. In this chamber an extensive study of nucleating water vapour in helium was made, in which also the influence of impurities was made clear (Allen and Kassner Jr. 1969, Hagen *et al.* 1982). The inert carrier gas helium did not take part in the condensation process, but acted as a heat reservoir for the latent heat released by condensation. The cloud chamber was further refined by Schmitt *et al.* (1982) who studied the nucleation of ethanol and toluene vapour. Wagner and Strey (1981) developed a two piston expansion cloud chamber in which the nucleation pulse duration was reduced to 1 ms.

Another useful tool for condensation studies proved to be the shock tube device [e.g. (Wegener and Lundquist 1951, Barschdorff 1975)]. A shock tube consists of two sections: the High Pressure Section (HPS), usually called the driver section, and the Low Pressure Section (LPS) or driven section. High pressure section and low pressure section are separated by a diaphragm. When the diaphragm is removed a wave pattern develops in the shock tube due to the initial pressure difference between HPS and LPS. In condensation studies the vapour (mixture) subject to investigation is inside the HPS together with a carrier gas. By means of an expansion wave, which induces a pressure and temperature decrease, condensation is initiated.

Peters (1983, 1987) realized a nucleation pulse in a wave tube, which actually is a shock tube, at the endwall of the high pressure section by means of a constriction in the low pressure section. In the $x - t$ diagram of Fig. 4.2 the wave propagation in Peters' expansion tube is given. The nucleation pulse is generated at the endwall by the reflection of the initial shock wave at the constriction running behind the initial expansion wave.

Our pulse expansion tube is a modification of Peters' wavetube; the post nucleation pressure is improved by replacing the original constriction in the low pressure section by a local widening. The gasdynamic aspects of the new tube are outlined in sections 4.2 and 4.3.

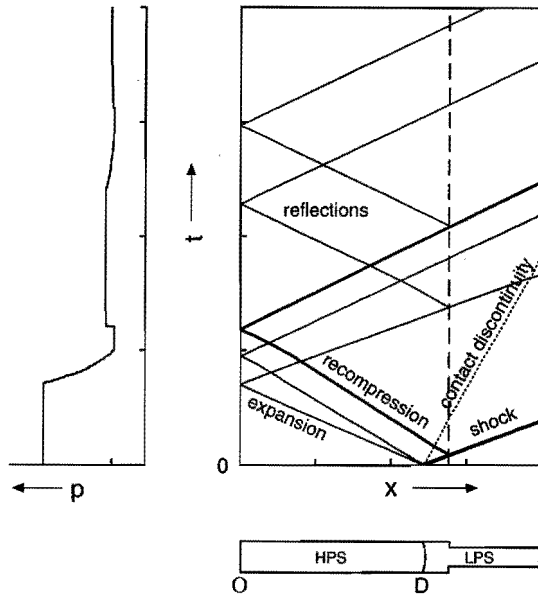


Figure 4.2: Wave diagram and pressure history of the expansion tube of Peters with a constriction in the low pressure section. The dashed line shows the position of the constriction. A nucleation pulse is formed at the observation point O at the endwall of the HPS by the reflection of the shock wave at the constriction. D denotes the position of the diaphragm. The diagrams were calculated with the Random Choice numerical Method (RCM) (see appendix C). The calculations were done with nitrogen gas, the pressure was chosen 2 bar in the HPS, and 1 bar in the LPS.

4.2 The shock tube

In Fig. 4.3 an ordinary shock tube is schematically sketched together with the wave pattern in the tube during operation. On the left hand side the high pressure section is situated, the low pressure section is on the right hand side. When the diaphragm is opened, the wave pattern divides the $x - t$ plane in four uniform regions. In the initial state the high pressure section is at a pressure p_4 and the low pressure section at p_1 , $p_4 > p_1$. The velocity $u = 0$ in both regions (1) and (4). A shock wave, which is a discontinuous compression front of the gas, propagates into the LPS, increasing pressure and temperature; $p_2 > p_1$, $T_2 > T_1$. In region (2) a flow velocity u_2 is induced. A centered rarefaction wave propagates into the HPS, lowering pressure and temperature; $p_3 < p_4$, $T_3 < T_4$. The expansion wave has a spatial extension; the head of the wave travels with the initial speed of sound c_4 , the tail of the wave travels with a lower speed because of the diminished sound speed c_3 , and a flow speed u_3 to the right, both induced by the expansion wave. Regions (2) and (3) are connected by a contact surface. Over this contact surface pressure and flow speed are continuous, but there is a jump in temperature and density; $u_2 = u_3$, $p_2 = p_3$, and $T_2 > T_3$, $\rho_2 \neq \rho_3$. The contact surface travels to the right with

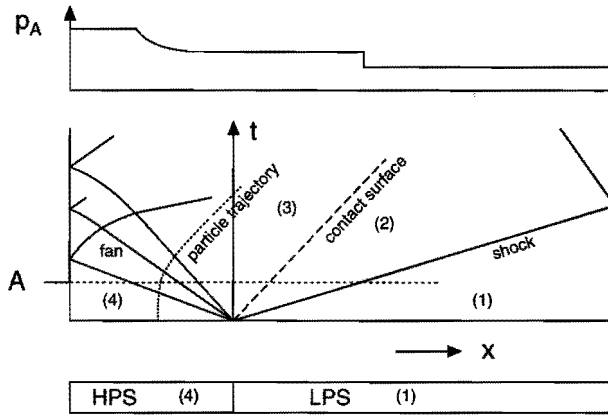


Figure 4.3: Schematic representation of a shock tube with wave diagram. The wave pattern divides the $x - t$ plane in uniform regions (1) to (4). The upper diagram shows the pressure distribution in the tube at time A.

flow velocity u_2 , it separates the gas that was initially in the high pressure section from the gas that was in the low pressure section.

The dashed curve in the figure shows the trajectory a fluid particle will follow. Initially, it is at rest; when the expansion wave passes it is accelerated to the right, until its speed equals the contact surface speed.

Because of the limited dimensions of the tube, at last the waves will encounter the endwalls of the tube. On the left the expansion wave reflects at the endwall bringing the flow into stagnation again.

The shock strength characterized by the shock Mach number M_s , which is the ratio of incident shock wave velocity and the sound speed, and the depth of the expansion are determined by the pressure ratio p_4/p_1 of the driver and driven section. It is possible to calculate thermodynamic and flow properties by connecting regions (1) up to (4) with the equations that describe unsteady wave propagation. In the next sections the wave propagation and wave interactions that are of concern in our tube will be outlined.

1-D unsteady wave propagation

Neglecting friction, heat transfer, and diffusion, the one-dimensional unsteady wave propagation is described by the Euler equations (Thompson 1984):

$$\frac{\partial \rho}{\partial t} + u \frac{\partial \rho}{\partial x} + \rho \frac{\partial u}{\partial x} = 0, \quad (4.2)$$

$$\frac{\partial u}{\partial t} + u \frac{\partial u}{\partial x} + \frac{1}{\rho} \frac{\partial p}{\partial x} = 0, \quad (4.3)$$

and

$$\frac{ds}{dt} = 0. \quad (4.4)$$

In the last equation, s is the specific entropy. In case of discontinuous waves like shock waves, the integral conservation laws must be applied. This will be described further on. The above non-linear equations are of the hyperbolic type. It is therefore convenient to write them in the characteristic form:

$$\left(\frac{\partial}{\partial t} + (u \pm c) \frac{\partial}{\partial x} \right) (u \pm F) = 0, \quad (4.5)$$

in which c is the sound speed defined as

$$c^2 = \left(\frac{\partial \rho}{\partial p} \right)_s, \quad (4.6)$$

and the thermodynamic variable F by:

$$F \equiv \int_{p_0}^p \frac{dp}{\rho c}. \quad (4.7)$$

$(u \pm F) \equiv J^\pm$ are called the Riemann invariants. Equation (4.5) expresses that in the characteristic directions $\frac{dx}{dt} = (u \pm c)$ the Riemann invariants $(u \pm F)$ are constant.

For a perfect gas with the ideal gas equation of state $p = \rho RT$, and the isentropic relations $\frac{d\rho}{\rho} = \frac{1}{\gamma-1} \frac{dc}{c}$ and $\frac{dp}{p} = \frac{2\gamma}{\gamma-1} \frac{dc}{c}$, the Riemann invariants turn into:

$$J^\pm = u \pm \frac{2c}{\gamma-1}, \quad (4.8)$$

with the constant isentropic exponent γ defined by the ratio of specific heats: $\gamma = \frac{c_p}{c_v}$.

The method of characteristics can be applied to calculate the solution in a neighbouring region of a line segment on which the J^+ and J^- are known, and which does not coincide with a characteristic. This is illustrated in Fig. 4.4. The C^+ characteristic coming from point (a) on

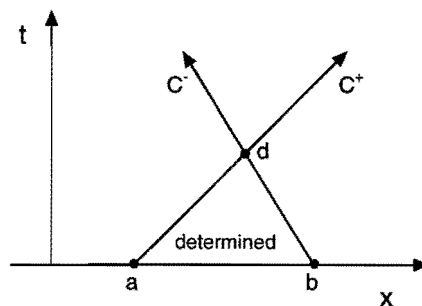


Figure 4.4: Method of characteristics. If the Riemann invariants are known on the line segment $a - b$, the flow properties can be calculated in the region bounded by $a - b$ and the characteristics C^- , and C^+ , denoted by “determined”.

which J^+ is uniform intersects with the C^- characteristic coming from (b) with constant J^- in point (d). The values u_d and F_d can be calculated from

$$\begin{aligned} u_d + F_d &= J_a^+ \\ u_d - F_d &= J_b^-. \end{aligned} \quad (4.9)$$

Solving this system yields

$$\begin{aligned} u_d &= \frac{1}{2} (J_a^+ + J_b^-) \\ F_d &= \frac{1}{2} (J_a^+ - J_b^-). \end{aligned} \quad (4.10)$$

As F is known in point (d), all thermodynamic variables are known. Similarly, the solution in the whole region enclosed by line $a - b$ and characteristics \mathcal{C}^+ and \mathcal{C}^- can be determined.

The expansion wave

In the $x - t$ diagram of Fig. 4.3 a centered rarefaction wave runs into the HPS. Because it is bounded by the uniform region (4), this expansion wave is a so-called simple wave. The \mathcal{C}^- characteristics all form straight lines $\frac{dx}{dt} = (u - c)$ over which J^- is uniform. Since the \mathcal{C}^+ characteristics originate from the uniform region (4), all J^+ Riemann invariants have the same value J_0^+ . The solution on a \mathcal{C}^- characteristic is given by

$$\begin{aligned} u &= \frac{1}{2} (J^- + J_0^+) \\ F &= \frac{1}{2} (J^- - J_0^+). \end{aligned} \quad (4.11)$$

The shock wave

The Euler equations (4.2) and (4.3) cannot be employed in differential form for discontinuous changes of the flow, such as is the case for shock waves. Applying the integral conservation equations in a reference frame attached to the shock front,

$$\begin{aligned} \rho u &= \hat{\rho} \hat{u} \\ p + \rho u^2 &= \hat{p} + \hat{\rho} \hat{u}^2 \\ \frac{1}{2} u^2 + h &= \frac{1}{2} \hat{u}^2 + \hat{h}, \end{aligned} \quad (4.12)$$

we obtain the Rankine–Hugoniot relation:

$$(\hat{p} - p) \left(\frac{1}{\hat{\rho}} + \frac{1}{\rho} \right) = 2(\hat{h} - h). \quad (4.13)$$

An illustration of a standing shockwave is given in Fig. 4.5. Since the enthalpy \hat{h} also satisfies an equation of state $\hat{h} = \hat{h}(\hat{p}, \hat{\rho})$, the Rankine–Hugoniot relation yields all states conceivable for a shock transition. A useful parameter is the shock Mach number M_s , defined by

$$M_s \equiv \frac{u}{c}, \quad (4.14)$$

which can be considered a measure for the shock strength.

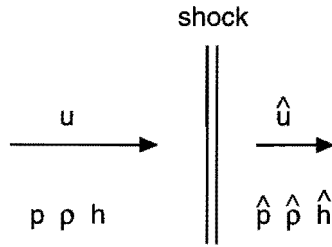


Figure 4.5: Stationary shock wave in a gas.

The Riemann problem

With the expressions for the expansion wave and the shock wave it is possible to solve the shock tube problem of fig. 4.3. The initial motion in a shock tube is caused by the discontinuity in pressure at the position of the diaphragm. The shock tube problem is a special variant of a Riemann problem. A Riemann problem is an initial value problem where a solution $U(x, t = 0)$ is known at the interval (x_a, x_b) . In the middle of the interval a discontinuity is present. Left and right from the discontinuity U is uniform.

The shock tube problem can be solved by connecting regions (1) up to (4) by the relations for u and p . This is illustrated in Fig. 4.6. The curve starting at state (4) in Fig. 4.6b represents

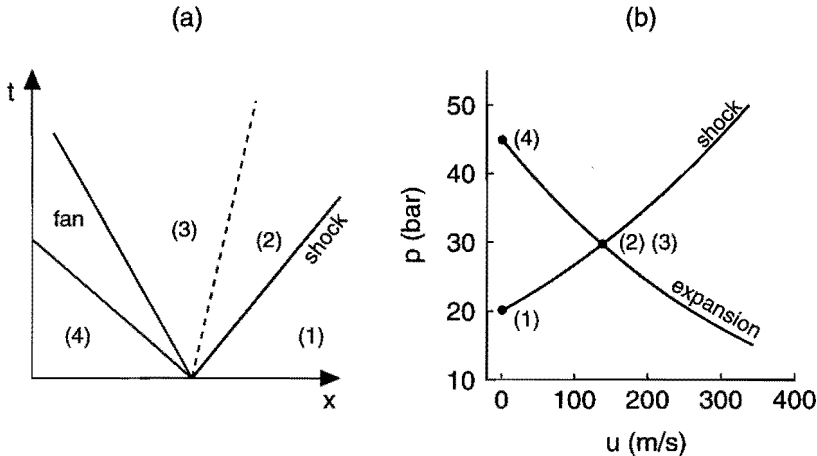


Figure 4.6: $x-t$ diagram (a) and $u-p$ diagram (b) of the shock tube problem. The intersection of the isentrope starting at state (4), and the shock adiabat starting at state (1) (Fig. b) represents the state of the middle regions (2) and (3) in the $u-p$ plane.

all states achievable by an adiabatic expansion wave in the HPS. The curve starting at (1) is the shock adiabat giving all states possible by a shock compression in the LPS. The solution in the middle region (2) and (3), u_m, p_m , is given by the intersection of both curves. Of course at the interface of the regions (2) and (3) the relations $u_2 = u_3$ and $p_2 = p_3$ hold.

Not only the initial waves in the tube are described by a Riemann problem. Also the shock wave reflection at changes of the tube diameter can be described in the form of a Riemann problem.

Shock wave reflection at a widening

When a shock wave running to the right arrives at a widening, we obtain the Riemann problem of Fig. 4.7. In the $x - t$ diagram an extra transition accounting for the change in tube cross section in addition to a contact discontinuity, divides the middle region into three distinct regions. When the flow on the spot of the cross section change is assumed to behave isentropically the following relations hold: Conservation of mass requires

$$u_l \rho_l = \frac{A_r}{A_l} u_r \rho_r. \tag{4.15}$$

The Bernoulli equation gives

$$\frac{1}{2} u_l^2 + i_l = \frac{1}{2} u_r^2 + i_r. \tag{4.16}$$

The assumption of isentropy states

$$S_l = S_r. \tag{4.17}$$

The subscript l and r refer to the the regions left and right from the position at which the cross section changes. The above equations yield two extra relations for u and p over the

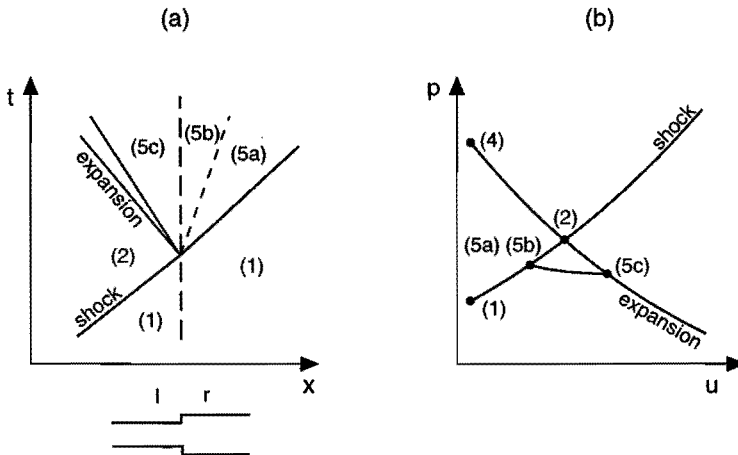


Figure 4.7: $x - t$ diagram (a) and $u - p$ (b) diagram of the shock reflection at a widening in the tube. The curve connecting regions (5a) and (5b) to (5c) in the $u - p$ plane represents the flow transition over the widening.

widening. In the $u - p$ diagram these relations form a curve from state (5a) to (5c) representing the transition of the flow over the widening. The pressure in region (5c) appears to be below the intersection of the expansion isentrope and shock adiabat that corresponds to the middle

region of the original shock tube problem. Therefore it follows that the reflection of the shock wave is a (small) expansion wave.

Shock wave reflection at a constriction

The shock wave reflection at a constriction in the shock tube is similar to the reflection at a widening, see Fig. 4.8. The curve connecting region (6a) and (6b) to (6c) appears at a pressure

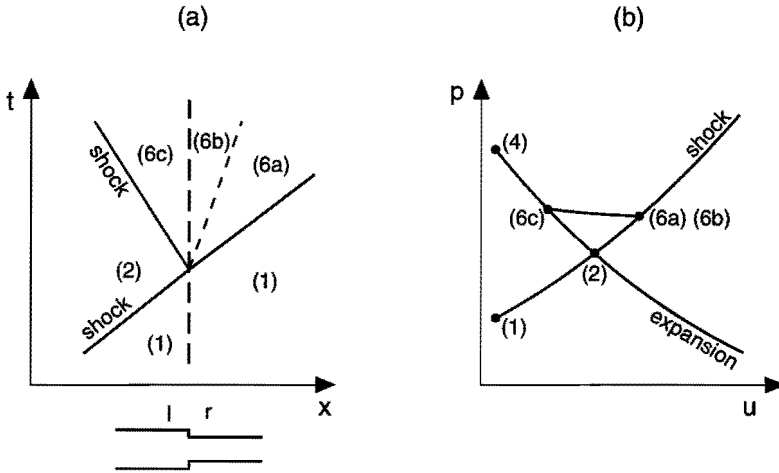


Figure 4.8: $x-t$ diagram (a) and $u-p$ (b) diagram of the shock wave reflection at a constriction. The curve connecting regions (6a) and (6b) to (6c) in the $u-p$ plane represents the flow transition over the constriction.

higher than the intersection of the isentropic and the shock adiabat. The reflection therefore is a weak shock.

4.3 The nucleation pulse expansion tube

4.3.1 Gas dynamic aspects

By choosing a special tube configuration the state of maximum supersaturation is realized only during exactly one nucleation period. A diaphragm separates the driver section, or high pressure section HPS of the tube, from the low pressure section LPS. In the LPS a local widening is situated 8 cm from the diaphragm. On both sides of the widening the tube cross section equals the cross section of the HPS. After diaphragm rupture, a wave pattern as in the $x-t$ diagram of Fig. 4.9 is formed. At time $t=0$ the diaphragm bursts. A rarefaction wave travels to the left into the HPS, while a shock wave runs into the LPS. When the rarefaction wave arrives at the observation point O at the endwall, it reflects and causes a rapid adiabatic drop of pressure. The shock wave first partly reflects at cross section change C_1 as a small centered rarefaction wave, that runs behind the first strong expansion wave and causes a second decrease in pressure at O .

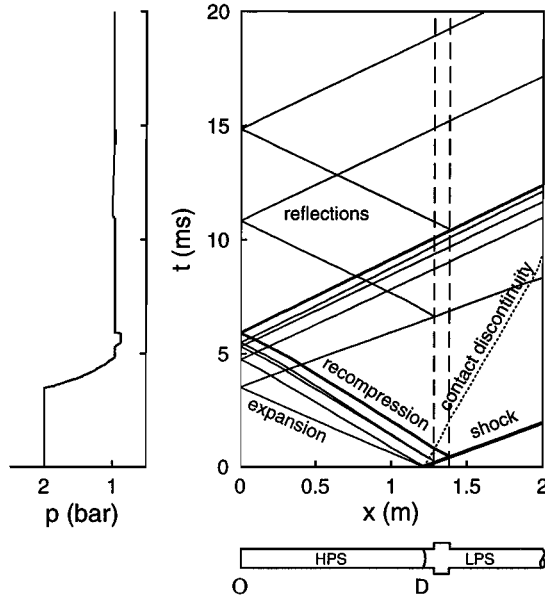


Figure 4.9: $x - t$ diagram of wave propagation in the pulse expansion tube with schematic tube configuration and pressure versus time diagram. The dashed lines show the position of the local widening. A nucleation pulse is formed at the observation point O at the endwall of the HPS by the reflections of the shock wave at the local widening. D denotes the position of the diaphragm. The diagrams were calculated with the Random Choice numerical Method (RCM). The calculations were done with nitrogen gas, the pressure was chosen 2 bar in the HPS, and 1 bar in the LPS.

After the waves have reflected from the endwall they will run back into the right hand direction and will meet again at the local widening. New reflections propagate into the HPS; as they reach O , pressure disturbances will be noticed. As a result of the configuration, these disturbances lead to a slight temporary recompression only. This can be understood as follows: The reflected first strong rarefaction wave reflects again at cross section change C_1 , which is a widening, as a recompression wave, denoted by the plus signs in the $x - t$ diagram. At C_2 it reflects as a small rarefaction wave, which is denoted by the minus signs. If the spatial extent of the rarefaction wave is large in comparison with the length of the widening, both reflections will interfere, and the disturbances will partially cancel. Finally, after the bump shaped disturbance, pressure recovers its undisturbed level.

4.3.2 Pressure and temperature in the nucleation pulse

The pressure and temperature in the nucleation pulse are a function of the initial pressure ratio p_4/p_1 in the shock tube. For gases that can not be considered to behave as an ideal gas, like methane at high pressure, they also depend on the initial pressure and temperature. The extra

expansion at the endwall due to the widening is related to the change in cross section. An analysis is made on the basis of the gas dynamic principles described in section 4.2. In Fig. 4.10 results are shown for methane in the wave tube. The ratio of cross sections A_r/A_l , with A_r the cross section of the widening, and A_l the cross section of the remainder of the tube, was taken 1.297. The calculations were performed for three different initial pressures p_4 in the HPS: 20, 50, and 80 bar, and for an initial temperature of 295 K. The equation of state used is

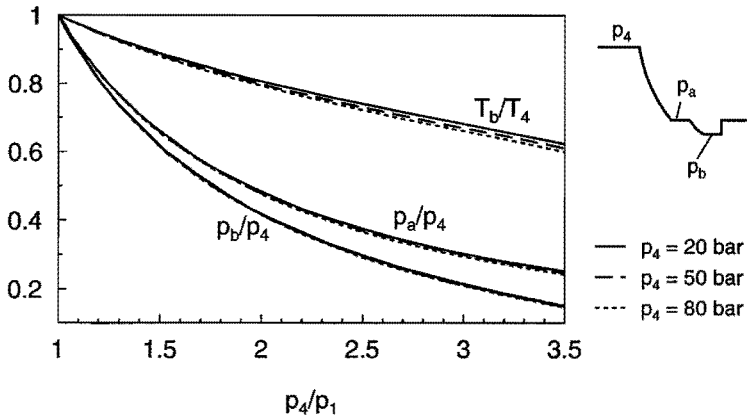


Figure 4.10: Pressure after the initial expansion, and pressure and temperature in the nucleation pulse as a function of the initial pressure ratio p_4/p_1 . Calculations were done for three different initial pressures in the HPS; 20, 50, and 80 bar. In both the HPS and the LPS the gas was methane. The initial temperature was 295 K, the ratio of cross sections A_r/A_l was 1.297.

the equation proposed by Sychev *et al.* (1987) which is described in appendix A. Due to real gas effects, which include Joule Thompson cooling, the temperature T_b in the nucleation pulse appears to be lower at higher initial pressure.

The depth of the nucleation pulse depends on the ratio of the cross sections right (A_r), and left (A_l) from the widening. This is illustrated in Fig. 4.11 for an initial pressure of 20 bar in the HPS. Of course the pulse depth also depends weakly on the initial pressure (Fig. 4.10) and temperature, but it appeared rather insensitive to the initial pressure ratio p_4/p_1 .

4.3.3 Numerical simulation and experiment

The gasdynamic behaviour of the described expansion–shock tube configuration has been studied numerically (Looijmans *et al.* 1993). The numerical method used is the so called one-dimensional Random Choice Method (RCM) described by Chorin (1976); see also appendix C. This numerical method solves unsteady flow problems as a sequence of Riemann problems at each time level. A quasi-random sampling determines the solution on the next time level. Smolders *et al.* (1992) applied an operator splitting method to include the influence of condensation relaxation processes in the unsteady flow in an expansion tube.

At the position of a varying cross section the Riemann problem becomes more complicated. The area change is situated in the middle of a numerical cell, which is the position of the initial

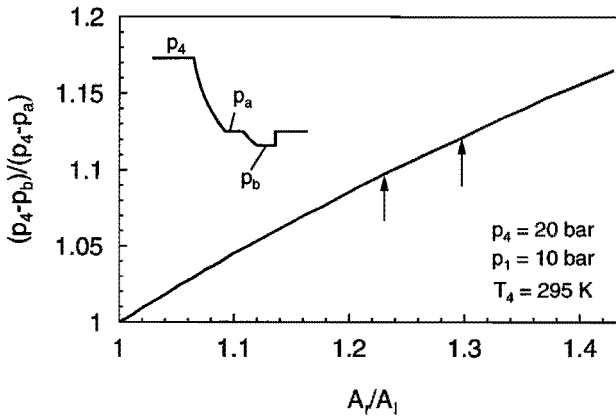


Figure 4.11: Depth of the nucleation pulse compared to the initial expansion, as a function of the ratio of the cross sections right (A_r), and left (A_l) from the widening. The initial conditions of the HPS are listed in the figure. The gas was methane in both the HPS and LPS. The arrows indicate the ratios of the widenings used in the nucleation experiments.

discontinuity in the Riemann problem. Two equations must be added to connect the areas left and right of the change in cross section. Conservation of mass requires:

$$u_l \rho_l = \frac{A_r}{A_l} u_r \rho_r, \quad (4.18)$$

where u and ρ are the gas velocity and density in the areas left and right of the change in cross section, and the ratio A_r/A_l is the ratio of cross section areas. The steady Bernoulli equation for a perfect gas yields:

$$\frac{1}{2} u_l^2 + \frac{\gamma}{\gamma - 1} \frac{p_l}{\rho_l} = \frac{1}{2} u_r^2 + \frac{\gamma}{\gamma - 1} \frac{p_r}{\rho_r}, \quad (4.19)$$

with p the pressure. Equations (4.18) and (4.19) give a quasi stationary model for the gas flow at the cross section change. This cross section change is treated as ideal; the gas flow is considered to behave isentropically, and no loss coefficient to include vortex shedding is incorporated in the model.

With an expansion–shock tube having a configuration as described above, the pressure has been measured at the endwall as a function of time. A diaphragm made of Melinex polyester film separates the HPS, of length 1.25 m, from the LPS. At the initial time $t = 0$ the membrane is removed by weakening it by a filament. Then the pressure difference causes the diaphragm to rupture. A pressure gauge of type Kistler 603B is mounted in the endwall which measures pressure p at the observation point O . Figure 4.12 gives the results of two experiments, together with the numerical simulations with the RCM. Both experiment and simulation show a pressure profile as expected from the gasdynamical analysis. Numerical simulation and experiment agree satisfactorily. The minimum pressure plateau at which nucleation has to take place is somewhat above the expected theoretical value and shows a slight variation. This variation diminishes as

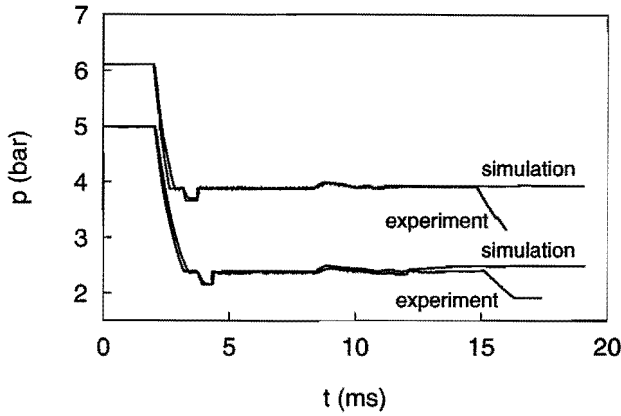


Figure 4.12: Pressure history at the endwall of the high pressure section of the expansion-shock tube, together with a numerical simulation by the RCM. The gas in the tube was nitrogen, initial temperature was 293 K.

the operation pressure of the tube is increased. Some improvement may further be expected from optimizing the diaphragm bursting mechanism. As time proceeds, a slight difference between simulation and experiment occurs. This probably arises from wall friction. After 15 ms, both pressure curves start to deviate. This is a consequence of different boundary conditions at the right end of the expansion-shock tube in experiment and simulation.

In Fig. 4.13 a simulation is shown of the nucleation rate during the nucleation pulse. The

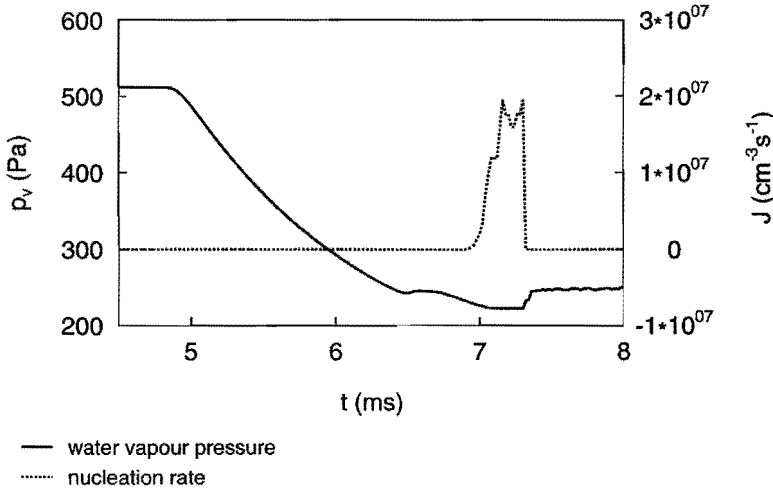


Figure 4.13: Simulation of the nucleation rate by classical nucleation theory for water vapour during the nucleation pulse.

variations in nucleation rate appear to be 40% of the maximum nucleation rate due to pressure variations during the nucleation pulse. Before and after the nucleation pulse the nucleation rate is 6 orders of magnitude lower than during the nucleation pulse, which can be considered as negligible small.

If a measured first expansion signal is compared with an analytical pressure time history of a centered rarefaction wave reflecting from the endwall, it appears that the tail of the experimental expansion fan arrives $140 \pm 20 \mu\text{s}$ later than theoretically predicted. This retarded expansion is an indication for the effective opening time of the membrane which is small in comparison with the total expansion time of $1.1 \pm 0.1 \text{ ms}$. From the result of the effective opening time of the membrane, an estimate of the minimum length of the HPS can be made. Reducing the length of the tube has the advantage of an increasing cooling rate, while the amount of test gas required is kept as small as possible. If we allow the time of the disturbance caused by the opening of the membrane to be one fifth of the expansion time, this results in a minimum length of the HPS of 66 cm.

References

- ALLARD, E.F., & J.L. KASSNER, JR. 1965. New cloud-chamber method for determination of homogeneous nucleation rates. *J. Chem. Phys.* **42**(4):1401-1405.
- ALLEN, L.B., & J.L. KASSNER JR. 1969. The nucleation of water vapor in the absence of particulate matter and ions. *J. Colloid and Interface Sci.* **30**(1):81-93.
- BARSCHDORFF, D. 1975. Carrier gas effects on homogeneous nucleation of water vapor in a shock tube. *Phys. Fluids* **18**(5):529-535.
- CHORIN, A.J. 1976. Random choice solution of hyperbolic systems. *J. Comput. Phys.* **22**:517-533.
- HAGEN, D.E., J.L. KASSNER, JR., & R.C. MILLER. 1982. Homogeneous nucleation of water anomalies explained by recognition and elimination of heterogeneous species. *J. Atmospheric Sci.* **39**:1115-1123.
- LOOIJMANS, K.N.H., P.C. KRIESELS, & M.E.H. VAN DONGEN. 1993. Gasdynamic aspects of a modified expansion-shock tube for nucleation and condensation studies. *Exp. Fluids* **15**:61-64.
- PETERS, F. 1983. A new method to measure homogeneous nucleation rates in shock tubes. *Exp. Fluids* **1**:143-148.
- PETERS, F. 1987. Condensation of supersaturated water vapor at low temperatures in a shock tube. *J. Phys. Chem.* **91**(10):2487-2489.
- SCHMITT, J.L., G.W. ADAMS, & R.A. ZALABSKY. 1982. Homogeneous nucleation of ethanol. *J. Chem. Phys.* **77**(4):2089-2097.
- SMOLDERS, H.J., E.J.M. NIESSEN, & M.E.H. VAN DONGEN. 1992. The random choice method applied to non-linear wave propagation in gas-vapour-droplet mixtures. *Comp. Fluids* **21**:63-75.

- SYCHEV, V.V., A.A. VASSERMAN, V.A. ZAGORUCHENKO, A.D. KOZLOV, G.A. SPIRIDONOV, & V.A. TSYMARNY. 1987. *Thermodynamic properties of methane*. Washington: Hemisphere publishing corporation.
- THOMPSON, P.A. 1984. *Compressible-Fluid Dynamics*. Rensselaer: The Maple Press Company.
- WAGNER, P.E., & R. STREY. 1981. Homogeneous nucleation rates of water vapor measured in a two-piston expansion chamber. *J. Phys. Chem.* **85**(18):2694-2700.
- WEGENER, P., & G. LUNDQUIST. 1951. Condensation of water vapor in the shock tube below 150°K. *J. Appl. Phys.* **22**(2):233.

Chapter 5

EXPERIMENTAL METHOD

5.1 Introduction

In chapter 4 the principle of the nucleation pulse method and its implementation in a shock tube was discussed. This chapter deals with the construction and operation of the high pressure pulse expansion tube for homogeneous nucleation and droplet growth studies. The experimental techniques employed are outlined as well as the measuring procedure.

5.2 The nucleation experiment

The pulse expansion tube was constructed according to the principle described in chapter 4. Figure 5.1 gives a schematic drawing of the wave tube facility together with its peripherals. On the left side is the HPS and on the right side we recognize the LPS with the local widening; HPS and LPS are separated by the diaphragm consisting of a polyester membrane clamped in the diaphragm section DS. After the system has been evacuated, the binary gas–vapour mixture is prepared in the HPS. To obtain a homogeneous mixture, the gas is circulated through the HPS by a rotary pump RP in the mixing circuit. The initial pressure is between ambient pressure and 100 bar, while the initial temperature is room temperature (293–295 K). The pressure in the LPS is adjusted to the HPS pressure such that the conditions desired are obtained during the nucleation pulse. After the diaphragm has ruptured the wave pattern develops as described in section 4.3.3. The nucleation pulse is formed near the endwall of the HPS, where nucleated droplets are detected by two optical techniques: a light extinction method providing droplet concentration, and a light scattering method yielding droplet concentration and time resolved droplet sizes. The electronic signals from the pressure transducer near the endwall, and from the light extinction and scattering instruments are recorded by a waveform recorder.

5.3 Expansion tube construction

5.3.1 High pressure section and mixing circuit

The HPS consists of three main parts: The endwall chamber with windows and a valve to the mixing circuit, a tube of 1 m length, and a chamber housing two valves connected to the mixing circuit and the vacuum pump. The inner circular cross section of the tube is of 36 mm diameter, the outer tube diameter is 56 mm. To minimize distortion of wave propagation the

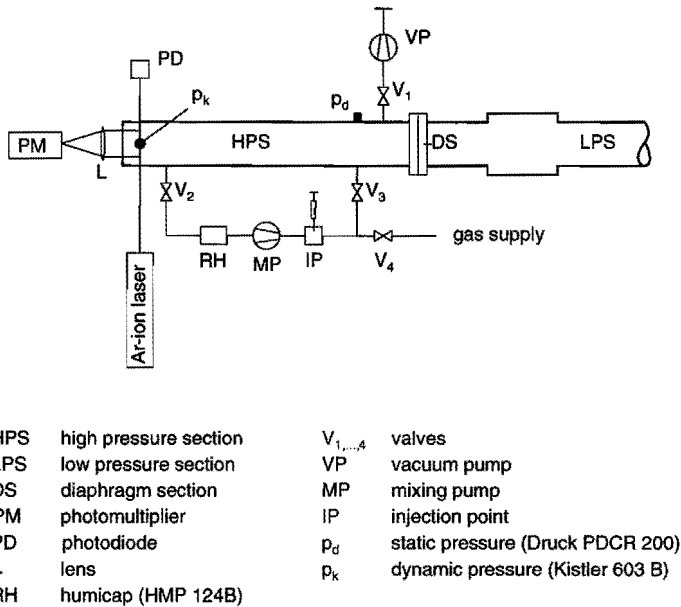


Figure 5.1: Experimental set-up.

valves close flush to the wall. Also the pressure transducers in the endwall chamber and valve chamber are mounted as flush as possible to the walls. In order to avoid corrosion and to reduce vapour adsorption on walls, almost all parts of the HPS are made of stainless steel. For sealing purposes rubber O-rings and quad-rings are used. The total length of the HPS is 1.26 m and the tube was designed to withstand over 100 bar pressure.

The mixing circuit is linked to the HPS by valves V_2 and V_3 (Fig. 5.1). It consists of stainless steel tubing with an inner diameter of 8 mm. In the mixing circuit the gas inlet, an injection point IP for the vapour component, a rotary pump RP, and a humidity gauge are integrated. All valves and coupling parts have metal seals to minimize vapour adsorption. The rotary pump in the mixing circuit is a double plunger pump which is sketched in Fig. 5.2. The operating conditions of the mixing pump require no moving parts connected to the outside world, as the pump has to be gas tight at vacuum conditions as well as at pressures up to 100 bar. Furthermore, no lubricator was allowed, for this would contaminate the gas mixture. Accordingly, the plunger PI and pistons Pi_1 and Pi_2 are driven by magnetic induction due to coils C_1 to C_6 placed outside the pump tubing.

In the situation of Fig. 5.2 coils C_1 , C_4 , and C_5 are activated. Piston Pi_1 is forced upwards and rests against the upper valve seat, piston Pi_2 is in the downward position. The plunger travels from left to right inducing a flow in the pump as sketched in the figure (accordingly it is required that the opening time of the pistons is small compared to the time in which the piston travels from one end to the other). When the plunger has reached the most left position coils

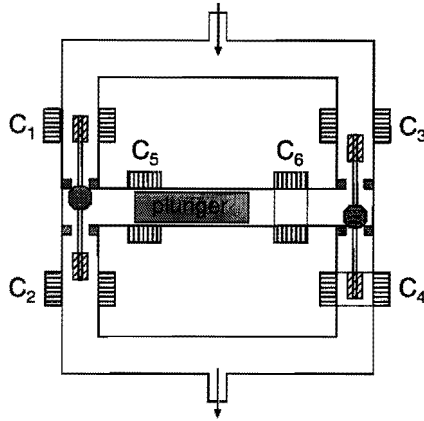


Figure 5.2: Schematic representation of the mixing pump.

C_2 , C_3 , and C_6 are activated, the others are switched off. Piston Pi_1 now closes the downward branch, and Piston Pi_2 the upward branch, while the piston starts moving in the opposite direction. In this case, the flow through the pump is still in the downward direction. When the plunger has reached the right end, the whole process starts over again. For an optimum performance there has to be a phase delay between piston and plunger; the movement of the plunger starts first, after the pistons already have closed the respective branches.

To test the mixing pump the HPS and mixing circuit were filled with water vapour. Then, nitrogen was added until the pressure was 100 bar. The humidity gauge with a time constant of 15 s monitored the relative humidity in the circuit during the mixing process. The pump speed appeared to be too low to provoke turbulent mixing, but due to the instationary flow induced by the plunger and piston movements, sufficient mixing is achieved. For the conditions mentioned no significant variations in humidity were observed any more after 12 minutes of mixing, indicating the water/nitrogen mixture being homogeneous. At lower pressures the required mixing time is less than 12 minutes.

5.3.2 Diaphragm construction

The diaphragm section is an important part of the pulse expansion tube; the “quality” of the generated waves, and thus of the nucleation pulse shape, are particularly determined by the opening of the diaphragm. Therefore the mechanism is subjected to the following requirements: The opening time of the diaphragm must be as short as possible, the diaphragm section is not permitted to form any obstruction to the flow, and obviously it must withstand the forces that act on it during high pressure experiments.

The diaphragm section is sketched in fig. 5.3. A polyester diaphragm (polyethylenterephthalate, thickness $50 \mu\text{m} - 500 \mu\text{m}$) separates the HPS from the LPS. The diaphragm is squeezed against an electrically high-resistant ribbon (Kanthal) on the LPS side. This ring-shaped ribbon is located around the tube cross section in a special polyester (Vespel) that insulates the ribbon from other metal parts, and which also can stand temperatures up to 800 K. The ribbon

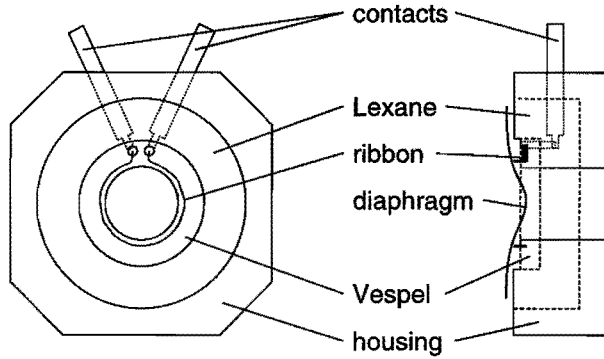


Figure 5.3: Diaphragm section.

is electrically heated, thereby weakening the polyester diaphragm, which subsequently ruptures by the pressure difference between LPS and HPS. The temperature of the hot ribbon increases in a period of 50 ms from room temperature up to 600 °C. The opening time of the diaphragm appears to be of the order of 100 μs (see section 4.3.3).

5.3.3 Low pressure section including local widening

The low pressure section is formed by a straight stainless steel tube of 6.4 m length with a circular inner diameter of 36 mm which equals the diameter of the HPS. Behind the diaphragm at a distance of 18 cm the local widening is located. This widening is made of brass. The widening has a length of 15 cm, the inner diameter is 41 mm resulting in a cross section ratio of 1.29 compared to the remaining tube cross section. The length of the widening (in combination with the pressure ratio p_4/p_1) determines the nucleation pulse duration, while the cross section ratio determines the pulse depth. The total measuring time after the nucleation pulse is a function of the total length of the HPS and LPS together, which is illustrated in Fig. 5.4.

The shock wave reflecting from the endwall of the LPS raises the pressure when it arrives back at the endwall of the HPS. Because of this, the supersaturation falls below unity, and the droplets evaporate. A rough estimate of the measuring time t_{growth} is given by:

$$t_{growth} = \frac{2L_{LPS}}{M_s c}. \quad (5.1)$$

In this equation L_{LPS} is the lengths of the LPS. Taking as an example the velocity of sound c at an average of 400 m/s and a shock Mach number of 1.2, a measuring time t_{growth} of 27 ms is found.

5.4 Experimental techniques

Our major objective is to measure nucleation rates for different thermodynamic states of the gas mixture. For this purpose the following parameters must be experimentally determined:

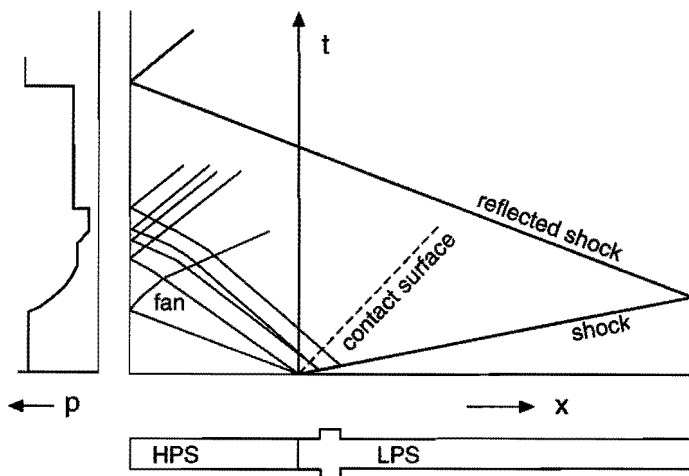


Figure 5.4: Schematic $x - t$ diagram with shock wave reflection at the endwall of the LPS. When the reflected shock wave arrives at the endwall of the HPS, the pressure is raised, and the droplets start to evaporate.

1. pressure
2. temperature
3. droplet concentration
4. droplet growth rate
5. gas composition

In the following sections the experimental techniques to measure each individual parameter will be described.

In the case of hydrocarbon mixtures at high pressures, the direct determination of gas composition by generally applied methods has been proven not to be straightforward by virtue of several effects. As an alternative approach we propose an indirect determination of gas composition. The gas composition is deduced from measured droplet growth rates (section 5.4.3).

5.4.1 Thermodynamic state

Measuring the pressure

Two pressure gauges are mounted in the HPS; a Druck PDCR 200 piezo-resistive pressure transducer for high pressure experiments to measure the static pressure of the gas-vapour mixture before the expansion, possibly replaced by a PDCR 81 for low pressure experiments, and a Kistler 603 B (piezo-electric) that records the dynamic pressure during the expansion and subsequent measuring time. As the Kistler 603 B is sensitive to temperature gradients in its surface, the pressure transducer was coated with a silicon rubber (type black, nr. 732RTV) of approximately 1 mm thickness. This coating delays the influence of temperature effects during and after the expansion.

Calculating the temperature

The initial temperature is measured with a thermocouple (Keitley 871A, NiCr–NiAl) in good thermal contact with the wall of the HPS. It is assumed that the wall temperature equals the gas temperature inside the HPS. The temperature during the experiment is calculated under the assumption that the changes of the thermodynamic state are adiabatic in the core of the expansion tube:

$$\frac{T}{T_0} = \left(\frac{p}{p_0} \right)^\alpha. \quad (5.2)$$

In case of an ideal gas, Eq. (5.2) is an isentropic relation where the “cooling coefficient” α is given by $\alpha = \frac{\gamma-1}{\gamma}$, with γ the ratio of specific heats: $\gamma = \frac{c_p}{c_v}$.

When a gas does not behave ideally, α is no longer a constant but depends on temperature and pressure, and includes the effect of Joule-Kelvin cooling. The exponent α is derived from thermodynamics; it reads

$$\alpha = \frac{p}{T} \left(\frac{\partial T}{\partial p} \right)_s = \frac{R_0}{c_p} Z \left[1 + \frac{T}{Z} \left(\frac{\partial Z}{\partial T} \right)_p \right]. \quad (5.3)$$

The compressibility factor Z can be calculated from an appropriate equation of state (EOS). For the calculation of α we have chosen the EOS, and the relation of the specific heat c_p given by Sychev *et al.* (1987), see appendix A.

In the experiments α will be mainly determined by the gas component. The presence of a minor amount of vapour will change the “cooling coefficient” only a little. Since the effect on the temperature during the nucleation pulse is limited to less than 0.1 K, no correction has been applied to the cooling coefficient of the pure gas.

5.4.2 Optics

Introduction

Optical droplet detection based on scattering of electromagnetic radiation at small particles has been proven to be very successful in various studies on homogeneous nucleation and droplet growth, e.g., (Wagner and Strey 1984, Peters and Paikert 1989, Strey *et al.* 1994). In our expansion tube an extinction method is applied to measure droplet concentration, and a 90° light scattering method to measure droplet sizes. In this section first the results of Mie theory are summarized, next both the experimental techniques are outlined.

Mie theory

Light Scattering. Light scattering from spherical particles of any size is governed by the Maxwell equations. Depending on particle size it often is useful and possible to make certain simplifications. For particles small compared to the wavelength of the light, the Rayleigh theory is a good approximation, for droplets much larger than the wavelength, geometrical optics may be used. Good textbooks about light scattering are available, e.g., (Bohren and Huffman 1983, Van de Hulst 1981, Kerker 1969). In this work the notation of Van de Hulst is followed.

In our experiment droplet sizes during the droplet growth stage range from 0 to about $2 \mu\text{m}$ radius. This size typically is of the order of the wavelength of visible light. Light scattering from such particles is described by the Mie theory. This theory (Mie 1908) gives a rigorous solution of the Maxwell equations of a plane electromagnetic wave incident on a dielectric spherical particle of arbitrary size. Both scatterer and surrounding medium are assumed to be homogeneous and isotropic.

The scattered irradiance I (energy flux per unit area, from now on called intensity, following most texts about light scattering) depends on the refractive index m relative to the surrounding medium, the droplet size relative to the wavelength α , and on the scattering angles θ and δ . Figure 5.5 shows the geometry of the scattering problem. The plane E.M. wave of wave number

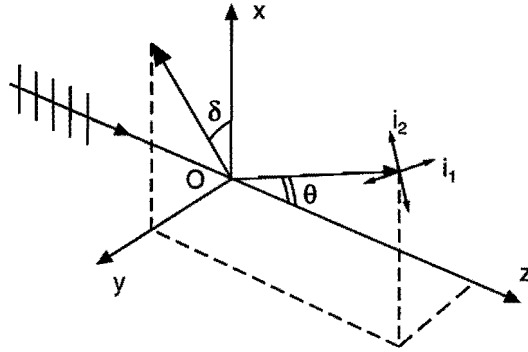


Figure 5.5: Geometry of scattering of a plane light wave incident on a spherical particle.

k in the surrounding medium, incident along the z -axis, is assumed to have a linear polarization in the $x - z$ plane. The angles θ and δ are the angles between scattering direction and direction of propagation of the incident wave, and between plane of scattering and plane of polarization respectively. The terms i_1 and i_2 refer to the intensity scattered perpendicular and parallel to the plane of scattering.

The scattered intensity (of one scattering sphere) is given by:

$$I(\alpha, m, \theta, \delta) = \frac{I_0}{2k^2 r_d^2} (i_1(\alpha, \theta, m) \sin^2 \delta + i_2(\alpha, \theta, m) \cos^2 \delta), \quad (5.4)$$

where r_d is the droplet radius. Droplet radius, wave number and size parameter α are related according to

$$\alpha = \frac{2\pi r_d}{\lambda} = k r_d. \quad (5.5)$$

The numbers i_1 and i_2 are given by Mie theory as the squares of the modulus of the amplitude functions $S(\theta)$

$$\begin{aligned} i_1 &= |S_1(\theta)|^2 \\ i_2 &= |S_2(\theta)|^2, \end{aligned} \quad (5.6)$$

whereas S_1 and S_2 are given by:

$$\begin{aligned} S_1(\theta) &= \sum_{n=1}^{\infty} \frac{2n+1}{n(n+1)} \{a_n \pi_n(\cos(\theta)) + b_n \tau_n \cos(\theta)\} \\ S_2(\theta) &= \sum_{n=1}^{\infty} \frac{2n+1}{n(n+1)} \{(b_n \pi_n(\cos(\theta)) + a_n \tau_n \cos(\theta))\}. \end{aligned} \quad (5.7)$$

The scattering coefficients a_n and b_n are combinations of Bessel-, Neumann-, and Hankel-functions, the angle dependent functions π_n and τ_n are combinations of the first derivatives of the Legendre polynomials.

The functions i_1 and i_2 can be evaluated numerically. Then, Eq. (5.4) gives the scattered intensity I for a single particle. To obtain the intensity scattered by a monodispersed cloud of droplets, I has to be multiplied by the number of droplets N , provided that the droplets are randomly distributed in space ensuring independent scattering, and provided that no multiple scattering occurs.

Extinction. In the previous paragraph, an expression for the intensity of the scattered light by a cloud of droplets was given. The energy of the scattered light is, because of conservation of energy, withdrawn from the incident light beam. The transmitted light beam will therefore be attenuated according to the law of Lambert-Beer:

$$I = I_0 \exp(-\beta L), \quad (5.8)$$

where β is the extinction coefficient and L the path length through the droplet cloud. The light beam will also be attenuated by possible absorption. This will not be considered here, the imaginary part of the refractive index of all substances used in this study being very small. Also the extinction coefficient can be derived from Mie theory; for a monodispersed droplet cloud it reads:

$$\beta = n_d \pi r_d^2 Q_{ext}(\alpha, m). \quad (5.9)$$

The extinction efficiency Q_{ext} , depending on α and m , accounts for the interference of the undisturbed beam and the light scattered in forward direction ($\theta = 0$). According to Van de Hulst (1981), Q_{ext} can be expressed as:

$$Q_{ext}(\alpha, m) = \frac{4}{r_d^2 k^2} \text{Re}\{S(0)\}. \quad (5.10)$$

Figure 5.6 shows the dependence of Q_{ext} on α for a refractive index of 1.395 corresponding to *n*-octane (Landolt-Börnstein 1962).

90° light scattering method

Detection of monochromatic light scattered by a cloud of growing droplets can be an excellent means of measuring droplet size and concentration. For a fixed scattering angle the intensity shows maxima and minima as the scattering droplets grow. The shape of these maxima – called “Mie-peaks” – and the rate at which they follow each other depend strongly on the scattering angle θ . In the expansion tube the observation section is located near the endwall of the HPS,

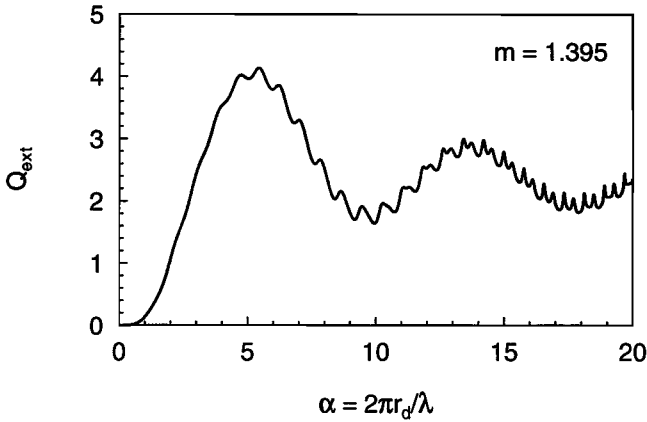


Figure 5.6: Extinction efficiency as a function of the size parameter α . The refractive index $m = 1.395$ corresponds to *n*-octane.

it is therefore straightforward to choose a $\theta = 90^\circ$ detection angle (fig. 5.7). A large window in the endwall of the tube provides a good optical accessibility. Furthermore, a scattering angle of 90° has the advantage of a larger number of Mie-peaks per unit of droplet radius than the often applied small θ forward scattering angles. A disadvantage is the lower intensity of the maxima, but this can be compensated by a higher power of the laser beam used.

In the optical set-up of fig. 5.7 an Argon-Ion laser (wavelength 514.2 nm, power 200 mW) passes the tube through two small windows in the sidewall, and illuminates the cloud of droplets. To avoid interference in the laser beam by reflections at the window surfaces, the windows are

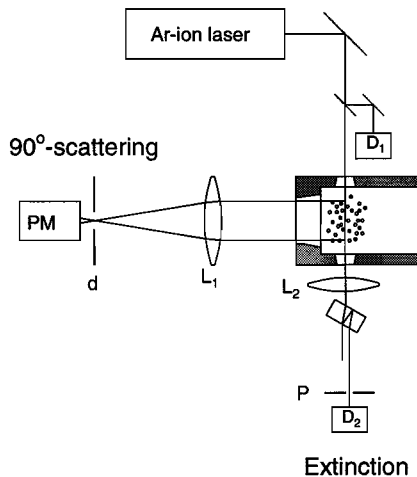


Figure 5.7: 90° Mie scattering set-up at the endwall of the expansion tube.

coated with an anti-reflex coating on the outer surface, and they are placed a little beneath the tube axis. Because the angle of incidence of the laser beam is 6° the internal reflections of the beam in the windows are spatially separated in the tube. The rectangular diaphragm d ($11\text{mm} \times 2\text{mm}$) in combination with lens L_1 (focal length 10cm) limits the scattering angles of scattered light focused on the photomultiplier PM (Hamamatsu 1P28A, red extended) to a θ -angle of $90^\circ \pm 1.15^\circ$ and a δ -angle of $90^\circ \pm 6^\circ$. Because the scattering direction is perpendicular to the plane of polarization, the scattered light is also linearly polarized, mainly in the transverse direction i_2 (Eq. (5.4); $\sin^2 \delta \ll 1$).

Figure 5.8 shows the 90° scattering intensity I_{scat} of n -octane (refractive index $m = 1.395$)

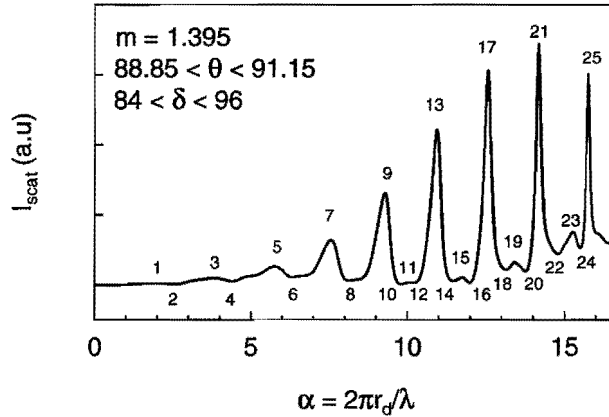


Figure 5.8: Theoretical 90° Mie scattering pattern. The refractive index $m = 1.395$ corresponds to n -octane. The scattering angles θ and δ were chosen in accordance with the experimental light scattering set-up. The characteristic maxima and minima of the “Mie-peaks” are numbered.

as a function of the size parameter α according to Mie theory. A sharply peaked pattern is observed. In the diagram specific parts of the intensity pattern such as peaks and valleys are numbered. These typical points of reference can be recognized easily when a measured intensity history is plotted as a function of the square root of time elapsed after the nucleation pulse (fig. 5.9). By mapping the theoretical and experimental Mie pattern together, each marked droplet size can be assigned uniquely to a point in time, so creating a droplet growth curve as a function of time.

The height of the Mie-peaks is a measure of the droplet number concentration. As remarked in section 5.4.2, the intensity scattered by a monodispersed droplet cloud is proportional to the number of droplets illuminated, provided that the droplets are independent scatterers. A drawback of determining droplet concentration by means of light scattering compared to the extinction method is that the light scattering method must be calibrated, this in contrast to the light extinction method.

Three factors may complicate the interpretation of the Mie scattering signal: multiple scattering, attenuation of the incident laser beam and of the scattered light, and finally the droplets being size dispersed.

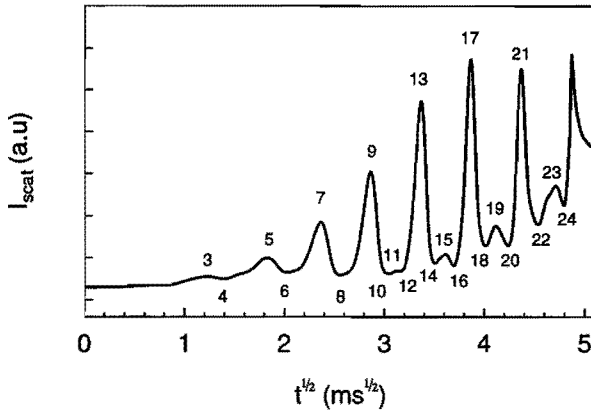


Figure 5.9: Experimental 90° Mie scattering pattern of *n*-octane. The numbers match the peak and valley numbers of Fig. 5.8. Identification of the peaks appears to be very easy. In order to facilitate peak recognition, the square root of the time is used for the *x*-axis scale.

Multiple scattering arises when the droplet cloud becomes this dense that light already scattered by droplets in the measuring volume (the volume illuminated by the laser beam in the tube) is scattered again by droplets inside or outside the measuring volume. Dense is used here in the sense of optically dense, which depends on droplet concentration as well as droplet size. Van de Hulst (1981) gives a rule of thumb for the condition that a correction for multiple scattering becomes important. If the optical depth $\beta L < 0.1$ no correction is required. Above this value correction may be necessary, and above 0.3 multiple scattering cannot be ignored. A numerical analysis has shown that multiple scattering detected by the photomultiplier of the light scattering technique, can be neglected at the typical droplet sizes and droplet number concentrations appearing in the nucleation and growth experiments.

A complication that also occurs in dense clouds, and which cannot be neglected, is the attenuation of the laser beam in the measuring volume, and the attenuation of scattered light before it is detected by the photomultiplier. When the laser beam extinction is significant, the intensity of the beam decays exponentially according to the law of Lambert–Beer. The contribution to the scattered light therefore varies with the position of the droplets in the measuring volume. Furthermore, the scattered light will also be attenuated due to scattering at droplets between the measuring volume and the detector, which actually is a form of multiple scattering.

The extinction effects the relative height of the different Mie-peaks. This is because each individual peak corresponds to a certain droplet size. Since the level of extinction also is a function of droplet size, the lowering is specific for each Mie-peak. Fig. 5.10 shows calculations with a *n*-nonane droplet cloud in our scattering configuration. The attenuation of the first three Mie-peaks versus droplet concentration is displayed. The height of the first Mie-peak is only attenuated above droplet concentrations of $n_p = 10^{13} \text{ m}^{-3}$. But if the third Mie-peak should be used for determination of the droplet concentration, a correction should be applied above

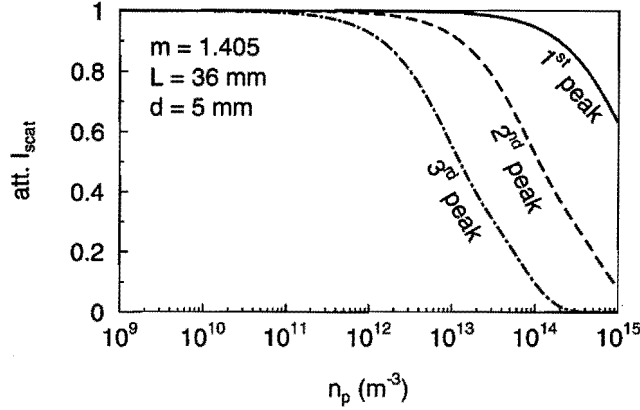


Figure 5.10: Attenuation of scattered light versus droplet number concentration. The curves show the amplitude of the first three Mie-peaks relative to the amplitude they would have when no attenuation of light occurs in the cloud. The length scales L which is the tube diameter, and d the distance of the laser beam to the endwall, are valid for our optical set-up. The refractive index $m = 1.405$ corresponds to *n*-nonane.

concentrations of $n_p = 10^{11} \text{ m}^{-3}$.

In the experimental situation there will never be an exactly monodispersed cloud of droplets. The zeroth-order lognormal distribution (ZOLD) is often used to describe the size distribution of a cloud of droplets (Kerker 1969, Smolders 1992, Rudolf 1994):

$$\mathcal{F}(r_d) = \frac{1}{\sqrt{2\pi}\epsilon r_m} \exp\left(-\left(\frac{\ln(r_d/r_m)}{\epsilon\sqrt{2}}\right)^2 - \frac{\epsilon^2}{2}\right), \quad (5.11)$$

with r_m the modal droplet radius at which \mathcal{F} has its maximum, and with ϵ the relative width of the ZOLD. The ZOLD becomes asymmetric for larger ϵ , and it is only defined for positive values of droplet radius r_d . The Mie patterns of Fig. 5.11 are obtained by averaging I_{scat} for each value of the modal droplet radius r_m over the ZOLD:

$$I_{scat}^{dis} = \int_0^\infty \mathcal{F}(r_m, r) I_{scat}(r) dr. \quad (5.12)$$

The size distribution has a smoothing effect on the Mie pattern; maxima and minima become less pronounced with increasing ϵ . Still, it is difficult to evaluate the influence of a size distribution on the light scattering more quantitatively, since a cloud of growing droplets tends to become more and more monodispersed during the growth process, so no unique value of ϵ can be assigned to one particular experiment.

Light extinction method

Once the droplet size is known from the light scattering method, the droplet concentration can be determined from the attenuation of the laser beam according to Eqs. (5.8) and (5.9).

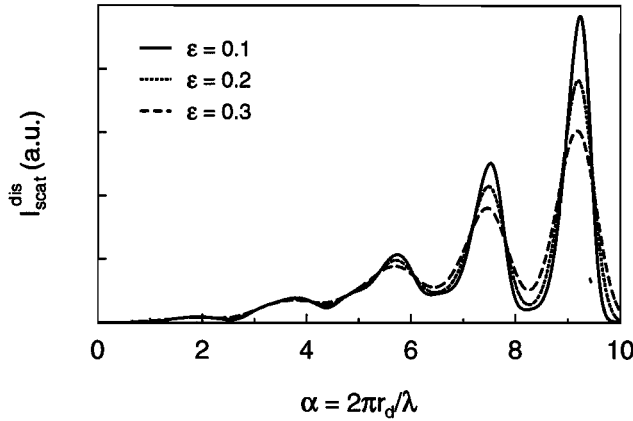


Figure 5.11: The effect of size dispersion of a droplet cloud on the 90° Mie scattering. The parameter ϵ denotes the relative width of the ZOLD function.

The advantage of using laser beam extinction for measuring droplet concentration is that no calibration is necessary.

The optical set up of the extinction method is also sketched in Fig. 5.7. After passage of the tube, the laser beam is focused by lens L_2 on a pinhole P with $\phi = 2$ mm, limiting the contribution of scattered light on the transmission signal to θ -angles less than 0.2° . Between lens and diaphragm a parallel glass plate attenuates the laser beam to approximately 0.2 % of the original intensity before it is recorded by photodiode D_1 (Telefunken BPW 34). Intensity variations of the laser beam are monitored by a reference signal (photodiode D_2 , Telefunken BPW 34).

Drawbacks of the light extinction set up. Although principally preferable above the light scattering method because of the self calibration property, the light extinction method has some practical drawbacks coming forward at high pressure experiments.

In Fig. 5.12 a cross-section of the tube is shown at the position of the side windows. If the refractive index inside the tube equals the refractive index of the surrounding air, the beam direction on exit equals the entrance beam direction. However the refractive index of the gas inside the tube varies with gas density ρ according to

$$n = 1 + \kappa\rho, \quad (5.13)$$

where κ is the Gladstone–Dale constant of the gas [for methane $\kappa = 6.15 \times 10^4 \text{ m}^3 \text{ kg}^{-1}$ (N.V. Nederlandse Gasunie 1988)]. The resulting angular deviation of the laser beam leads to a shift of the focus off the pinhole at high gas densities in the tube. An estimate for the angular deviation yields $2\Delta\varphi/\Delta\rho = 0.046^\circ \text{ bar}^{-1}$. This problem has been overcome by replacing the pinhole by a lens (not drawn in Fig. 5.7) of focal length = 2 cm and with a diameter of 1.5 cm focussing the laser beam on the photodiode. A disadvantage of this is the increase of intensity scattered in the forward direction that is also focused on the photodiode. Smolders (1992)

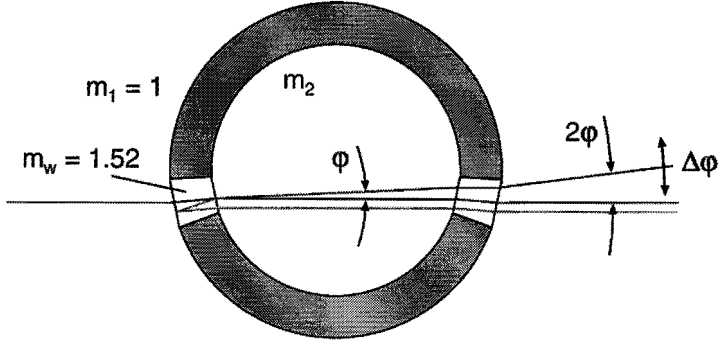


Figure 5.12: Angle variation of the laser beam as a consequence of a varying refractive index. At high pressures the refractive index of the test gas m_2 does not equal the refractive index of the surrounding gas. The laser beam refraction at the inner window surface differs from the refraction at the outer surface which results in an angular deviation φ . This deviation is doubled at the laser beam exit from the test chamber through the right hand window.

estimated the contribution of the scattered light on the transmitted beam:

$$\frac{P_s}{P_b} = n_d L \pi r_d^2 \frac{i_0(\alpha, m)}{\alpha^2} \theta_{det}^2, \quad (5.14)$$

where P_s is the scattered power on the photodiode, P_b the power of the transmitted beam, L the length of the measuring volume, and θ_{det} angle of detection which is assumed to be small. Replacing the pinhole with diameter $\phi_P = 2$ mm by the lens with diameter $\phi_L = 15$ mm, increases the scattered power detected by the photodiode by a factor $\phi_L^2/\phi_P^2 = 56$.

When the droplets in the cloud are of the size belonging to the first Mie-peak of the 90° light scattering signal, $r_d = 0.16 \mu\text{m}$, the ratio of scattered power and transmitted power detected by the photodiode becomes $P_s/P_b = 3 \times 10^{-18} n_d$, and at the second Mie-peak ($r_d = 0.32 \mu\text{m}$) $P_s/P_b = 1 \times 10^{-16} n_d$. With typical experimental droplet concentrations $n_d < 2 \times 10^{13} \text{ m}^{-3}$ this yields ratios of $P_s/P_b < 6 \times 10^{-5}$ (first Mie-peak), and $P_s/P_b < 2 \times 10^{-3}$ (second Mie-peak).

The maximum permitted extinction is 10 % of the total transmitted intensity, this being the upper limit satisfying the criterium of no multiple scattering, so the contribution of scattered light to the extinction signal leads to an error of the order of 10^{-2} in droplet number concentration, for the droplet size belonging to the second Mie-peak. For smaller droplets no significant error will occur, for larger droplets the contribution of scattered light to the extinction will be significant.

A second problem is the sensitivity of the extinction method to Schlieren effects. Density variations induced by the propagating waves, and developing in boundary layers refract the laser beam. Consequently, during and after the initial large expansion, the intensity of the transmitted laser beam fluctuates with 1 % of the total intensity. As the maximum permitted extinction is 10 % of the total intensity, the optimum feasible accuracy for high pressure experiments will be 10 %.

Reconsidering these two properties of the extinction set-up leads to the conclusion that at high pressures the extinction method can be used only as a calibration for the scattering method. The amplitude of the first Mie-peak of the scattering signal can be related to the droplet number concentration with a relative uncertainty of 10 %.

5.4.3 Mixture composition

Introduction

A very important parameter that is considered to be the driving force of nucleation and condensation is the saturation ratio S . In chapter 2, S was defined as the ratio of vapour fraction y_1 and the equilibrium vapour fraction $y_{1,eq}$ evaluated at the same pressure and temperature:

$$S = \frac{y_1}{y_{1,eq}} \simeq \frac{\rho_1}{\rho_{1,eq}}$$

The vapour fraction of the mixture y_1 , which is much less than the gas fraction y_2 , must be determined experimentally. Three methods to prepare a gas-vapour mixture of known composition are generally applied in nucleation experiments:

1. The vapour under investigation is in liquid form present in the experimental set up. This method is used in diffusion cloud chambers and often in piston expansion chambers. In the latter case the vapour pressure in the chamber equals the equilibrium vapour pressure which obviously is known when the temperature is known.
2. A gas mixture is prepared by first letting in one component of which the vapour pressure is measured, and next supplying the gas component after which the total pressure is measured.
3. The test chamber is circulated for a certain time with a gas flow of fixed composition. This is done to saturate the walls of the chamber with the vapour component. Once the walls are saturated the flow is stopped, and the experiment can start with the gas mixture present in the test chamber.

In the high pressure expansion tube experiment none of these three methods is well applicable. The first method requires that equilibrium is attained by diffusion in the whole HPS. A low diffusion coefficient at high pressure slows down this process. Also the temperature in the tube cannot be adjusted, so that the achievable supersaturations are limited very much. Furthermore, to obtain the equilibrium vapour concentration of a high pressure gas mixture, one has to rely on an equation of state. The second approach fails because of the process of vapour adsorption on tube walls and seals. This process is strongly dependent on pressure; the actual vapour pressure will differ strongly from the initial vapour pressure measured at a much lower pressure. Although possibly the best method, the last one has a practical drawback. Flushing the tube at a pressure of about 100 bar for several minutes would cost large amounts of gas per experiment.

In the present study we will follow a different approach: The composition of the mixture is not fixed precisely before the experimental run, but determined afterwards on the basis of the growth of the nucleated droplets. The rate at which droplets grow also depends on the

supersaturation and hence also on the vapour fraction. By comparing measured droplet growth rates to a droplet growth model, the vapour fraction of the mixture can be deduced. The applied droplet growth model is the explicit model of Gyarmathy (1982), modified such that solution of methane in the droplet at high pressures is taken into account. It will be shown that at high pressures certain approximations concerning the growth model can be made, leaving only one parameter that determines the uncertainty of the actual vapour fraction y_1 . In the next section this droplet growth model is summarized, for a more extensive treatment the reader is referred to papers of Oswatitsch (1990) and Young (1993).

Droplet growth

We consider a single droplet surrounded by a supersaturated gas mixture. The droplet will grow by incorporating gas molecules which is accompanied by the release of latent heat. The mass and heat flows are sketched in the gas–droplet system of Fig. 5.13. A droplet with radius

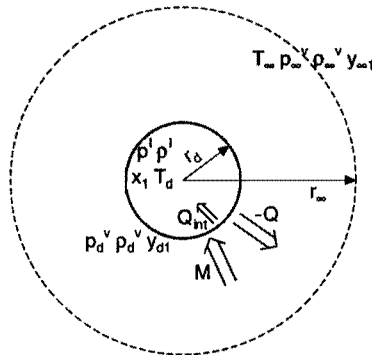


Figure 5.13: Model of a condensing droplet.

r_d is surrounded by a gas mixture. Far from the droplet at r_∞ , $r_\infty^3 \gg r_d^3$, the far field conditions are considered to hold: temperature T_∞ , total pressure p_∞^v , and vapour mass fraction¹ $y_{\infty,1}$; the density of the gas is ρ_∞^v . The droplet is characterized by the quantities T_d , p_d^l , ρ_d^l , and the fraction of component one in the droplet x_1 . Near the droplet the properties of the gas phase are: p_d^v , $\rho_{d,1}^v$, and $y_{d,1}$. The mass flow M into the droplet as well as the heat flow Q into the droplet and the internal heatflow Q_{int} in the droplet are defined to be of positive sign when they are directed towards the droplet; as a consequence the heatflow Q will be negative as the droplet releases latent heat of condensation.

The following assumptions are made regarding the droplet system:

- The droplet system is spherical.
- Changes in gas pressure are slow; characteristic time $\tau_p > 10$ ms.

¹Usually droplet growth models use the vapour pressure as a parameter; in order to avoid any confusion about the definition of partial pressures because of real gas effects, we will describe the model in terms of mass fractions rather than vapour pressures. The subscript 1 again denotes the vapour component of the mixture, i.e. the less volatile component.

- No slip between droplet and gas.
- No coalescence.
- The vapour fraction is small: $y_{\infty,1} \ll y_{\infty,2}$.
- The speed of the advancing droplet surface is small compared to the barycentric speed.
- Droplets grow independently; r_{∞} is determined by the droplet number concentration: $r_{\infty} = \sqrt[3]{3/(4\pi n_d)}$.
- All quantities in the droplet are uniform (Gyarmathy 1982).
- No pressure diffusion and thermo-diffusion.
- The total gas pressure in the vicinity of the droplet p_d^v equals the far field pressure p_{∞}^v (Gyarmathy 1982).
- The droplet is in mechanic and thermodynamic equilibrium with the surrounding gas: $p^l = p_d^v + 2\sigma/r_d$, and $y_{d,1}$ is the equilibrium vapour fraction belonging to the droplet.

For the droplet we can write down the following mass and heat balances at the droplet surface:

$$\frac{d}{dt} \left(\rho^l \frac{4}{3} \pi r_d^3 \right) = M. \quad (5.15)$$

This mass balance couples the increase (decrease) of droplet radius to the mass flux M . The heat balance equation

$$M \cdot L = Q_{int} - Q \quad (5.16)$$

expresses that the latent heat ML released by condensation is partially absorbed in the droplet by means of the internal heat flow Q_{int} thereby increasing the droplet temperature, and the remainder being absorbed in the gas by heat flow Q increasing the gas temperature. The internal heat flow Q_{int} can be expressed by:

$$Q_{int} = \rho^l \frac{4}{3} \pi r_d^3 \frac{dh^l}{dt}, \quad (5.17)$$

where h^l is the specific enthalpy of the liquid. It can be shown (Smolders 1992) that for the circumstances of this study the internal heat flow is small compared to the latent heat release. Hence, the growth process becomes stationary. Eq. (5.16) then turns into the equation

$$M \cdot L = Q \quad (5.18)$$

which is known as the wet-bulb approximation.

It is the task to substitute into the wet-bulb equation the appropriate relations for M and Q . Which equations should be used depends on the flow regime of concern. We discern the continuum flow regime and the free molecular flow regime. In the continuum flow regime the droplet is large compared to the mean free path of the ambient gas, and therefore mass and

heat transfer towards the droplet can be described by the differential equations for diffusion that are valid for continuum flow. The Knudsen number Kn

$$Kn = \frac{l}{2r_d}, \quad (5.19)$$

in which l is the mean free path of the molecules, is an indication for the particular flow regime. When $Kn < \frac{1}{100}$ the transfer processes are considered to be continuous.

In the continuum flow regime the equation describing mass transfer can be derived to be

$$M = 4\pi r_d \rho_{d,m}^v D_m \frac{y_{\infty,1} - y_{d,1}}{x_1 - y_{d,1}} \frac{r_{\infty}}{r_{\infty} - r_d}. \quad (5.20)$$

The subscripts ∞ and d refer to the far field and the neighbourhood of the droplet, respectively. The subscript m of the vapour density $\rho_{d,m}^v$ and diffusion coefficient D_m indicates that these quantities are to be evaluated at an intermediate temperature T_m between droplet temperature T_d and far field temperature T_{∞} . A one third rule (Hubbard *et al.* 1975) proved to be appropriate:

$$T_m = (2T_d + T_{\infty})/3. \quad (5.21)$$

For later use it is convenient to introduce a dimensionless Nusselt number for mass transfer

$$Nu_M = \frac{M}{2\pi r_d \rho_{d,m}^v D_m (y_{\infty,1} - y_{d,1})}, \quad (5.22)$$

which yields for the continuum regime

$$Nu_M^{ct} = 2 \frac{1}{x_1 - y_{d,1}} \frac{r_{\infty}}{r_{\infty} - r_d}. \quad (5.23)$$

The continuum heat flow Q is described by the relation

$$Q = 4\pi r_d \lambda_m (T_{\infty} - T_d) \frac{r_{\infty}}{r_{\infty} - r_d}, \quad (5.24)$$

with λ_m the thermal conductivity. The corresponding Nusselt number for heat transfer is

$$Nu_Q = \frac{Q}{2\pi r_d \lambda_m (T_{\infty} - T_d)}, \quad (5.25)$$

leading to the continuum Nusselt number for heat transfer

$$Nu_Q^{ct} = 2 \frac{r_{\infty}}{r_{\infty} - r_d}. \quad (5.26)$$

If the droplet size is small compared to the molecular mean free path, i.e., $Kn > 10$ the mass and heat transfer are determined by impingement rates β of single molecules, and surface kinetics. This is known as the Knudsen effect. At atmospheric conditions the free molecular flow regime or Knudsen regime ranges only to very small droplets $r_d < 5$ nm. Hence, at high pressures this effect will not play an important role. For the sake of completeness, the

expressions for mass and heat flow in the free molecular flow regime are given below, thereby it is assumed that only the vapour component "1" contributes to condensation:

$$M = 4\pi r_d^2 (\beta_{\infty,1} - \beta_{d,1}), \quad (5.27)$$

$$Nu_M^{fm} = \frac{2r_d}{D_m \rho_{d,m}^v (y_{\infty,1} - y_{d,1})} (\beta_{\infty,1} - \beta_{d,1}), \quad (5.28)$$

and

$$Q = 4\pi r_d^2 (T_{\infty} - T_d) \sum_{i=1}^2 \beta_{\infty,i} \frac{\gamma_i + 1}{2(\gamma_i - 1)} \frac{R}{m_i}, \quad (5.29)$$

$$Nu_Q^{fm} = \frac{2r_d}{\lambda_m} \sum_{i=1}^2 \beta_{\infty,i} \frac{\gamma_i + 1}{2(\gamma_i - 1)} \frac{R}{m_i}, \quad (5.30)$$

where γ is the ratio of specific heats.

For Knudsen numbers $\frac{1}{100} < Kn < 10$ we speak of the transitional flow regime. The pure free molecular flow regime and the pure continuum flow regime must be coupled, which is done here by introducing the following Nusselt numbers for the transitional flow regime:

$$Nu^{tr} = \frac{Nu^{ct}}{1 + \frac{Nu^{ct}}{Nu^{fm}}}. \quad (5.31)$$

This Nusselt number can have subscript M as well as Q . Nu^{tr} satisfies the limits $\lim_{r_d \rightarrow 0} Nu^{tr} = Nu^{fm}$ and $\lim_{r_d \rightarrow \infty} Nu^{tr} = Nu^{ct}$. The mass and heat transfer expressions for the total regime can now be written as

$$M = 2\pi r_d D_m \rho_{d,m}^v (y_{\infty,1} - y_{d,1}) Nu_M^{tr}, \quad (5.32)$$

and

$$Q = 2\pi r_d \lambda_m (T_{\infty} - T_d) Nu_Q^{tr}. \quad (5.33)$$

High pressure limit. Substitution of the expressions of the continuum mass flow (5.20) and heat flow (5.24) in the wet bulb equation (5.18) yields

$$\rho_{d,m}^v D_m (y_{\infty,1} - y_{d,1}) \frac{L}{x_1 - y_{d,1}} = \lambda_m (T_d - T_{\infty}). \quad (5.34)$$

This equation is an implicit equation for the droplet temperature T_d which can be solved exactly, but regarding the condition of high pressure we can make a simplifying approximation. If the far field vapour density $\rho_{\infty,1}$ is held fixed, the vapour fraction $y_{\infty,1}$ varies inversely proportional with the total pressure. The product $\rho_m^v D_m$ is rather insensitive to the pressure, while the latent heat L and the heat conductivity λ vary slightly as a function of pressure: L decreases, λ increases with increasing pressure. So, if the pressure is raised, the droplet temperature will approach the far field temperature:

$$y_{\infty,1} - y_{d,1} \rightarrow 0 \quad \Rightarrow \quad T_d \rightarrow T_{\infty}. \quad (5.35)$$

By combining Eqs. (5.15) and (5.20) with the high pressure limit ($T_d = T_\infty$) we obtain an explicit relation for the droplet growth rate:

$$\frac{d}{dt} \left(\rho^l \frac{4}{3} \pi r_d^3 \right) = 4\pi r_d \rho_d^v D \frac{y_{\infty,1} - y_{d,1}}{x_1 - y_{d,1}} \frac{r_\infty}{r_\infty - r_d}. \quad (5.36)$$

Since $T_d = T_\infty$ the subscript m has been left out of the equation.

Finally, we rewrite this with the assumption $r_\infty \gg r_d$ (under typical conditions this leads to an error less than 3 %) as

$$\frac{dr_d^2}{dt} = 2 \frac{\rho_d^v}{\rho^l} D \frac{y_{\infty,1} - y_{d,1}}{x_1 - y_{d,1}}. \quad (5.37)$$

The quantities x_1 , $y_{d,1}$, and ρ_d^v and ρ^l can be evaluated from the RKS equation of state by solving the Kelvin equations (2.7) analogous to the procedure in chapter 2. The parameter introducing the largest uncertainty in this equation is the diffusion coefficient D . We applied the Fuller method together with the Takahashi high pressure correlation (Reid *et al.* 1987) to determine the diffusion coefficient. For the mixtures n -nonane/methane and n -octane/methane no experimental data of diffusion coefficients are available, but for other mixtures, the diffusion coefficients calculated according to the Fuller method generally deviate less than 10% from measured values. The other terms in Eq. (5.37) are less sensitive to errors: the liquid fraction of the heavy hydrocarbon x_1 approaches unity, while at large supersaturations the equilibrium fraction $y_{d,1}$ is much smaller than the vapour fraction $y_{\infty,1}$.

The experimental vapour fraction is found by fitting a droplet growth curve calculated according to Eq. (5.37) to the measured growth curve by varying $y_{\infty,1}$. The procedure is as follows: Starting at $t = 0$ s, $r_d = 0.001 \mu\text{m}$, $T_\infty = T_{\infty,0}$, and $n_d = n_{d,0}$ and with a first guess for $y_{\infty,1}$, the parameters ρ_d^v , ρ^l , D , $y_{d,1}$, and x_1 are calculated at discrete time intervals. The required pressure is taken from the measured pressure history. At each time step the droplet radius r_d is recalculated, and the far field vapour fraction $y_{\infty,1}$ and the temperature T_∞ are corrected for vapour depletion and latent heat release. The procedure is repeated with a different $y_{\infty,1}$ until agreement between calculated and measured droplet growth curves is obtained.

5.5 Experimental procedure

An experiment starts with mounting the polyester diaphragm in the diaphragm section DS (see Fig. 5.1). Subsequently HPS and LPS are evacuated. To remove as much as possible foreign particles, like dust particles, that could act as condensation nuclei, and other vapours such as water vapour that entered the HPS when the membrane was installed, the HPS is evacuated for one hour by a turbo-molecular vacuum pump VP. The final pressure that is attained is below 10^{-2} Pa. The leakage rate of the tube has been established to be about 0.04 Pa/min. After the valve V_1 was closed, the vapour component is injected by means of a syringe into the mixing circuit through a septum (Chrompack, chromsep blue) at the injection point I_1 . Typical volumes that are to be injected range from 50 to 500 μl . In order to ensure the liquid has been evaporated and spread through the tube, the gas component is supplied into the HPS to the desired pressure first after 15 minutes. Simultaneously, the LPS is brought up to the desired pressure with, in case of experiments with methane, a mixture of 60% nitrogen

and 40% hydrogen. This mixture is chosen such that the contact surface formed in the tube will minimally reflect the expansion wave back into the HPS. Then for another 15 minutes the mixture is circulated through the HPS and mixing circuit to homogenize the gas-vapour mixture. Then, the mixing circuit is isolated from the HPS by closing valves V_2 and V_3 . At this moment the initial pressure and temperature of the HPS are recorded.

A 50 ms electrical pulse of 4×10^2 W in the ribbon starts the opening of the diaphragm, initiating the expansion wave and shock wave. For 32 ms the pressure, light scattering, extinction and reference signal are recorded with a sampling rate of 32 kHz by a Le Croy 6810 waveform recorder. In figs. 5.14 to 5.16 typical pressure, light scattering and extinction signals are shown for a *n*-octane/methane experiment with an initial pressure of 74 bar.

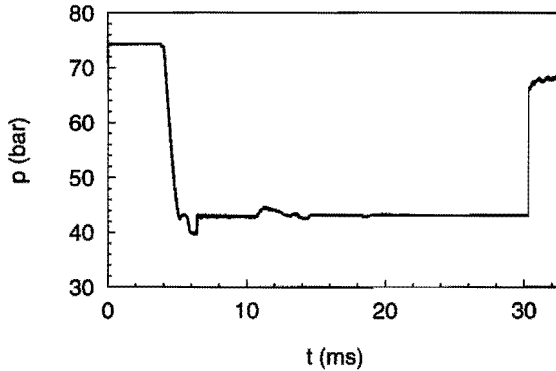


Figure 5.14: Typical pressure signal of a *n*-octane/methane high pressure experiment. The initial pressure in the HPS was 74 bar.

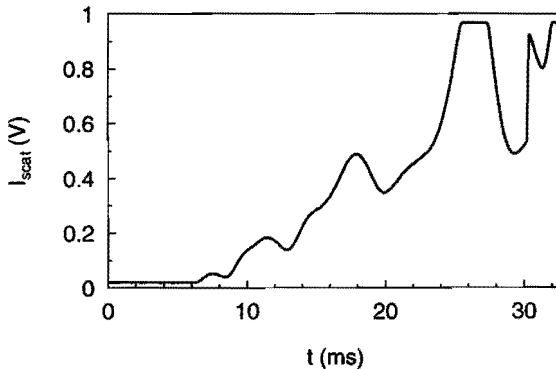


Figure 5.15: Typical light scattering signal of the *n*-octane/methane experiment. The fourth Mie-peak goes outside the range of the transient recorder. After 30 ms the shock wave stops the condensation process. The existing droplets start to evaporate.

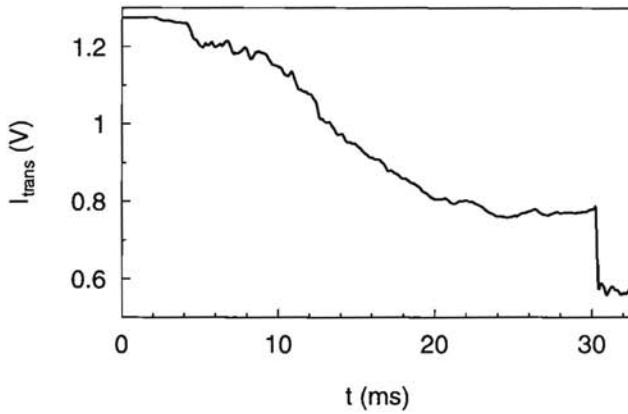


Figure 5.16: Typical extinction signal belonging to the high pressure *n*-octane/methane experiment. The fluctuations on the signal are probably due to Schlieren effects.

References

- BOHREN, C.F., & D.R. HUFFMAN. 1983. *Absorption and scattering of light by small particles*. New York: John Wiley & Sons.
- GYARMATHY, G. 1982. The spherical droplet in gaseous carrier streams: review and synthesis. In *Multiphase science and technology, 1*. Washington: Hemisphere Publishing Corporation.
- HUBBARD, G.L., V.E. DENNY, & A.F. MILLS. 1975. Droplet evaporation: effects of transients and variable properties. *Int. J. Heat Mass Transfer* **18**:1003–1008.
- KERKER, M. 1969. *The scattering of light and other electromagnetic radiation*. Academic Press, New York.
- LANDOLT-BÖRNSTEIN. 1962. *Zahlenwert und Funktionen*. Vol. II Band, 8. Teil. Berlin: Springer Verlag.
- MIE, G. 1908. Beitrage zur Optik trüber Medien speziell kolloidaler Metallösungen. *Ann. Phys.* **25**:377–445.
- N.V. NEDERLANDSE GASUNIE. 1988. *Physical properties of natural gases*. Groningen: N.V. Nederlandse Gasunie.
- OSWATITSCH, K. 1990. Verdampfen und Kondensieren binärer Gemische als Strömungsproblem. *Wärme und Stoffübertragung* **25**:45–58.
- PETERS, F., & B. PAIKERT. 1989. Nucleation and growth rates of homogeneously condensing water vapor in argon from shock tube experiments. *Exp. Fluids* **7**:521–530.
- REID, R.C., J.M. PRAUSNITZ, & B.E. POLING. 1987. *The Properties of Gases and Liquids*. New York: McGraw-Hill Book Company.

- RUDOLF, R. 1994. *Experimental investigation on condensation of supersaturated acid-water vapor mixtures by means of laser light scattering in a newly developed expansion chamber*. Ph.d. thesis, Universität Wien, Formal- und Naturwissenschaftlichen Fakultät.
- SMOLDERS, H.J. 1992. *Non-Linear wave phenomena in a gas-vapour mixture with phase transition*. Ph.d. thesis, TU Eindhoven, Eindhoven University of Technology, Faculty of Applied Physics.
- STREY, R., P.E. WAGNER, & Y. VIISANEN. 1994. The problem of measuring homogenous nucleation rates and the molecular contents of nuclei: Progress in the form of nucleation pulse experiments. *J. Phys. Chem.* **98**(32):7748-7758.
- SYCHEV, V.V., A.A. VASSERMAN, V.A. ZAGORUCHENKO, A.D. KOZLOV, G.A. SPIRIDONOV, & V.A. TSYMARNY. 1987. *Thermodynamic properties of methane*. Washington: Hemisphere publishing corporation.
- VAN DE HULST, H.C. 1981. *Light scattering by small particles*. New York: Dover.
- WAGNER, P.E., & R. STREY. 1984. Measurements of homogeneous nucleation rates for *n*-nonane vapor using a two-piston expansion chamber. *J. Chem. Phys.* **80**(10):5266-5275.
- YOUNG, J.B. 1993. The condensation and evaporation of liquid droplets at arbitrary Knudsen number in the presence of an inert gas. *Int. J. Heat Mass Transfer* **36**(11):2941-2956.

Chapter 6

EXPERIMENTAL RESULTS

6.1 Introduction

In the previous chapter we discussed the experimental techniques applied to measure homogeneous nucleation rates and droplet growth rates in a pulse expansion tube. This chapter deals with experimental results obtained with various gas mixtures. The measuring procedure is tested at low pressure with mixtures of nitrogen/water and nitrogen/*n*-nonane, the results are compared with literature data. From the vapours water and *n*-nonane a lot of nucleation rate data measured in a variety of apparatus is known from literature.

Next we will concentrate on high pressure experiments of the mixtures *n*-nonane/methane and *n*-octane/methane. Nucleation rates were measured under different conditions: total pressure, temperature, and mixture composition were varied. We shall compare the results with the classical model described in chapters 2 and 3, and with a new phenomenological model of Kalikmanov and Van Dongen (1995). From the data measured at constant temperature an estimate of the composition of the critical nucleus is made.

6.2 Homogeneous nucleation and droplet growth of water vapour in nitrogen

As a performance test for our new pulse expansion tube a series of experiments of water in nitrogen was carried out at more or less "standard" conditions; the expansion was initiated from a pressure slightly above atmospheric. In this type of experiments it is assumed that the mixture behaves ideally i.e. the droplets consist of pure water. The carrier gas nitrogen causes the necessary cooling rate and acts as a heat reservoir for the latent heat released by the condensing droplets. For the preparation of the mixture distilled water was used. The purity of the nitrogen gas was better than 99.999 %.

The experimental procedure followed in case of nucleation and droplet growth experiments with water vapour has been adapted in some ways with respect to the procedure described in chapter 5:

- The initial water vapour concentration in the tube is measured by a capacitive relative humidity gauge (Humicap HMP 124B).
- The droplet concentration is measured by means of the extinction method. At low pressure the position of the laser is much more stable. So, instead of a lens the pinhole with

diameter $\phi = 2$ mm (fig. 5.7) was installed. This limits the forward scattering angle to $\theta = 0.23^\circ$. In this situation the influence of light scattering on the extinction signal can be omitted completely.

- The temperature is calculated by means of the isentropic relation:

$$T = T_0 \left(\frac{p}{p_0} \right)^{\frac{\bar{\gamma}-1}{\bar{\gamma}}}. \quad (6.1)$$

In order to account for the influence of the presence of water vapour on the isentropic exponent $\bar{\gamma}$, it is averaged over the mixture components according to

$$\bar{\gamma} = \frac{\bar{c}_p}{\bar{c}_p - R}, \quad (6.2)$$

where \bar{c}_p is the averaged isobaric molar specific heat of the mixture. The corrections in temperature carried out by the averaging are of the order of 0.1 K.

- The initial pressure is measured by a Druck PDCR 81 piezo resistive pressure transducer.

Typical theoretical and measured light scattering and extinction signals of an experiment with water/nitrogen are given in Figs. 6.1 and 6.2.

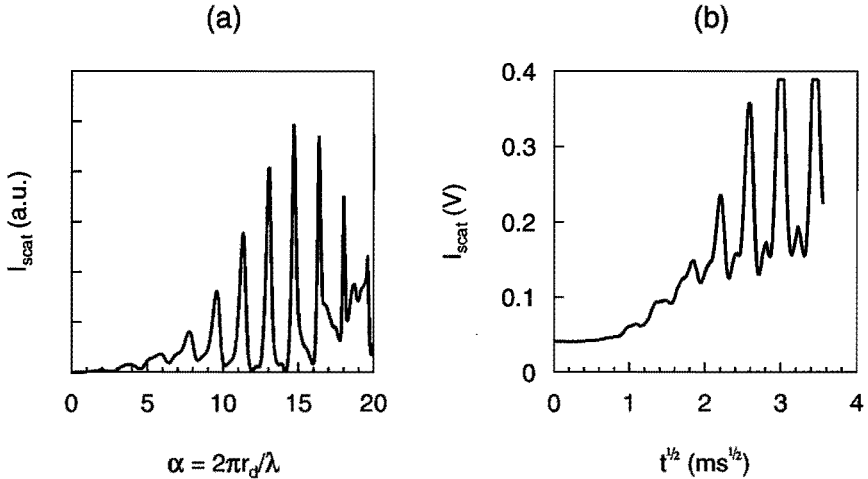


Figure 6.1: Theoretical Mie pattern (a) and experimental Mie signal (b) of water droplets. Note the different x -scales. The peculiarly peaked behaviour with finestructures predicted by the theory is clearly observed in the experimental signal. In the experimental signal also a DC component appears. This is probably due to internal reflections of the laser beam inside the expansion tube. The experimental conditions in the nucleation pulse were: $T = 240.9$ K, $p = 0.62$ bar, water vapour pressure $p_v = 5.1 \times 10^2$ Pa, and droplet number density $n_d = 2.0 \times 10^{11}$ m $^{-3}$.

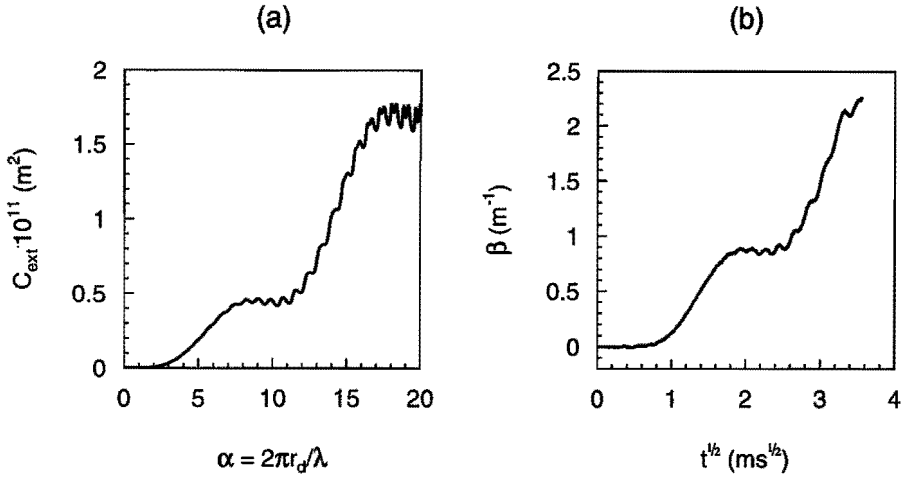


Figure 6.2: Theoretical extinction cross section (a) and experimental extinction signal (b) due to growing water droplets. Experimental conditions as in Fig. 6.1.

Nucleation rates

A series of experiments was performed at various nucleation temperatures and vapour pressures. The initial pressures of the HPS were between 1.2 and 1.5 bar, the initial temperature was room temperature. The variation in nucleation temperature was attained by varying the expansion depth. The results are shown in the $p - T$ diagram of Fig. 6.3. Each position of a solid marker represents the thermodynamic state of the water vapour during the nucleation pulse for one experiment. The marker shape indicates the order of magnitude of the nucleation rate measured. The nucleation rates range from $1 \times 10^7 \text{ cm}^{-3}\text{s}^{-1}$ to $1 \times 10^{11} \text{ cm}^{-3}\text{s}^{-1}$. The supersaturations required for these nucleation rates vary with temperature, from about 8 at 255 K to 80 at 200 K. This latter figure must be handled with care however. To calculate the supersaturation the vapour-liquid equilibrium curve of water vapour (appendix A) has to be extrapolated down to these low temperatures, which is of course a precarious enterprise, because this is as much as 70 K below the triple point of water. To express the deviation from equilibrium by the undercooling (the temperature difference between Wilson point and saturation curve at equal vapour pressure) is less speculative. The undercooling for the nucleation temperatures ranges from 30 K to 35 K. To get an impression of the experimental uncertainty, data of three experiments are listed in table 6.1. A table of all nucleation experiments can be found in appendix D.

In the diagram also nucleation experiments of others are depicted. From the enormous amount of data on nucleation of water we selected the data of Peters and Paikert (1989) and of Viisanen *et al.* (1993). The data series of Peters and Paikert denoted by the solid curve were obtained in an expansion tube very similar to ours. The curve roughly indicates the thermodynamic state at which the nucleation rate was circa $1 \times 10^8 \text{ cm}^{-3}\text{s}^{-1}$. From 230 K to 260 K this data series coincides with our measurements. Below 230 K Peters and Paikert measured a decreasing supersaturation with temperature which does not agree with our experiment.

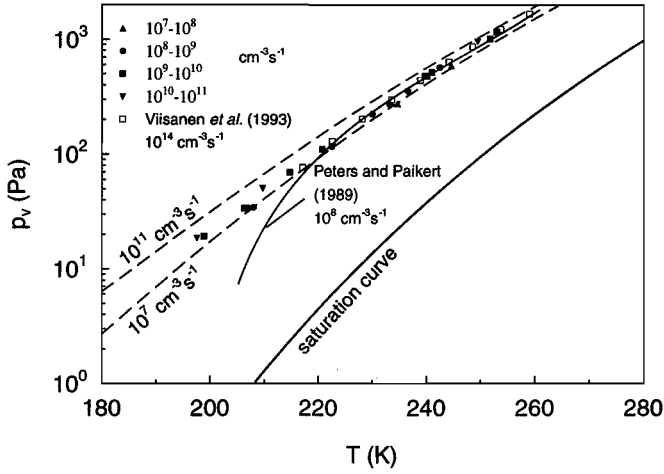


Figure 6.3: $p_v - T$ state diagram with of water. Solid markers, present nucleation data of water vapour in nitrogen. The marker position denotes the vapour pressure and the temperature during the nucleation pulse. The marker shape is an indication of the measured nucleation rate. Open markers, data of Viisanen *et al.* (1993). Solid curve, data of Peters and Paikert 1989). Dashed curves, lines of constant nucleation rate according to the Classical Nucleation Theory.

| p_v (Pa) | T (K) | J ($\text{cm}^{-3}\text{s}^{-1}$) |
|--------------------------------------|-----------------|---------------------------------------|
| 19 ± 3 | 199 ± 1 | $9 \times 10^9 \pm 7 \times 10^9$ |
| 222 ± 6 | 230.1 ± 0.9 | $5 \times 10^8 \pm 1 \times 10^8$ |
| $1.16 \times 10^3 \pm 3 \times 10^1$ | 252.9 ± 0.8 | $7 \times 10^9 \pm 2 \times 10^9$ |

Table 6.1: Experimental uncertainty of the thermodynamic state of water vapour during the nucleation pulse and of the corresponding nucleation rate, for three experiments at different conditions.

The data of Viisanen *et al.* were recently obtained in a two piston expansion chamber. They measured very accurately several series of nucleation rates, each series at a fixed temperature at nine different temperatures and for three different carrier gases. Some of the data, those that belong to a nucleation rate near to $1 \times 10^8 \text{ cm}^{-3}\text{s}^{-1}$, are depicted in the diagram by the open squares. Their data coincide with ours.

In the diagram also two curves representing the unary Classical Nucleation Theory are drawn. The curves of constant nucleation rate give the thermodynamic vapour state at which the nucleation rate has a value of $1 \times 10^7 \text{ cm}^{-3}\text{s}^{-1}$ and $1 \times 10^{11} \text{ cm}^{-3}\text{s}^{-1}$, respectively. All experimental data are supposed to fall between the curves, which appears to be so for the whole range of temperatures, indicating that CNT predicts the measured nucleation rates rather correctly. Later on we will revert to the comparison between experiment and nucleation theory.

droplet growth

The droplet growth phase of a quintet experiments is shown in Fig. 6.4. The circles represent

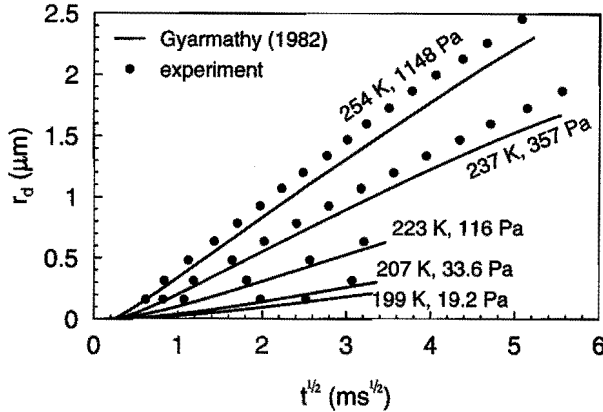


Figure 6.4: Droplet growth of water vapour in nitrogen. Circles, experiment. Curves, calculations according to the droplet growth model of Gyarmathy (1982). The labels denote the water vapour state during the nucleation pulse.

the Mie-peaks in the light scattering signal, the solid curves are droplet growth calculations according to a droplet growth model based on Gyarmathy's model, which is described by Paikert (1990). This droplet growth model assumes ideal behaviour of the water/nitrogen mixture, but Knudsen effects are taken into account. The origin of the time axis is taken in the middle of the nucleation pulse. In the continuum regime the so called "quadratic growth law" is valid, i.e. the increase of droplet radius squared is proportional to time:

$$dr_d^2 \propto dt, \quad (6.3)$$

and therefore along the x -axis \sqrt{t} is plotted. It is possible to discern between three distinguishable regimes in the droplet growth process. During the first stage of droplet growth when droplet radii are less than $0.3 \mu\text{m}$, Knudsen effects are important; this is expressed in a linearly increasing droplet radius with time. Droplets larger than $0.3 \mu\text{m}$ can be considered to be in the continuum regime, the square of the droplet radius increases proportional with time, according to the "quadratic growth law". After some time, depending on the amount of water vapour present, vapour depletion is noticeable, which results in a decrease of the droplet growth rate. The droplet growth rate of the "237 K, 357 Pa experiment" starts to diminish above a droplet size of $r_d = 1.2 \mu\text{m}$.

The decrease of droplet growth rate with decreasing temperature is due to the temperature dependency of the diffusion coefficient.

Furthermore, it turns out that there is a discrepancy between experiment and theory of about 10% over the whole range of temperatures and vapour pressures, whereas Peters and Paikert (1989, 1994) found excellent agreement between the same growth model and their measurements. The apparent discrepancy between our measurements and the growth model is very

probably caused by an error in the vapour pressure determination due to an unexpected sensitivity of the relative humidity sensor to the total gas pressure. Since the humidity sensor was calibrated in pure water vapour, this sensitivity yields slightly erroneous values at atmospheric pressures.

We now return to the nucleation results. Since there was no reason to believe that the droplet growth model were not correct, the experimental vapour pressure has been deduced from the droplet growth experiment. The original vapour pressure values were multiplied by a factor 1.1 and Fig. 6.3 was recalculated. The result is shown in Fig. 6.5. Due to the logarithmic

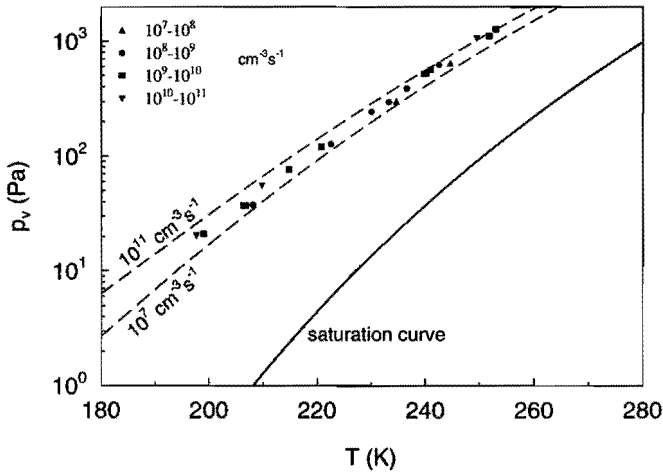


Figure 6.5: $p_v - T$ state diagram with nucleation rates of water in nitrogen with corrected vapour pressure (markers). Dashed curves, lines of constant nucleation rates according to the Classical Nucleation Theory.

p_v -axis there is only a very small change, but the experimental points seem to fit better with the theoretical curves.

A more detailed analysis of the water vapour nucleation experiments is shown in Fig. 6.6. The ratio of measured nucleation rates J_{exp} and theoretical nucleation rates J_{th} is depicted for (a) the unary Classical Nucleation theory and (b) the semi-phenomenological nucleation theory of Dillmann and Meier (1991) (DMT) as a function of the nucleation temperature. The formulas used to do the calculations for these theories are listed in appendix C. Both our corrected measurements (solid markers) and the data of Viisanen *et al.* (1993) with a nucleation rate near to $1 \times 10^8 \text{ cm}^{-3}\text{s}^{-1}$ are drawn in the figure (open markers).

Several conclusions can be drawn. First, a very good agreement is observed between our measured nucleation rates and those of Viisanen *et al.*. The scatter in our data series is a factor three larger than the scatter in Viisanens data, which indicates that the reproducibility in the expansion tube is a little less than in the two-piston expansion chamber, but better than one order of magnitude in nucleation rate. Nevertheless, the magnitudes of the measured nucleation rates correspond excellently over the temperature range 217 K – 260 K.

In the theoretical calculations corresponding to the expansion tube experiments the cor-

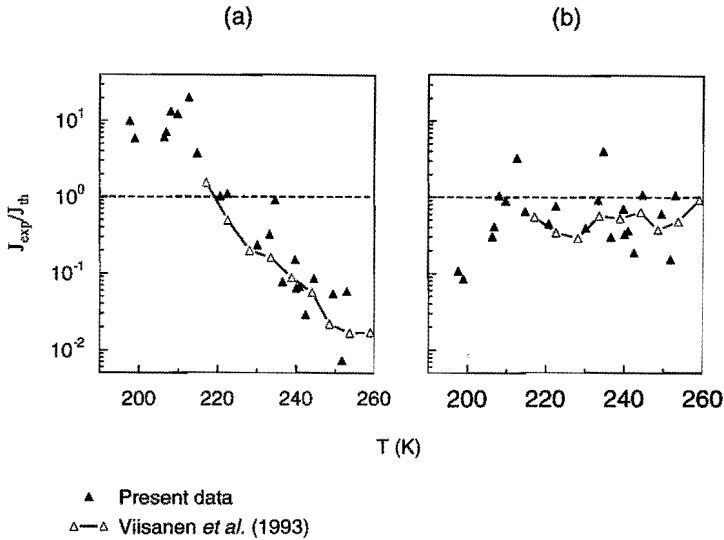


Figure 6.6: Comparison of experimental nucleation rates to Classical Nucleation Theory (a) and Dillmann–Meier Theory (b). Depicted are the ratios of the measured nucleation rate and the theoretical nucleation rate calculated at the same conditions p_v and T .

rected nucleation vapour pressure was used. So, actually the vapour pressure was fitted to the droplet growth rate. Hence, from the accordance with Viisanens data we conclude that the droplet growth method to obtain the vapour pressure yields the correct result for water vapour, which gives further confidence in applying this method to high pressure experiments.

Finally, examining the differences between the classical theory and the theory of Dillmann and Meier, we observe at low temperatures an underestimate of the nucleation rate by CNT by one order of magnitude, and an overestimate by two orders of magnitude at high temperatures, whereas DMT predicts correctly the nucleation rate over the whole temperature range. The observation that the discrepancy between the nucleation rates predicted by CNT, and experimentally obtained values, varies with temperature has been confirmed by several investigations. Also the improved temperature dependence of the predicted nucleation rates by DMT, which is expressed by the zero slope of J_{exp}/J_{th} in diagram (b), is found for other substances.

6.3 Homogeneous nucleation and droplet growth of *n*-nonane

The second vapour studied in the expansion tube at low pressure concerns the hydrocarbon *n*-nonane, which consists of chain molecules with 9 carbon molecules and 20 hydrogen molecules. At room temperature its vapour pressure is about 400 Pa. This vapour has become a key substance in nucleation studies, on one hand because reliable nucleation data obtained in different devices are well documented in literature, and on the other hand the classical nucleation theory is orders of magnitude wrong in predicting nucleation rates, so that *n*-nonane became a sort of

test substance of nucleation theories.

The experimental procedure is similar to the procedure followed with the water experiments except for the *n*-nonane vapour fraction determination. After the injection of liquid *n*-nonane (Merck, purity > 98 %) in the tube, typical injection volumes range from 50 to 300 μl , the vapour was allowed to establish an adsorption equilibrium with the tube walls for half an hour. Then the vapour pressure was measured with a pressure gauge (Barocel type 600 A). This vapour pressure was corrected for leakage into the tube and assumed not to change during inlet of the carrier gas nitrogen and thus considered to be the initial partial vapour of the experiment.

A Mie scattering signal and measured extinction coefficient of growing *n*-nonane droplets are given in Figs. 6.7 and 6.8. Theoretical patterns were calculated with a refractive index of 1.405 (Landolt-Börnstein 1962)

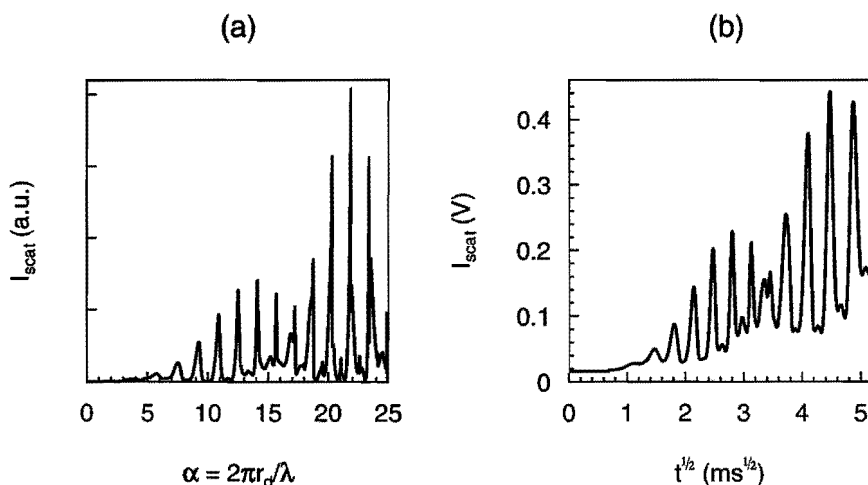


Figure 6.7: Theoretical Mie pattern (a) and experimental Mie signal (b) of *n*-nonane droplets. Conditions during the nucleation pulse: $p = 0.386$ bar, $T = 222.1$ K, $p_v = 89$ Pa, $n_d = 7 \times 10^{10} \text{ m}^{-3}$.

In the $p - T$ diagram of Fig. 6.9 the Wilson points measured in the pulse expansion tube are depicted. Again the position of the markers represent the *n*-nonane vapour state (partial vapour pressure and temperature) in the nucleation pulse. The shape of the markers refers to the nucleation rate. The Wilson points are arranged in a band at a temperature about 50 K below the saturation temperature. The corresponding supersaturations are of the order of 200. Among the data of the expansion tube also three measurements of Wagner and Strey (1984) performed in a two-piston cloud chamber are shown (open squares). The nucleation rate of these points was near to $1 \times 10^9 \text{ cm}^{-3}\text{s}^{-1}$. The supersaturation agrees fairly well with our measurements. The theoretical nucleation rates are represented by the dotted curve (CNT) and the dashed curve (DMT). The labels next to the curves denote the nucleation rate in $\text{cm}^{-3}\text{s}^{-1}$. It is clear that the nucleation rates predicted by DMT are far better than those predicted by CNT. At 220 – 230 K the measured Wilson points fall in between the two DMT curves while CNT over the whole temperature range largely underestimates the nucleation rate.

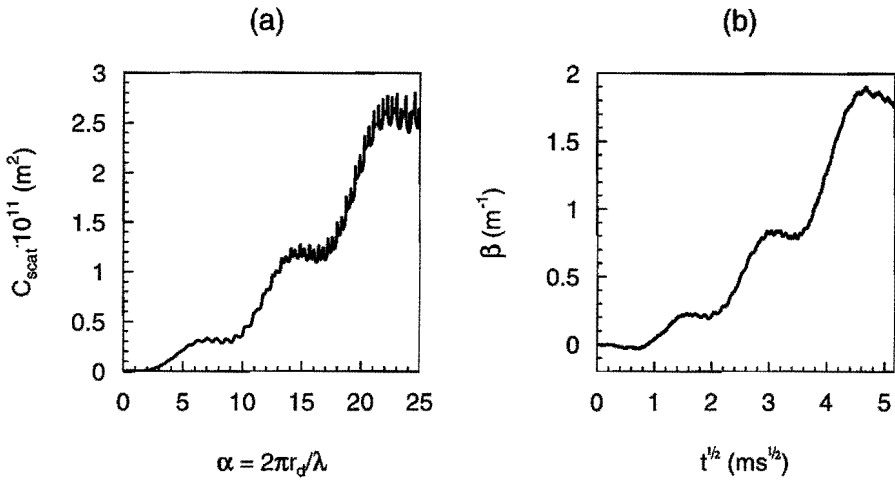


Figure 6.8: Theoretical extinction cross section (a) and experimental extinction signal (b) of growing *n*-nonane droplets. Conditions as in Fig. 6.7.

Nonane droplet growth is shown in Fig. 6.10. Four experimental growth curves are accompanied by calculated growth curves. The theoretical curves are the exact solution of the Eqs. (5.15) and (5.16) of Gyarmathy's growth model. We observe a decreasing droplet growth rate with decreasing temperature and vapour pressure. The diffusion of *n*-nonane in nitrogen is slowed down because of a decreased diffusion coefficient at lower temperature, and a decreased concentration gradient of *n*-nonane due to the lower nonane fraction in the mixture.

At the *x*-axis again the square root of the time is plotted. An increasing growth rate in the Knudsen regime is observed for droplets with a radius smaller than 0.3 μm , larger droplets

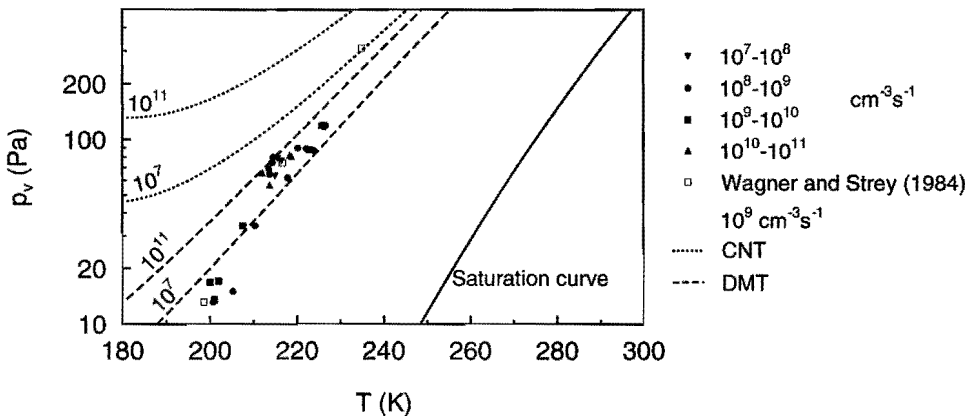


Figure 6.9: $p_v - T$ state diagram of *n*-nonane with Wilson points and theoretical lines of constant nucleation rates according to CNT and DMT.

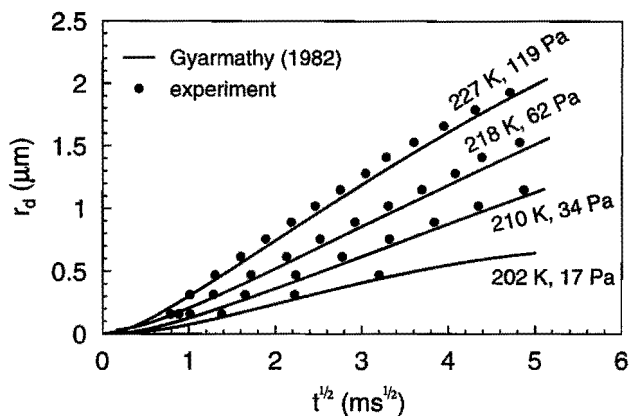


Figure 6.10: Growth rates of *n*-nonane in nitrogen. Labels denote the temperature and *n*-nonane vapour pressure during the nucleation pulse.

satisfy the “quadratic growth law” of Eq. (6.3). The flattening that is exhibited by the lowest curve at larger times is caused by *n*-nonane vapour depletion.

Once more experimental growth rates appear to be larger than theoretical growth rates (by about 5%) although the vapour pressure was measured in a different way in comparison to the water experiments. It is very likely this time that the assumption of a constant *n*-nonane vapour pressure during the filling of the tube with the carrier gas nitrogen is invalid. After the injection of *n*-nonane into the HPS a large amount, up to 10 times as much as the remaining *n*-nonane in the gaseous phase, was adsorbed on walls. Due to the pressure increase caused by the supply of nitrogen, the chemical potential of the adsorbed *n*-nonane is raised. So, the *n*-nonane will tend to leave the walls and evaporate into the gas phase. Therefore, the vapour concentration will be somewhat higher than was assumed, leading to a larger growth rate.

This brings the section of test experiments to an end. We conclude that the pulse expansion tube and the procedures followed, lead to results very much in accordance with literature data obtained with shock tubes and piston expansion chambers.

6.4 High pressure nucleation and droplet growth in hydrocarbon mixtures

Up to now, only very little experimental work on high pressure nucleation was reported in literature. In a diffusion cloud chamber study of Heist *et al.* (1994) nucleation rates of 1-propanol were measured in hydrogen and helium, but in contrast to the present investigations it was implicitly assumed that the mixtures behaved ideally, i.e., the carrier gas was not present in the nucleating droplets. Kalikmanov and van Dongen (1995) developed a semi-phenomenological nucleation model based on Fisher’s theory (1967) that can be used in the supercritical region of binary mixtures. The implementation of real gas effects in the Classical Nucleation Theory was described in chapter 2. In this section experimental results of *n*-nonane in methane and *n*-octane in methane are presented and compared with both nucleation theories.

6.4.1 Nucleation and droplet growth in *n*-nonane/methane

The first mixture that we consider is the *n*-nonane/methane mixture. The equilibrium phase behaviour of this mixture is shown in the two diagrams of Fig. 6.11. Diagram (a) shows the

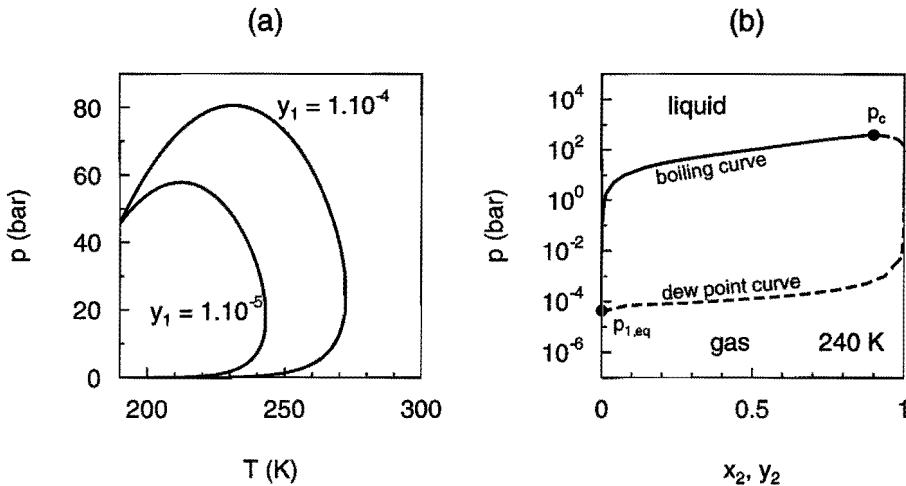


Figure 6.11: Phase diagrams of *n*-nonane/methane. (a), $p - T$ diagram with two coexistence curves of mixtures with *n*-nonane molar fraction as denoted by the labels. (b), $p - x$ diagram, with boiling curve and dew point curve versus methane molar fraction in liquid and vapour, respectively, at fixed $T = 240$ K. This latter diagram was calculated with the Peng-Robinson equation of state (NIST 1990).

vapour-liquid coexistence curve in the $p - T$ plane at two fixed compositions namely with $y_1 = 1 \times 10^{-4}$ and $y_1 = 1 \times 10^{-5}$. In the area enclosed by the coexistence curve, which is also called coexistence envelope, the mixture of given composition can attain an equilibrium state with both vapour and liquid present. This is all analogous to the phase behaviour of natural gas. A different view is given by diagram (b)¹ in which the equilibrium pressure is plotted versus the methane molar fraction in the liquid x_2 or in the gas y_2 which depends on the state of the mixture, at a fixed temperature of 240 K. Below the lower curve the mixture is in the gaseous phase, above the upper curve the mixture is in the liquid phase, in between the gas phase of the mixture is in coexistence with the liquid phase. On the left y -axis where the liquid contains only *n*-nonane the boiling curve and dew points curve come together at the pure vapour pressure *n*-nonane. Since at a temperature of 240 K no pure liquid methane exists, the curve does not make contact with the right y -axis. Boiling curve and dew point curve come together at a point for which $x_2 < 1$. Since in this point there is no visible meniscus, it is called the critical point in analogy to pure vapours.

For the representation of the experimental data we use the supersaturation parameter $S = y_1/y_{1,eq}$, introduced in Eq. (3.9). So, the vapour fraction *n*-nonane y_1 is the equilibrium property

¹As an exception, diagram (b) was calculated with the Peng-Robinson equation of state on the basis of a commercial data base (NIST 1990).

that we are most interested in. The equilibrium vapour fraction $y_{1,eq}$ is calculated with the RKS equation of state. Unfortunately, only the already mentioned data of Shipman and Kohn (1966) were found in the literature, but they lack the desired accuracy to compare to our calculated *n*-nonane vapour fractions. Therefore, we have to restrict ourselves to the remark that calculated RKS equilibrium *n*-decane vapour fractions do not depart more than 10% from equilibrium data measured by Rijkers *et al.* (1992) under similar conditions. We consider the calculated RKS data for *n*-nonane/methane as reliable as for the mixture *n*-decane/methane.

Nucleation rate measurements were performed for the mixture *n*-nonane/methane at various pressures, temperatures, and vapour fractions *n*-nonane. The injected liquid *n*-nonane was of a purity > 98% (Merck), while the methane gas was of a purity > 99.995%.

Droplet growth

First, a plot of four growth curves of droplets in *n*-nonane/methane is shown in Fig. 6.12. The

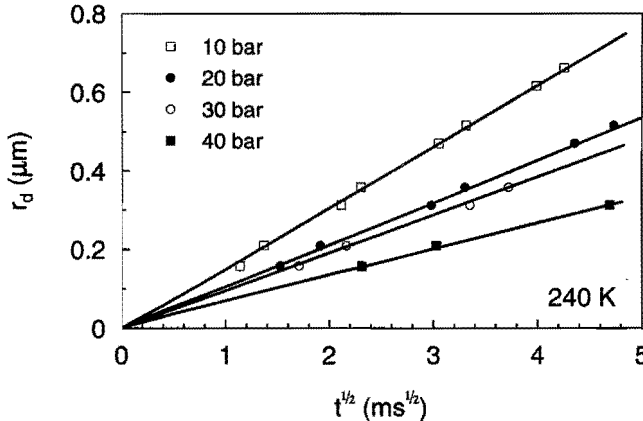


Figure 6.12: Droplet growth rates of *n*-nonane/methane at various pressures, and fixed $T = 240$ K. Markers, experiment. Solid curves, calculations according to the high pressure limit of the droplet growth model. In these calculations the vapour fraction *n*-nonane was chosen such that optimum agreement with the experiment was obtained.

labels denote the total pressure in the nucleation pulse, the temperature was approximately 240 K in all cases. The time origin was taken to be in the middle of the nucleation pulse. The markers indicate the positions of the peaks and valleys in the Mie scattering signal. It must be noted here that the theoretical Mie pattern to which the experimental pattern is compared, was calculated with a refractive index of 1.405 which belongs to pure liquid *n*-nonane. The influence of methane in the droplet on the refractive index is unknown, but since the shapes of the measured and calculated Mie patterns agree very well, it is not to be expected that a significant error is made. The experimental growth curves perfectly satisfy the quadratic growth law. The solid curves are calculated according to the high pressure limit of the growth model of chapter 5; the *n*-nonane fraction y_1 of the mixture was chosen such that optimal agreement

between experimental and theoretical curves was achieved. For each experiment, the y_1 value obtained in this way is used in representing the nucleation rate data.

Nucleation rates

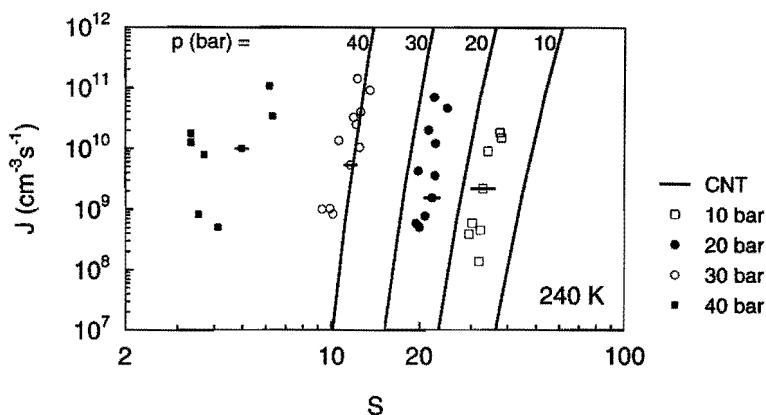


Figure 6.13: Measured nucleation rates of *n*-nonane/methane versus supersaturation. The markers indicate the total pressure in the nucleation pulse; the nucleation pulse temperature was in all cases approximately 240 K. The horizontal lines added to some experimental points reflect the experimental uncertainty of the supersaturation. The relative uncertainty of the nucleation rate value is about $\pm 20\%$, which roughly corresponds to the vertical size of the markers.

Results on homogeneous nucleation are depicted in Fig. 6.13, the measured nucleation rates are plotted as a function of *n*-nonane supersaturation S for different pressures. The temperature in the nucleation pulse was in all cases near to 240 K.

Besides a natural increase of nucleation rate with supersaturation for each pressure, it appears that the supersaturation of *n*-nonane, required for a given nucleation rate, decreases strongly with increasing pressure. This must be considered a very important result; it clearly demonstrates a strong influence of methane on the nucleation process. Fig. 6.13 also shows theoretical nucleation rates according to calculations based on the binary Classical Nucleation Theory. A significant difference is found between experiment and theory. Still, experiment and theory exhibit the same general behaviour of decreasing supersaturation with increasing pressure.

Furthermore, the larger scatter of supersaturations of the 40 bar experiment is eye-catching. A definitive explanation has not been found yet. Possibly, it has to do with the low vapour pressure of *n*-nonane, so that other vapours, present in small amounts in the methane gas, influence nucleation. We tried to find an indication for this, but experiments with methane gas with an impurity as high as 10^{-3} did not give results significantly different, so no proof was found.

The temperature in the nucleation pulse was approximately 240 K. In reality the nucleation temperature differed from one experiment to the other over a range from 238 K to 243 K.

This scatter in nucleation temperature largely causes the scatter in Fig. 6.13. In order to diminish the effect of a nucleation temperature deviating from 240 K, a correction factor $\Delta \ln S$ is introduced:

$$\Delta \ln S = \Delta T \left. \frac{\partial \ln S}{\partial T} \right|_{J,p} . \quad (6.4)$$

ΔT is the deviation from 240 K. A point in the $J - S$ plane is shifted in the S -direction according to Eq. (6.4). The derivative in the equation is calculated on the basis of the binary Classical Nucleation Theory. The consequence of this correction factor can be seen in Fig. 6.14. Especially for the 10 to 30 bar experiments the scatter has diminished considerably.

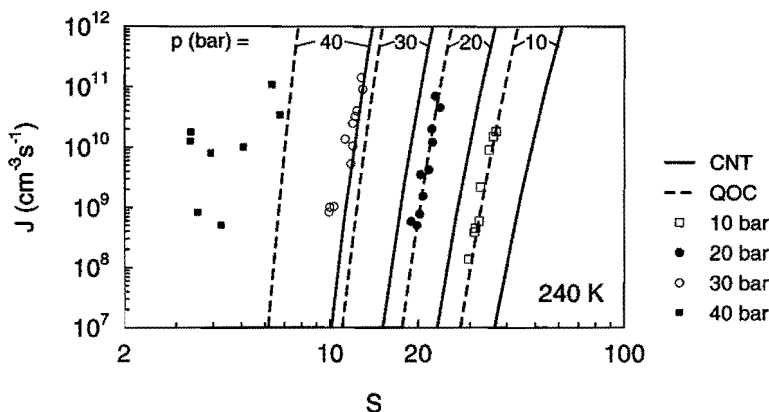


Figure 6.14: Nucleation rates of *n*-nonane/methane versus supersaturation corrected for temperature deviations from 240 K in the nucleation pulse. Also theoretical curves are drawn according to CNT, and to a Quasi-One-Component semi-phenomenological model (QOC), recently described by Kalikmanov and Van Dongen (1995).

In Fig. 6.14 also nucleation rates calculated according to a recently described nucleation theory by Kalikmanov and Van Dongen (1995) are drawn. This theory belongs to the class of so-called semi-phenomenological theories. The ideas behind these theories originate from the unary nucleation theory formulated by Dillmann and Meier (1991). They described the Gibbs formation free energy of a cluster on the basis of a cluster model of Fisher (1967), and introduced a new free parameter that corrects for possible deviations of the cluster surface tension from the equilibrium surface tension. The parameters of the Fisher model and the surface tension correction were calculated from the critical point properties of the vapour of interest, and by constructing a relation between the new model and the real equation of state.

The model of Kalikmanov and Van Dongen (referred to as "QOC") is a modification of the Dillmann–Meier Theory for binary systems. The binary mixture is reduced to a quasi-one-component system, and it is applicable in the coexistence region of real mixtures. Calculations for the *n*-nonane/methane mixture are represented by the dashed curves in Fig. 6.14. It appears that predictions of QOC are improved compared to CNT for this mixture at 240 K.

The value of the *n*-nonane supersaturation of course depends on the saturated vapour pressure of *n*-nonane, which varies strongly with total pressure. So as an alternative representation, nucleation rate is plotted versus *n*-nonane molar density in fig. 6.15. The results at 40 bar are

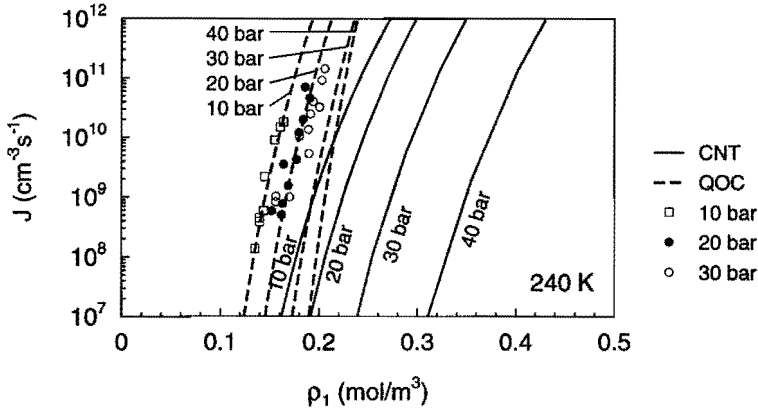


Figure 6.15: Nucleation rate versus (temperature corrected) molar density for *n*-nonane/methane at 240 K.

not in the diagram because of the larger scatter. Here, all data almost overlap within the experimental uncertainty. Assuming the correctness of the droplet growth model, the explanation could be the following: with a fixed *n*-nonane density, adding methane results both into a lowering of the supersaturation, and into dissolving of methane in the critical droplets which lowers the surface tension. These two effects have an opposing influence on nucleation rate.

Figures 6.16 and 6.17 show nucleation rates of *n*-nonane/methane at 230 K and 250 K. Striking again are the very low supersaturations measured at 230 K and 40 bar. For all conditions, QOC predictions of nucleation rate are shifted to lower supersaturations compared to CNT predictions, but this does not mean an improvement in all circumstances.

As an illustration we applied the method described by Oxtoby and Kashchiev (1994) to deduce the excess number of molecules n_i^* of both species in the critical nucleus:

$$\Delta n_i^* \approx \left[\frac{\partial(k_B T \ln J)}{\partial \mu_{0,i}} \right]_T, \tag{6.5}$$

where $\mu_{0,i}$ is the chemical potential of component *i* in the gas mixture, and k_B is Boltzmann's constant. The excess number represents the extra number of molecules that is present in a volume containing a critical cluster, over the number of molecules that occupied the same volume before the critical cluster was formed. Results at $T = 240$ K are given in table 6.2. The excess numbers of methane molecules in the cluster were estimated from a linear interpolation between measurements at different pressures.

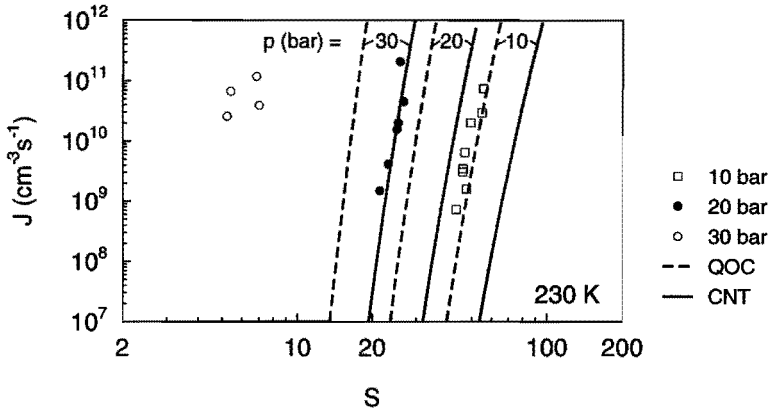


Figure 6.16: Nucleation rate versus supersaturation of *n*-nonane/methane at 230 K.

6.4.2 Nucleation and droplet growth in *n*-octane/methane

A second mixture that was studied at high pressure is *n*-octane/methane. The advantage of using *n*-octane above *n*-nonane is the higher vapour pressure. The phase diagrams of *n*-octane/methane are given in Fig. 6.18.

Droplet growth

Droplet growth curves of *n*-octane/methane are displayed in Fig. 6.19. Due to the larger *n*-octane vapour fraction the droplets grow remarkably faster than did the *n*-nonane/methane droplets. The theoretical Mie pattern was calculated with the pure liquid *n*-octane refrac-

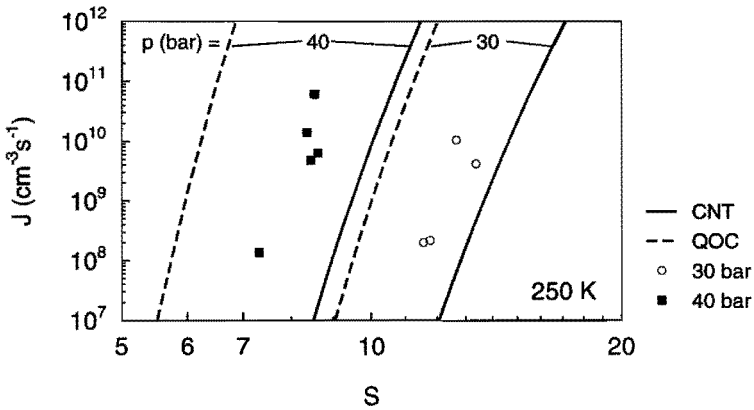


Figure 6.17: Nucleation rate versus supersaturation of *n*-nonane/methane at 250 K.

| p (bar) | n-nonane | methane |
|---------|------------|---------|
| 10 | 24 ± 2 | 20 |
| 20 | 24 ± 3 | 30 |
| 30 | 18 ± 2 | 40 |
| 40 | 12 ± 7 | 40 |

Table 6.2: Excess number of molecules in the critical cluster at 240 K, calculated according to the relation of Oxtoby and Kashchiev (1994). The values in the last column only give a rough indication of the number of methane molecules.

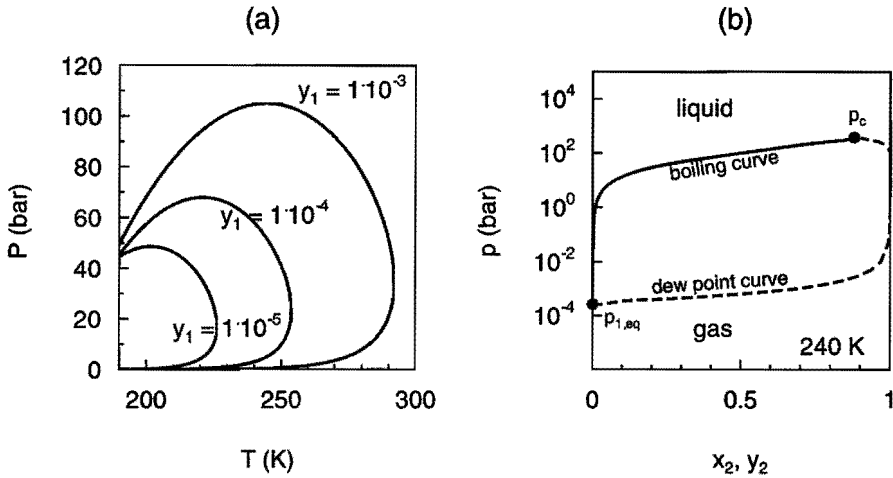


Figure 6.18: Phase diagrams of *n*-octane/methane. (a), $p - T$ diagram with three coexistence curves of mixtures with *n*-nonane molar fraction as denoted by the labels. (b), $p - x$ diagram, with boiling curve and dew point curve versus methane molar fraction in liquid and vapour, respectively, at fixed $T = 240$ K. Diagram (b) was calculated with the Peng-Robinson equation of state (NIST 1990).

tive index of 1.395 (Landolt-Börnstein 1962). The solid curves are again the best fits to the experimental growth curves.

A check was made whether the high pressure limit was applicable in this situation for the 10 bar experiment. The 10 bar curve was calculated with the high pressure limit approximation, and by exactly solving Eqs. (5.15) and (5.16). Both curves are in the diagram, but they appear to be indistinguishable; at 29.5 ns the difference is less than 0.1 %. So, we conclude that the high pressure limit may be used also at pressures 20 bar to 40 bar.

Nucleation rates

Nucleation rates of *n*-octane/methane at 240 K are given in the $J - S$ diagram of Fig. 6.20. Again the experimental results are compared with the Classical Nucleation Theory and the Quasi-One-Component theory. The supersaturations required for nucleation rates between

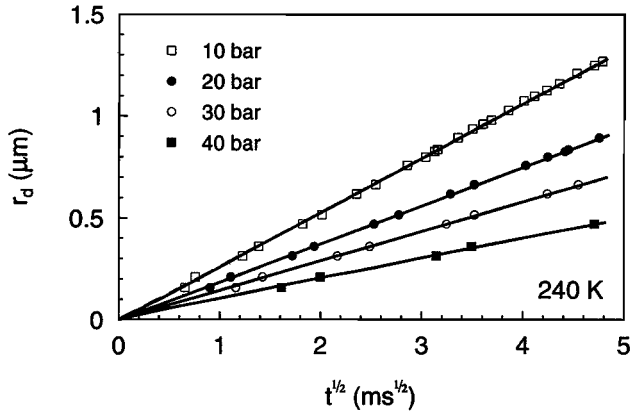


Figure 6.19: Droplet growth of *n*-octane/methane at $T = 240$ K. Markers, experiment. Solid lines, droplet growth according to the high pressure limit. The calculations were fitted to the experimental growth rates by varying the vapour composition.

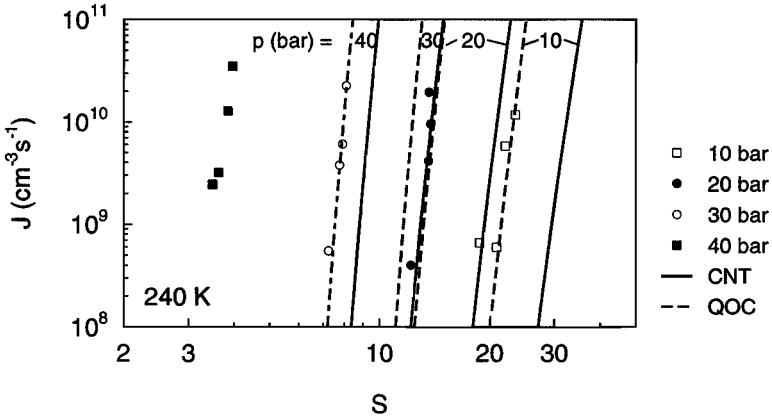


Figure 6.20: Nucleation rates of *n*-octane/methane versus supersaturation at $T = 240$ K. Markers, experiment. Solid curves, binary Classical Nucleation Theory. Dashed curves, Quasi-One-Component nucleation theory.

$10^9 \text{ cm}^{-3}\text{s}^{-1}$ and $10^{11} \text{ cm}^{-3}\text{s}^{-1}$ are somewhat below the *n*-nonane supersaturations. Finally, the nucleation rate is plotted versus *n*-octane molar density in Fig. 6.21. A similar pattern is

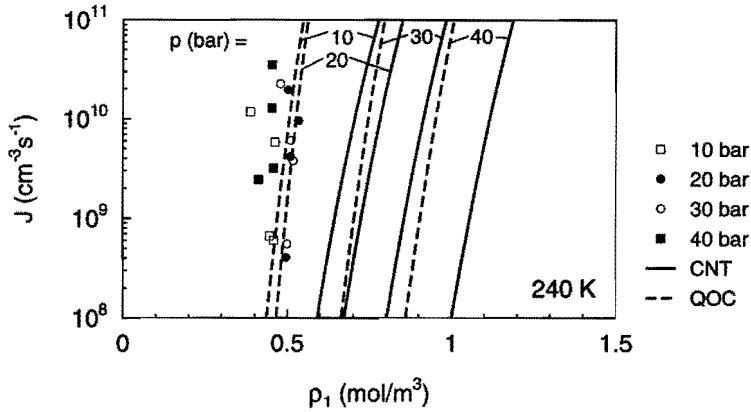


Figure 6.21: Nucleation rates of *n*-octane/methane as a function of *n*-octane vapour density.

found as in Fig. 6.15. The *n*-octane vapour density for which the nucleation rate is between $10^8 \text{ cm}^{-3}\text{s}^{-1}$ and $10^{11} \text{ cm}^{-3}\text{s}^{-1}$ appears to be about the same for all pressures.

References

- DILLMANN, A., & G.E.A. MEIER. 1991. A refined droplet approach to the problem of homogeneous nucleation from the vapor phase. *J. Chem. Phys.* **94**(5):3872–3884.
- FISHER, M.E. 1967. The theory of condensation and the critical point. *Physics* **3**:255–283.
- HEIST, R.H., M. JANJUA, & J. AHMED. 1994. Effects of background gases on the homogeneous nucleation of vapors. 1. *J. Phys. Chem.* **98**(16):4443–4453.
- KALIKMANOV, V.I., & M.E.H. VAN DONGEN. 1995. Quasi-one-component theory of homogeneous binary nucleation. *Phys. Rev. E* **51**:in press.
- LANDOLT-BÖRNSTEIN. 1962. *Zahlenwert und Funktionen*. Vol. II Band, 8. Teil. Berlin: Springer Verlag.
- NIST. 1990. *NIST Thermophysical properties of hydrocarbon mixtures database*. National Institute of Standards and Technology, Gaithersburg, Maryland 20899.
- PAIKERT, B. 1990. *Untersuchung der Kondensation und Verdampfung ruhender Tropfen in Gas-Dampf-Gemischen mit Hilfe eines Stoßwellenrohres*. Ph.d. thesis, Universität Essen, Fakultät Maschinentechnik.
- PETERS, F., & B. PAIKERT. 1989. Nucleation and growth rates of homogeneously condensing water vapor in argon from shock tube experiments. *Exp. Fluids* **7**:521–530.
- PETERS, F., & B. PAIKERT. 1994. Measurement and interpretation of growth and evaporation of monodispersed droplets in a shock tube. *Int. J. Heat Mass Transfer* **37**(2):293–302.

- RIJKERS, M.P.W.M., M. MALAIS, C.J. PETERS, & J DE SWAAN ARONS. 1992. Measurements on the phase behavior of binary hydrocarbon mixtures for modelling the condensation behavior of natural gas. *Fluid Phase Equilibria* **71**:143–168.
- SHIPMAN, L.M., & J.P. KOHN. 1966. Heterogeneous phase and volumetric equilibrium in the methane-*n*-nonane system. *J. Chem. Eng. Data* **11**(2):176–180.
- VIISANEN, Y., R. STREY, & H. REISS. 1993. Homogeneous nucleation rates for water. *J. Chem. Phys.* **99**(6):4680–4692.
- WAGNER, P.E., & R. STREY. 1984. Measurements of homogeneous nucleation rates for *n*-nonane vapor using a two-piston expansion chamber. *J. Chem. Phys.* **80**(10):5266–5275.

Chapter 7

CONCLUSIONS AND DISCUSSION

This study concerns the homogeneous nucleation and droplet growth of real mixtures *n*-nonane/methane and *n*-octane/methane at high pressures. The development of a pulse expansion tube that is able to provide experimental data on homogeneous nucleation rates at high pressures was described. A theoretical study for *n*-nonane on the basis of the Classical Nucleation Theory was carried out, and nucleation and droplet growth experiments were performed in the pulse expansion tube with various mixtures.

A nucleation pulse of about 400 μ s duration was realized in an expansion tube, which actually is a shock tube, by the implementation of a local widening in the low pressure section. The reflections of the initial shock wave at the local widening create one single nucleation pulse in the high pressure section, which is the test section. The nucleation pulse appeared to be well shaped, especially at elevated pulse pressures up to 40 bar. Droplets originate by the homogeneous nucleation process induced by the pressure and temperature increase in the high pressure section.

A light scattering method and a light extinction method provide accurate data on the droplet size and the droplet number density. The droplets are illuminated by a laser beam. Detection of the light scattered over an angle of 90° and comparison with a theoretical Mie-signal yields very accurate droplet sizes as a function of time. The light extinction method in combination with the scattering method yields droplet number density at high pressures with a relative uncertainty of 10%

Nucleation and droplet growth experiments of water in nitrogen demonstrated at low pressure an excellent performance of the expansion tube. The results of the nucleation experiments were compared with very reliable experiments of Viisanen *et al.* (1993) in a two-piston cloud chamber. Over a temperature range of 215 K – 260 K close agreement was found. Only the scatter in our experiments was a factor 3 larger. This larger scatter is possibly due to the the experimental uncertainty of the pressure measurement. The water experiments were also compared to the unary Classical Nucleation Theory and the theory of Dillmann and Meier (1991). CNT predicted values of the nucleation rate being one order of magnitude too low, at a temperature of about 210 K. At higher temperatures, above 240 K, CNT overestimated the nucleation rate by about two orders of magnitude. This in contrast to the DMT which predicted the nucleation rates correctly within the experimental uncertainty. The Dillmann–Meier theory performs very well not only for water, but also for other substances like *n*-nonane. The agreement with experimental results is much improved with respect to CNT, as has been found by many other researchers. The basis of the success of DMT is not clear yet. All the

more because Laaksonen *et al.* established an inconsistency in the theory. Removal of this inconsistency led to a deterioration of the nucleation rate predictions. However, by simplifying the model they succeeded in restoring the agreement between experiment and theory.

Droplet growth of water was compared to a droplet model of Gyarmathy (1982). Experimental droplet growth rates appeared to be 10% larger than theoretical ones over the whole range of temperatures. This is attributed to an inadequate calibration procedure of the humidity sensor used.

Measured nucleation rates of *n*-nonane in nitrogen at low pressure appeared to agree with experimental results of Wagner and Strey (1984). Again a systematic deviation was found between experimental droplet growth rates and Gyarmathy's model. Probably, vapour desorption from tube walls after the supply of nitrogen into the tube slightly increased the vapour concentration. Since the amount of *n*-nonane present in the tube was determined by measuring the vapour pressure before nitrogen was added, the *n*-nonane concentration was underestimated which explains the experimental growth rates exceeding the theoretical growth rates.

The effect of vapour desorption increases with pressure. Therefore an alternative way of determining the vapour composition on the basis of the observed droplet growth rate was described in chapter 5. The theoretical growth rate which was calculated from the high pressure limit of Gyarmathy's growth model, was fitted to the measured growth rate by varying the vapour concentration of the less volatile component in the mixture. The main uncertainty in this method is the value of the binary diffusion coefficient. An incorrect value yields a systematic error in the value for the vapour fraction of the less volatile component.

Mixtures of methane and one or more higher hydrocarbons show real gas effects that lead to retrograde phase behaviour. To study homogeneous condensation of the mixture *n*-nonane/methane mixture in the coexistence region of the mixture, the binary Classical Nucleation Theory has been adapted to account for the real gas properties of the mixture. The Redlich-Kwong-Soave equation of state was implemented in CNT to calculate the Gibbs free energy of droplet formation. An analysis with the new model shows that the amount of methane dissolved in the critical droplet increases with pressure, but remains less than the equilibrium methane concentration in the liquid. The resulting decrease of surface tension leads to an increased nucleation rate at fixed temperature and supersaturation.

Nucleation rates in *n*-nonane/methane were measured for temperatures from 230 K to 250 K and pressures from 10 bar to 40 bar. Measured nucleation rates are of the order of 10^8 to 10^{11} $\text{cm}^{-3}\text{s}^{-1}$. The supersaturations required to obtain these values of the nucleation rate decrease with pressure, e.g. at $T = 240$ K, $p = 10$ bar, $S \approx 30$; at $p = 40$ bar, $S \approx 5$. This is in qualitative agreement with the results theoretically obtained by CNT. However, quantitatively, the agreement between experiment and CNT is very poor. Also a comparison of the experiment with a semi-phenomenological model (QOC) by Kalikmanov and Van Dongen (1995) was made. At $T = 240$ K the agreement between QOC and experiment appeared to be better than that between CNT and experiment, while at $T = 250$ K the agreement was worse. A conclusion about the validity of the semi-phenomenological theory cannot be drawn yet.

When the nucleation rate was plotted versus *n*-nonane density instead of supersaturation, a totally different view is obtained. At $T = 240$ K the experimental curves at different pressures are situated inside a very small interval of *n*-nonane vapour density. This may be an indication that two opposing effects play a role.

Experiments on the *n*-octane/methane mixture show similar results as sketched for *n*-nonane/methane.

We end up with the important conclusion that real gas properties present in the coexistence region of hydrocarbon mixtures at high pressures strongly effect the nucleation rate as a function of supersaturation. The picture is less clear when the *n*-nonane vapour density is considered. Experiments on other mixtures and at different circumstances should reveal whether this behaviour either is typical for *n*-nonane and *n*-octane, or is a result of the peculiarity of the real gas behaviour considered in this work.

References

- DILLMANN, A., & G.E.A. MEIER. 1991. A refined droplet approach to the problem of homogeneous nucleation from the vapor phase. *J. Chem. Phys.* **94**(5):3872–3884.
- GYARMATHY, G. 1982. The spherical droplet in gaseous carrier streams: review and synthesis. In *Multiphase science and technology, 1*. Washington: Hemisphere Publishing Corporation.
- KALIKMANOV, V.I., & M.E.H. VAN DONGEN. 1995. Quasi-one-component theory of homogeneous binary nucleation. *Phys. Rev. E* **51**:in press.
- VIISANEN, Y., R. STREY, & H. REISS. 1993. Homogeneous nucleation rates for water. *J. Chem. Phys.* **99**(6):4680–4692.
- WAGNER, P.E., & R. STREY. 1984. Measurements of homogeneous nucleation rates for *n*-nonane vapor using a two-piston expansion chamber. *J. Chem. Phys.* **80**(10):5266–5275.

Appendix A

PHYSICAL PROPERTIES

Material properties of gases and liquids: critical density ρ_c , critical pressure p_c , critical temperature T_c , Pitzer's acentric factor ω , Rackett compressibility factor Z_{RA} , molar mass M , parachor P , refractive index m , liquid density ρ^l , surface tension σ , saturation vapour pressure p_{eq} , second virial coefficient B . For temperature dependent properties the absolute temperature T in K must be inserted:

| water: | unit | literature |
|--|--|------------|
| $\rho_c = 323$ | kg m ⁻³ | (e) |
| $T_c = 647.3$ | K | (a) |
| $M = 18.015$ | kg kmol ⁻¹ | (a) |
| $m = 1.334$ | – | (c) |
| $\rho^l = 999.84 + 0.086(T - 273.15) - 0.0108(T - 273.15)^2$ | kg m ⁻³ | (d) |
| $\sigma = 0.111773(1 - T/T_c)^{0.712012}$ | N m ⁻¹ | (c) |
| $p_{eq} = 610.8 \exp(-5.1421 \ln(T/273.15) - 6828.77(1/T - 1/273.15))$ | N m ⁻² | (f) |
| $B = 17.1 - 102.9(T_c/T)^2 - 33.6 \times 10^{-3} T/T_c \exp(5.255T_c/T)$ | cm ³ mol ⁻¹ | (e) |
| methane: | | |
| $p_c = 46.0$ | bar | (a) |
| $T_c = 190.4$ | K | (a) |
| $\rho_c = 163.5$ | kg m ⁻³ | (i) |
| $\omega = 0.011$ | – | (a) |
| $Z_{RA} = 0.2892$ | – | (a) |
| $M = 16.043$ | kg kmol ⁻¹ | (a) |
| $P = 81.0$ | g ^{1/4} cm ³ s ^{-1/2} mol ⁻¹ | (a) |
| <i>n</i> -nonane: | | |
| $p_c = 22.9$ | bar | (a) |
| $T_c = 594.6$ | K | (a) |
| $\rho_c = 234$ | kg m ⁻³ | (e) |
| $\omega = 0.445$ | – | (a) |

| | unit | literature |
|---|--|------------|
| $Z_{RA} = 0.2543$ | – | (a) |
| $M = 128.259$ | kg kmol ⁻¹ | (a) |
| $P = 81.0$ | g ^{1/4} cm ³ s ^{-1/2} mol ⁻¹ | (a) |
| $m = 1.405$ | – | (c) |
| $\rho^l = 733.3 - 0.75(T - 273.15) +$ $4.55 \times 10^{-4}(T - 273.15)^2$ | kg m ⁻³ | (g) |
| $\sigma = (24.72 - 0.09347(T - 273.15))/1000$ | N m ⁻¹ | (g) |
| $p_{eq} = 1000 \exp(-1647.6676 + 27512.569/T -$ $0.96917185T + 4.7629229 \times 10^{-4}T^2 +$ $316.16334 \ln(T))$ | N m ⁻² | (h) |
| $B = 369.2 - 705.3T_c/T + 17.9(T_c/T)^2 -$ $427(T_c/T)^3 - 8.9(T_c/T)^8$ | cm ³ mol ⁻¹ | (g) |
| <i>n</i> -octane: | | |
| $p_c = 24.9$ | bar | (a) |
| $T_c = 568.8$ | K | (a) |
| $\omega = 0.398$ | – | (a) |
| $Z_{RA} = 0.2571$ | – | (a) |
| $M = 114.232$ | g mol ⁻¹ | (a) |
| $P = 350.6$ | g ^{1/4} cm ³ s ^{-1/2} mol ⁻¹ | (a) |
| $m = 1.395$ | – | (c) |

Binary interaction parameters k_{ij} used in the RKS equation of state:

| | | | |
|--------------------------|-------------------|---|-----|
| <i>n</i> -nonane/methane | $k_{ij} = 0.0448$ | – | (b) |
| <i>n</i> -octane/methane | $k_{ij} = 0.0448$ | – | (b) |

Diffusion coefficients of *n*-nonane/methane and *n*-octane/methane are calculated according to the method proposed by Fuller *et al.* (1987), together with the Takahashi correlation \mathcal{T} (1987) for the effect of pressure on the diffusion coefficient. Temperatures are inserted in K, pressure in bar:

$$D_{12} = \frac{0.00143T^{1.75}}{pM_{12}^{1/2} \left[(\Sigma v_1^{1/3}) + (\Sigma v_2^{1/3}) \right]^2} \cdot \mathcal{T}(T_r, P_r) \quad \text{cm}^2 \text{ s}^{-1} \quad (\text{a})$$

$$\mathcal{T}(T_r, p_r) = 1 + p_r \left(\frac{1}{3}T_r - 0.583 \right)$$

$$M_{12} = 2 \left[(1/M_1) + (1/M_2) \right]^{-1}$$

$$T_r = \frac{T}{T_c}$$

$$T_c = y_1 T_{c,1} + y_2 T_{c,2}$$

$$p_r = \frac{p}{p_c}$$

$$p_c = y_1 p_{c,1} + y_2 p_{c,2}$$

| | |
|-------------------------------|-----|
| methane: $\Sigma_v = 25.4$ | (a) |
| n-octane: $\Sigma_v = 168.78$ | (a) |
| n-nonane: $\Sigma_v = 189.3$ | (a) |

To calculate the temperature during the expansion the isentropic exponent γ is used for nitrogen. For methane the compressibility factor Z , and the isobaric heat capacity c_p are calculated according the equation of state given by Sychev *et al.* (1987):

nitrogen:
 $\gamma = 1.40$

methane:

$$Z = 1 + A_0$$

$$\frac{c_p}{R} = \frac{c_{p,0}}{R} - 1 + A_5 + (1 + A_2)^2 / (1 + A_1)$$

$$A_0 = \sum_{i=1}^{10} \sum_{j=0}^7 b_{ij} \frac{\rho_r^i}{T_r^j}$$

$$A_1 = \sum_{i=1}^{10} \sum_{j=1}^7 (i + 1) b_{ij} \frac{\rho_r^i}{T_r^j}$$

$$A_2 = - \sum_{i=1}^{10} \sum_{j=0}^7 (j - 1) b_{ij} \frac{\rho_r^i}{T_r^j}$$

$$A_5 = - \sum_{i=1}^{10} \sum_{j=0}^7 \frac{j(j-1)}{i} b_{ij} \frac{\rho_r^i}{T_r^j}$$

$$\frac{c_{p,0}}{R} = \sum_{j=0}^{10} \alpha_j \phi^j + \sum_{j=1}^6 \beta_j \phi^{-j}$$

$$\phi = \frac{T}{100 \text{ K}}$$

$$\rho_r = \frac{\rho}{\rho_c}$$

$$T_r = \frac{T}{T_c}$$

coefficients:

| | | |
|-------------------------------------|--------------------------------------|--------------------------------------|
| $b_{10} = 0.5365574$ | $b_{34} = -0.1690813 \times 10^1$ | $b_{63} = -0.1025381$ |
| $b_{11} = -0.1671289 \times 10^1$ | $b_{35} = 0.1154217 \times 10^1$ | $b_{64} = 0.7468426 \times 10^{-1}$ |
| $b_{12} = 0.1704335 \times 10^1$ | $b_{36} = 0.9352795 \times 10^{-1}$ | |
| $b_{13} = -0.4003982 \times 10^1$ | | $b_{70} = -0.8863694 \times 10^{-1}$ |
| $b_{14} = 0.3491415 \times 10^1$ | $b_{40} = 0.2431204 \times 10^{-1}$ | $b_{71} = -0.6837762 \times 10^{-1}$ |
| $b_{15} = -0.1332024 \times 10^1$ | $b_{41} = 0.3478417$ | $b_{72} = 0.5915308 \times 10^{-1}$ |
| $b_{16} = 0.5440249 \times 10^{-1}$ | $b_{42} = 0.3587548 \times 10^{-1}$ | $b_{73} = 0.2985520 \times 10^{-2}$ |
| $b_{17} = 0.5211075 \times 10^{-1}$ | $b_{43} = 0.2945131$ | |
| | $b_{44} = 0.1565847 \times 10^{-1}$ | $b_{80} = 0.3030236 \times 10^{-1}$ |
| $b_{20} = 0.7187518 \times 10^{-1}$ | $b_{45} = -0.4257759$ | $b_{81} = -0.1014545 \times 10^{-2}$ |
| $b_{21} = 0.5481658$ | | $b_{82} = -0.1847890 \times 10^{-1}$ |
| $b_{22} = -0.1932578 \times 10^1$ | $b_{50} = -0.1779964$ | $b_{83} = -0.3250667 \times 10^{-2}$ |
| $b_{23} = 0.4295984 \times 10^1$ | $b_{51} = -0.2754465 \times 10^{-1}$ | |
| $b_{24} = -0.3969273 \times 10^1$ | $b_{52} = -0.5843797$ | $b_{90} = -0.6183691 \times 10^{-2}$ |
| $b_{25} = 0.1944849 \times 10^1$ | $b_{53} = 0.2273617$ | $b_{91} = 0.6643026 \times 10^{-2}$ |
| $b_{26} = -0.5923964$ | $b_{54} = -0.7393567 \times 10^{-1}$ | $b_{92} = 0.9014904 \times 10^{-3}$ |

$$\begin{array}{lll}
 b_{30} = 0.4802716 \times 10^{-1} & b_{55} = 0.1461452 \times 10^{-1} & b_{93} = -0.8454372 \times 10^{-3} \\
 b_{31} = 0.1443345 & b_{60} = 0.1650834 & b_{10\ 0} = 0.6100390 \times 10^{-3} \\
 b_{32} = -0.1249822 \times 10^1 & b_{61} = 0.1337959 & b_{10\ 1} = -0.1371245 \times 10^{-2} \\
 b_{33} = 0.1618220 \times 10^1 & b_{62} = 0.1158357 & b_{10\ 2} = 0.6833971 \times 10^{-3}
 \end{array}$$

$$\begin{array}{ll}
 \alpha_0 = 0.146696186 \times 10^3 & \beta_1 = -0.209233731 \times 10^3 \\
 \alpha_1 = -0.656744186 \times 10^2 & \beta_2 = 0.206925203 \times 10^3 \\
 \alpha_2 = 0.202698132 \times 10^2 & \beta_3 = -0.135704831 \times 10^3 \\
 \alpha_3 = -0.420931845 \times 10^1 & \beta_4 = 0.564368924 \times 10^2 \\
 \alpha_4 = 0.606743008 & \beta_5 = -0.134496111 \times 10^2 \\
 \alpha_5 = -0.612623969 \times 10^{-1} & \beta_6 = 0.139664152 \times 10^1 \\
 \alpha_6 = 0.430969226 \times 10^{-2} & \\
 \alpha_7 = -0.206597572 \times 10^{-3} & \\
 \alpha_8 = 0.642615810 \times 10^{-5} & \\
 \alpha_9 = -0.116805630 \times 10^{-6} & \\
 \alpha_{10} = 0.940958930 \times 10^{-9} &
 \end{array}$$

Literature:

- (a) Reid *et al.* (1987)
- (b) Knapp *et al.* (1982)
- (c) Landolt-Börnstein (1960, 1962)
- (d) Pruppacher and Klett (1978)
- (e) Dillmann and Meier (1991)
- (f) Vargaftik (1975)
- (g) Adams *et al.* (1984)
- (h) Boublik *et al.* (1984)
- (i) Sychev *et al.* (1987)

References

- ADAMS, G.W., J.L. SCHMITT, & R.A. ZALABSKY. 1984. The homogeneous nucleation of nonane. *J. Chem. Phys.* 81(11):5074-5078.
- BOUBLIK, T., V. FRIED, & E. HALA. 1984. *Physical sciences data 17: The vapour pressures of pure substances*. Amsterdam, The Netherlands: Elsevier.
- DILLMANN, A., & G.E.A. MEIER. 1991. A refined droplet approach to the problem of homogeneous nucleation from the vapor phase. *J. Chem. Phys.* 94(5):3872-3884.
- KNAPP, H., R. DÖRING, L. OELLRICH, U. PLÖCKER, & J.M. PRAUSNITZ. 1982. *Vapor-Liquid Equilibria for Mixtures of Low Boiling Substances*. Frankfurt am Main: Deutsche Gesellschaft für Chemisches Apparatewesen.

- LANDOLT-BÖRNSTEIN. 1960. *Zahlenwerte und Funktionen*. Vol. II Band, 2a. Teil. Berlin: Springer Verlag.
- LANDOLT-BÖRNSTEIN. 1962. *Zahlenwert und Funktionen*. Vol. II Band, 8. Teil. Berlin: Springer Verlag.
- PRUPPACHER, H.R., & J.D. KLETT. 1978. *Microphysics of clouds and precipitation*. Dordrecht, Holland: Reidel.
- REID, R.C., J.M. PRAUSNITZ, & B.E. POLING. 1987. *The Properties of Gases and Liquids*. New York: McGraw-Hill Book Company.
- SYCHEV, V.V., A.A. VASSERMAN, V.A. ZAGORUCHENKO, A.D. KOZLOV, G.A. SPIRIDONOV, & V.A. TSYMARNY. 1987. *Thermodynamic properties of methane*. Washington: Hemisphere publishing corporation.
- VARGAFTIK, N.B. 1975. *Tables on the thermophysical properties of liquids and gases 2nd edition*. New York: Wiley.

Appendix B

RANDOM CHOICE METHOD

Introduction

This appendix outlines the Random Choice numerical Method as it is used to calculate the pressure history of the pulse expansion tube in section 4.3.3.

The Random Choice Method (RCM) is a numerical technique capable to solve quasi-one-dimensional hyperbolic partial differential equations. The gasdynamic wave propagation in a shock tube is governed by the hyperbolic 1D wave equation. The RCM was first described by Chorin (1976) in a way feasible for computational use. Since then, the efficiency of the RCM in terms of computer time has gradually been improved. A good review of the method is given by Toro (1987).

The RCM is a time explicit method; the solution at a time level t_n , $U(t_n, x)$, is calculated by solving a sequence of Riemann problems at the foregoing time level t_{n-1} . Toro (1987) mentions four virtues that make RCM particularly suitable to gasdynamic problems:

- Discontinuities like shocks and contacts are captured with infinite resolution.
- Wave interactions are handled automatically.
- *Ad hoc* procedures and adjustable arbitrary parameters are absent.
- The method has good physical and mathematical foundations.

The main concept of RCM will be described below.

Concept of the Random Choice Method

Our goal is to describe the time development of the distribution of the flow parameters pressure p , density ρ , and velocity u in a quasi-1D tube configuration. Our treatment of the RCM on a non-staggered grid is analogous to the approach described by Toro (1987).

We start with a known solution $U(t_n, x)$ at time t_n . The first step concerns the discretization of the initial data $U(t_n, x)$ with respect to the spatial coordinate x . This is illustrated in fig. B.1. One of the parameters of the problem (for example pressure or density) at time t_n is plotted versus the spatial coordinate x . The data are approximated as a piecewise constant function of x . At the interval $[i - \frac{1}{2}\Delta x, i + \frac{1}{2}\Delta x]$ the function value equals the value of the computational node i . The transition discontinuity is positioned in the middle between two successive computational nodes. We now consider the computational cell from node i to node

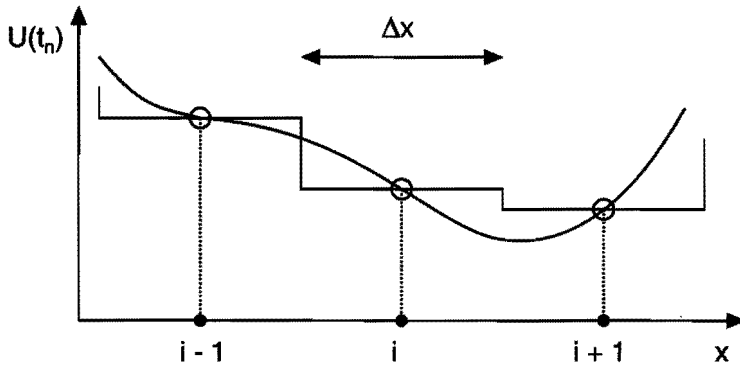


Figure B.1: Approximation of data at time t_n in the spatial domain by a piecewise constant function.

$i + 1$. In our approximation, the variables are assumed to be constant left and right from the discontinuity in the middle of the cell, so that the time development of the cell variables is described by the solution of a Riemann problem. This way the whole spatial domain forms a sequence of Riemann problems, that can be solved independently by the procedure described in section 4.2.

Figure B.2 schematically shows the solution of the Riemann problem in two adjacent cells. In each cell a left running wave, a right running wave, and a contact discontinuity develop.

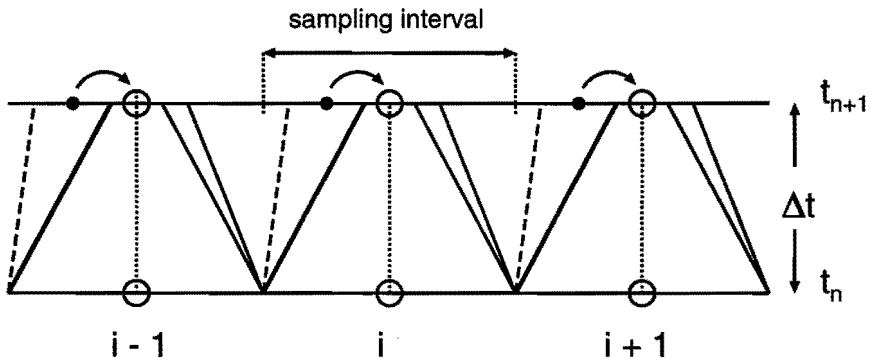


Figure B.2: Two adjacent computational cells with schematic representation of the solution of the Riemann problem. At time t_{n+1} the sampling procedure is illustrated. The solution of the Riemann problem at the sampling position x_{pi} , $U(t_{n+1}, x_{pi})$, is assigned to the nearest computational node.

Either wave can be a shock or expansion wave, allowing four possible combinations. The solutions of the Riemann problems are calculated by means of an exact Riemann solver using Newton–Raphson iteration. The solution of the Riemann problem at time level t_{n+1} is multi-valued, therefore a (quasi-) random sampling method is applied to assign a solution to the grid points at t_{n+1} (fig B.2). On the sampling interval $[i - \frac{1}{2}\Delta x, i + \frac{1}{2}\Delta x]$ one solution of the

Riemann problems concerned is selected randomly. This solution is allocated to the nearest computational node i . The van der Corput sequence is applied for the random number generation (Collela 1982). It selects an alternating sampling position left and right from the node i .

By repeating the procedure described above, the solution is advanced from t_{n+1} to the next time level t_{n+2} , etc. After a large number of time steps, the averaging property of the random selection of solutions of the Riemann problems will result in a correct description of the wave propagation in the $x - t$ domain.

To obtain a maximum "computational speed" the time step ΔT was chosen as large as possible. The length of ΔT is limited by the Courant–Friedrichs–Lewy condition (CFL condition). In the context of RCM, the CFL condition states that no interaction of waves of neighbouring Riemann problems is allowed before the sampling procedure was carried out. So, the time step is chosen to satisfy: $\Delta T = (1/2\Delta x)/S_{max}$, where S_{max} is the maximum wave speed at a given time level.

References

- CHORIN, A.J. 1976. Random choice solution of hyperbolic systems. *J. Comput. Phys.* **22**:517–533.
- COLLELA, P. 1982. Glimm's method for gas dynamics. *Siam J. Sci Stat. Comput.* **3**(1):76–110.
- TORO, E.F. 1987. *The Random Choice Method on a non-staggered grid utilising an efficient Riemann solver*. Cranfield College of Aeronautics, report no. 8708.

Appendix C

UNARY NUCLEATION

In chapter 6 experimental homogeneous nucleation rates for water in nitrogen, and *n*-nonane in nitrogen are compared to unary Classical Nucleation Theory, and the Dillmann Meier Theory of unary nucleation. The expressions used in the calculations are listed below.

The expression for CNT reads:

$$J_{CNT} = \sqrt{\frac{2\sigma m}{\pi}} \frac{(p^v)^2}{k_B^2 T^2 \rho^l} \exp\left(-\frac{4\pi\sigma(r^*)^2}{3k_B T}\right). \quad (C.1)$$

The radius of the critical nucleus r^* is given by:

$$r^* = \frac{2\sigma}{\rho^l T R_m \ln S}, \quad (C.2)$$

with the specific gas constant R_m , and the supersaturation defined by $S = p^v/p_{eq}^v$.

The nucleation rate according to DMT is described by the following set of equations:

$$J_{DMT} = \frac{1}{3} \sqrt{\frac{\sigma A_1}{k_B T \pi}} \left(1 + \alpha_1 (i^*)^{-1/3} + \frac{9\tau k_B T}{2\sigma A_1} (i^*)^{-2/3}\right) \times \frac{A_1 p^v}{\sqrt{2\pi m k_B T}} \exp\left(\frac{-\Delta F(i^*)}{k_B T}\right), \quad (C.3)$$

$$\Delta F(i^*) = -k_B T i^* \ln S + \left(1 + \alpha_1 (i^*)^{-1/3} + \alpha_2 (i^*)^{-2/3}\right) \sigma A_1 (i^*)^{2/3} + k_B T \tau \ln i^* - k_B T \ln(q_0 V^*), \quad (C.4)$$

$$A_1 = (6\sqrt{\pi} v^l)^{2/3}, \quad (C.5)$$

$$V^* = i^* v^l, \quad (C.6)$$

$$\alpha_1 = \frac{(\kappa(2) - 1) - (\kappa(1) - 1)2^{-2/3}}{2^{-1/3} - 2^{-2/3}}, \quad (C.7)$$

$$\alpha_2 = -\frac{(\kappa(2) - 1) - (\kappa(1) - 1)2^{-1/3}}{2^{-1/3} - 2^{-2/3}}, \quad (C.8)$$

$$\kappa(1) = -\frac{k_B T}{\sigma A_1} \ln\left(\frac{p_{eq}^v}{q_0 k_B T}\right), \quad (C.9)$$

$$\kappa(2) = -\frac{k_B T}{\sigma A_1 2^{2/3}} \ln\left[-\left(\frac{p_{eq}^v}{q_0 k_B T}\right)^2 2^{\tau-1} q_0 B\right]. \quad (C.10)$$

In these equations v^l is the molecular volume of the liquid, and B the second virial coefficient. The parameters τ and q_0 are related to the critical point properties; the values are listed in table C.1. The number of molecules in the critical cluster i^* is determined by the solution of

| | τ | q_0 |
|------------------|--------|-------|
| water | 2.166 | 48.84 |
| <i>n</i> -nonane | 2.190 | 39.97 |

Table C.1: Parameters DMT.

the cubic equation:

$$\tau \left(\sqrt[3]{i^*}\right)^3 + \frac{1}{3}\alpha_1 \frac{\sigma A_1}{k_B T} \left(\sqrt[3]{i^*}\right)^2 + \frac{2\sigma A_1}{k_B T} \left(\sqrt[3]{i^*}\right) - \ln S = 0 \quad (\text{C.11})$$

Appendix D

TABLES OF EXPERIMENTAL DATA

This appendix contains a list of the experimental data concerning the nucleation experiments of water/nitrogen and *n*-nonane/nitrogen at low pressure, and *n*-nonane/methane and *n*-octane/methane at high pressures.

| n° | p^* (bar) | p_1^* (Pa) | T^* (K) | J ($\text{cm}^{-3}\text{s}^{-1}$) |
|-----------|-------------|--------------------|-----------|---------------------------------------|
| 402 | 0.413 | 51 | 212.6 | 1.9×10^9 |
| 403 | 0.404 | 50 | 209.7 | 6.9×10^{10} |
| 404 | 0.572 | 273 | 234.6 | 9.0×10^7 |
| 405 | 0.550 | 269 | 233.2 | 3.4×10^8 |
| 407 | 0.807 | 961 | 249.4 | 1.2×10^{10} |
| 408 | 0.838 | 1.01×10^3 | 251.7 | 1.2×10^8 |
| 409 | 0.920 | 1.17×10^3 | 252.9 | 7.1×10^9 |
| 411 | 0.621 | 515 | 240.9 | 1.7×10^9 |
| 412 | 0.713 | 475 | 239.7 | 3.7×10^9 |
| 413 | 0.719 | 476 | 240.0 | 1.0×10^9 |
| 414 | 0.771 | 585 | 244.5 | 1.0×10^8 |
| 415 | 0.741 | 568 | 242.4 | 7.3×10^8 |
| 417 | 0.628 | 353 | 236.5 | 2.4×10^8 |
| 418 | 0.574 | 223 | 230.1 | 5.3×10^8 |
| 419 | 0.468 | 116 | 222.5 | 2.8×10^8 |
| 421 | 0.464 | 110 | 220.7 | 1.7×10^9 |
| 422 | 0.429 | 70 | 214.7 | 6.6×10^9 |
| 423 | 0.375 | 34 | 208.0 | 8.7×10^8 |
| 424 | 0.368 | 34 | 206.8 | 2.3×10^9 |
| 425 | 0.358 | 34 | 206.3 | 3.8×10^9 |
| 427 | 0.326 | 19 | 198.9 | 9.1×10^9 |
| 428 | 0.309 | 19 | 197.6 | 4.4×10^{10} |

Table D.1: Experimental nucleation data of water/nitrogen at low pressure. The data are represented in Fig. 6.3.

| n° | p^* (bar) | p_1^* (Pa) | T^* (K) | J ($\text{cm}^{-3}\text{s}^{-1}$) |
|-----------|-------------|--------------|-----------|---------------------------------------|
| 433 | 0.350 | 66 | 212.0 | 1×10^{10} |
| 434 | 0.370 | 76 | 216.4 | 8×10^7 |
| 435 | 0.360 | 63 | 214.9 | 7×10^7 |
| 437 | 0.358 | 69 | 213.5 | 9×10^8 |
| 438 | 0.367 | 80 | 214.5 | 8×10^8 |
| 439 | 0.374 | 79 | 215.5 | 3×10^7 |
| 440 | 0.364 | 65 | 213.7 | 5×10^8 |
| 443 | 0.363 | 75 | 214.3 | 5×10^8 |
| 462 | 0.365 | 90 | 220.2 | 3×10^8 |
| 464 | 0.387 | 88 | 223.1 | 4×10^8 |
| 465 | 0.386 | 87 | 223.9 | 2×10^8 |
| 470 | 0.404 | 119 | 225.7 | 3×10^9 |
| 471 | 0.361 | 82 | 218.3 | 3×10^{10} |
| 472 | 0.360 | 81 | 218.7 | 1×10^{10} |
| 473 | 0.386 | 89 | 222.1 | 3×10^8 |
| 474 | 0.336 | 56 | 213.7 | 1×10^{10} |
| 475 | 0.362 | 62 | 217.8 | 2×10^8 |
| 477 | 0.303 | 34 | 207.5 | 2×10^9 |
| 478 | 0.316 | 34 | 210.3 | 3×10^8 |
| 481 | 0.266 | 14 | 201.0 | 3×10^9 |
| 482 | 0.264 | 17 | 200.0 | 8×10^9 |
| 483 | 0.271 | 17 | 202.0 | 3×10^9 |
| 484 | 0.407 | 117 | 226.2 | 2×10^8 |
| 486 | 0.404 | 119 | 226.6 | 2×10^8 |
| 491 | 0.365 | 88 | 222.8 | 3×10^9 |

Table D.2: Experimental nucleation data of *n*-nonane/nitrogen at low pressure. The data are represented in Fig. 6.9.

| n° | p^* (bar) | T^* | y_1^* | J ($\text{cm}^{-3}\text{s}^{-1}$) |
|-----------|-------------|-------|-----------------------|---------------------------------------|
| 727 | 19.6 | 239.3 | 1.48×10^{-4} | 7.8×10^8 |
| 728 | 19.6 | 238.4 | 1.44×10^{-4} | 1.6×10^9 |
| 729 | 19.9 | 239.7 | 1.48×10^{-4} | 5.0×10^8 |
| 730 | 19.6 | 239.2 | 1.59×10^{-4} | 3.6×10^9 |
| 731 | 19.6 | 239.4 | 1.63×10^{-4} | 1.2×10^{10} |
| 732 | 20.1 | 242.9 | 1.96×10^{-4} | 4.3×10^9 |
| 735 | 19.8 | 240.5 | 1.79×10^{-4} | 7.0×10^{10} |
| 740 | 20.2 | 241.1 | 1.79×10^{-4} | 2.0×10^{10} |
| 741 | 19.6 | 239.4 | 1.72×10^{-4} | 4.6×10^{10} |
| 742 | 19.6 | 239.1 | 1.35×10^{-4} | 5.9×10^8 |

Table D.3: Experimental nucleation data of *n*-nonane/methane at 20 bar, 240 K. The data are represented in Fig. 6.13.

| n° | p^* (bar) | T^* | y_1^* | J ($\text{cm}^{-3}\text{s}^{-1}$) |
|-----------|-------------|-------|-----------------------|---------------------------------------|
| 750 | 41.1 | 243.9 | 1.14×10^{-4} | 3.4×10^{10} |
| 751 | 39.6 | 241.2 | 8.7×10^{-5} | 1.1×10^{11} |
| 752 | 39.8 | 240.9 | 6.9×10^{-5} | 1.0×10^{10} |
| 753 | 39.8 | 240.4 | 4.43×10^{-5} | 1.8×10^{10} |
| 754 | 39.8 | 240.0 | 4.30×10^{-5} | 1.3×10^{10} |
| 755 | 41.7 | 243.3 | 6.6×10^{-5} | 7.9×10^9 |
| 821 | 39.8 | 239.9 | 4.54×10^{-5} | 8.3×10^8 |
| 822 | 39.9 | 241.6 | 6.02×10^{-5} | 5.1×10^8 |

Table D.4: Experimental nucleation data of *n*-nonane/methane at 40 bar, 240 K. The data are represented in Fig. 6.13.

| n° | p^* (bar) | T^* | y_1^* | J ($\text{cm}^{-3}\text{s}^{-1}$) |
|-----------|-------------|-------|-----------------------|---------------------------------------|
| 800 | 29.4 | 238.3 | 8.48×10^{-5} | 1.0×10^9 |
| 801 | 30.4 | 240.6 | 1.14×10^{-4} | 5.3×10^9 |
| 802 | 30.2 | 239.5 | 1.08×10^{-4} | 2.5×10^{10} |
| 803 | 30.0 | 239.1 | 1.08×10^{-4} | 4.0×10^{10} |
| 804 | 31.3 | 242.2 | 1.22×10^{-4} | 1.4×10^{10} |
| 805 | 30.8 | 240.9 | 1.21×10^{-4} | 3.2×10^{10} |
| 806 | 30.6 | 241.4 | 1.30×10^{-4} | 1.4×10^{11} |
| 808 | 31.6 | 242.8 | 1.13×10^{-4} | 1.0×10^9 |
| 809 | 29.9 | 238.2 | 1.07×10^{-4} | 9.1×10^{10} |
| 810 | 30.1 | 239.0 | 8.64×10^{-5} | 8.3×10^8 |
| 811 | 29.2 | 238.4 | 9.87×10^{-5} | 1.0×10^{10} |

Table D.5: Experimental nucleation data of *n*-nonane/methane at 30 bar, 240 K. The data are represented in Fig. 6.13.

| n° | p^* (bar) | T^* | y_1^* | J ($\text{cm}^{-3}\text{s}^{-1}$) |
|-----------|-------------|-------|-----------------------|---------------------------------------|
| 812 | 10.2 | 238.3 | 2.28×10^{-4} | 1.4×10^8 |
| 814 | 10.2 | 241.4 | 2.93×10^{-4} | 6.0×10^8 |
| 815 | 10.3 | 241.2 | 2.80×10^{-4} | 3.9×10^8 |
| 816 | 10.0 | 239.6 | 2.71×10^{-4} | 2.2×10^9 |
| 817 | 9.9 | 238.7 | 2.87×10^{-4} | 1.5×10^{10} |
| 818 | 10.1 | 240.3 | 3.01×10^{-4} | 9.0×10^9 |
| 819 | 10.0 | 239.5 | 3.05×10^{-4} | 1.8×10^{10} |
| 820 | 10.1 | 239.2 | 2.54×10^{-4} | 4.5×10^8 |

Table D.6: Experimental nucleation data of *n*-nonane/methane at 10 bar, 240 K. The data are represented in Fig. 6.13.

| n° | p^* (bar) | T^* | y_1^* | J ($\text{cm}^{-3}\text{s}^{-1}$) |
|-----|-------------|-------|-----------------------|---------------------------------------|
| 831 | 19.9 | 229.7 | 6.47×10^{-5} | 4.2×10^9 |
| 832 | 20.2 | 230.8 | 7.91×10^{-5} | 1.6×10^{10} |
| 833 | 20.0 | 230.0 | 7.46×10^{-5} | 2.1×10^{11} |
| 834 | 20.6 | 233.6 | 8.95×10^{-5} | 1.5×10^9 |
| 835 | 20.1 | 231.6 | 8.60×10^{-5} | 2.0×10^{10} |
| 837 | 19.9 | 230.0 | 7.74×10^{-5} | 4.5×10^{10} |

Table D.7: Experimental nucleation data of *n*-nonane/methane at 20 bar, 230 K. The data are represented in Fig. 6.16.

| n° | p^* (bar) | T^* | y_1^* | J ($\text{cm}^{-3}\text{s}^{-1}$) |
|-----|-------------|-------|-----------------------|---------------------------------------|
| 838 | 9.7 | 227.3 | 1.24×10^{-4} | 3.0×10^{10} |
| 839 | 9.9 | 230.2 | 1.47×10^{-4} | 1.6×10^9 |
| 840 | 10.0 | 230.5 | 1.47×10^{-4} | 3.5×10^9 |
| 841 | 10.1 | 230.9 | 1.55×10^{-4} | 6.5×10^9 |
| 842 | 10.0 | 229.3 | 1.57×10^{-4} | 7.4×10^{10} |
| 843 | 10.1 | 230.2 | 1.53×10^{-4} | 2.0×10^{10} |
| 844 | 10.0 | 229.5 | 1.31×10^{-4} | 3.1×10^9 |
| 845 | 10.0 | 229.3 | 1.22×10^{-4} | 7.3×10^8 |

Table D.8: Experimental nucleation data of *n*-nonane/methane at 10 bar, 230 K. The data are represented in Fig. 6.16.

| n° | p^* (bar) | T^* | y_1^* | J ($\text{cm}^{-3}\text{s}^{-1}$) |
|-----|-------------|-------|-----------------------|---------------------------------------|
| 854 | 30.0 | 229.7 | 2.56×10^{-5} | 1.2×10^{11} |
| 855 | 30.3 | 230.3 | 2.16×10^{-5} | 6.7×10^{10} |
| 856 | 29.9 | 230.1 | 2.73×10^{-5} | 3.9×10^{10} |
| 857 | 30.4 | 231.0 | 2.23×10^{-5} | 2.6×10^{10} |

Table D.9: Experimental nucleation data of *n*-nonane/methane at 30 bar, 230 K. The data are represented in Fig. 6.16.

| n° | p^* (bar) | T^* | y_1^* | J ($\text{cm}^{-3}\text{s}^{-1}$) |
|-----|-------------|-------|-----------------------|---------------------------------------|
| 824 | 30.4 | 250.0 | 2.42×10^{-4} | 2.0×10^8 |
| 825 | 30.4 | 250.8 | 2.82×10^{-4} | 1.1×10^{10} |
| 826 | 30.0 | 249.3 | 2.63×10^{-4} | 4.2×10^9 |
| 827 | 30.0 | 250.5 | 2.55×10^{-4} | 2.2×10^8 |

Table D.10: Experimental nucleation data of *n*-nonane/methane at 30 bar, 250 K. The data are represented in Fig. 6.17.

| n° | p^* (bar) | T^* | y_1^* | J ($\text{cm}^{-3}\text{s}^{-1}$) |
|-----------|-------------|-------|-----------------------|---------------------------------------|
| 846 | 40.3 | 251.2 | 2.17×10^{-4} | 1.4×10^8 |
| 847 | 40.1 | 250.6 | 2.38×10^{-4} | 4.9×10^9 |
| 848 | 40.0 | 250.5 | 2.33×10^{-4} | 1.4×10^{10} |
| 849 | 39.9 | 249.6 | 2.25×10^{-4} | 6.4×10^9 |
| 850 | 40.0 | 250.2 | 2.34×10^{-4} | 6.1×10^{10} |

Table D.11: Experimental nucleation data of *n*-nonane/methane at 40 bar, 250 K. The data are represented in Fig. 6.17.

| n° | p^* (bar) | T^* | y_1^* | J ($\text{cm}^{-3}\text{s}^{-1}$) |
|-----------|-------------|-------|-----------------------|---------------------------------------|
| 961 | 10.0 | 236.7 | 7.31×10^{-4} | 1.2×10^{10} |
| 962 | 10.2 | 240.9 | 8.43×10^{-4} | 6.7×10^8 |
| 963 | 9.9 | 240.1 | 8.86×10^{-4} | 6.0×10^8 |
| 968 | 10.0 | 239.6 | 8.89×10^{-4} | 5.8×10^9 |

Table D.12: Experimental nucleation data of *n*-octane/methane at 10 bar, 240 K. The data are represented in Fig. 6.20.

| n° | p^* (bar) | T^* | y_1^* | J ($\text{cm}^{-3}\text{s}^{-1}$) |
|-----------|-------------|-------|-----------------------|---------------------------------------|
| 951 | 20.3 | 240.9 | 4.52×10^{-4} | 4.0×10^8 |
| 952 | 20.2 | 239.6 | 4.56×10^{-4} | 2.0×10^{10} |
| 953 | 20.2 | 240.3 | 4.87×10^{-4} | 9.6×10^9 |
| 966 | 20.2 | 239.8 | 4.64×10^{-4} | 4.2×10^9 |

Table D.13: Experimental nucleation data of *n*-octane/methane at 20 bar, 240 K. The data are represented in Fig. 6.20.

| n° | p^* (bar) | T^* | y_1^* | J ($\text{cm}^{-3}\text{s}^{-1}$) |
|-----------|-------------|-------|-----------------------|---------------------------------------|
| 958 | 29.9 | 238.6 | 2.81×10^{-4} | 2.3×10^{10} |
| 959 | 30.1 | 240.5 | 2.94×10^{-4} | 5.5×10^8 |
| 960 | 30.1 | 240.1 | 3.04×10^{-4} | 3.8×10^9 |
| 965 | 30.0 | 239.7 | 3.01×10^{-4} | 6.1×10^9 |

Table D.14: Experimental nucleation data of *n*-octane/methane at 30 bar, 240 K. The data are represented in Fig. 6.20.

| n° | p^* (bar) | T^* | y_1^* | J ($\text{cm}^{-3}\text{s}^{-1}$) |
|-----------|-------------|-------|-----------------------|---------------------------------------|
| 955 | 39.5 | 240.3 | 1.77×10^{-4} | 2.4×10^9 |
| 956 | 40.0 | 240.9 | 1.95×10^{-4} | 3.2×10^9 |
| 957 | 39.7 | 239.6 | 1.93×10^{-4} | 3.5×10^{10} |
| 964 | 39.5 | 240.2 | 1.94×10^{-4} | 1.3×10^{10} |

Table D.15: Experimental nucleation data of *n*-octane/methane at 40 bar, 240 K. The data are represented in Fig. 6.20.

SYMBOLS

This list of symbols contains the main symbols used in this thesis. Occasionally, the symbols can have a different meaning; this will be explicitly mentioned in the section concerned.

Roman symbols:

| | | |
|--------------|----------------------------------|---|
| a | m^3 | coefficient RKS equation |
| A | m^2 | surface area |
| b | J mol^{-1} | coefficient RKS equation |
| c | m^3 | Peneloux correction |
| c | m s^{-1} | speed of sound |
| c | m^{-3} | equilibrium cluster concentration |
| C | m^{-3} | actual cluster concentration |
| C_{ext} | m^2 | extinction cross section |
| c_p | $\text{J kg}^{-1} \text{K}^{-1}$ | isobaric specific heat |
| c_v | $\text{J kg}^{-1} \text{K}^{-1}$ | isochoric specific heat |
| D | $\text{m}^2 \text{s}^{-1}$ | diffusion coefficient |
| \mathbf{D} | J | tensor with second derivatives of free energy |
| F | J | Helmholtz free energy |
| G | J | Gibbs free energy |
| ΔG | J | Gibbs free energy of droplet formation |
| i | J kg^{-1} | specific enthalpy |
| i | – | number of molecules of component 1 |
| I | $\text{J m}^{-2} \text{s}^{-1}$ | irradiance |
| j | – | number of molecules of component 2 |
| J | $\text{cm}^{-3} \text{s}^{-1}$ | nucleation rate |
| J^\pm | m s^{-1} | Riemann invariants |
| k | m^{-1} | wave number |
| K | $\text{cm}^{-3} \text{s}^{-1}$ | kinetic prefactor |
| k_b | J K^{-1} | Boltzmann's constant |
| k_{ij} | – | interaction parameter |
| Kn | – | Knudsen number |
| l | m | molecular mean free path |
| L | J kg^{-1} | latent heat of evaporation |
| m | – | refractive index |
| m | kg | (molecular) mass |
| M | kg s^{-1} | rate of mass transfer to a droplet |
| M_s | – | shock Mach number |

| | | |
|--------------|--|--|
| n | – | number of molecules |
| n_d | m^{-3} | droplet concentration |
| n_i^* | – | number of excess molecules in critical cluster |
| N | – | number of monomers in gas |
| N_A | mol^{-1} | Avogadro's number |
| Nu_M | – | Nusselt number for mass transfer to a droplet |
| Nu_Q | – | Nusselt number for heat transfer to a droplet |
| p | Pa | pressure |
| P | $\text{kg}^{1/4} \text{m}^3 \text{s}^{-1/2} \text{mol}^{-1}$ | parachor |
| P_s | J s^{-1} | scattered power |
| Q | J s^{-1} | rate of heat transfer to a droplet |
| Q_{int} | J s^{-1} | rate of heat transfer into a droplet |
| Q_{ext} | – | extinction efficiency |
| r | m | droplet radius |
| R | $\text{J mol}^{-1} \text{K}^{-1}$ | universal gas constant |
| \mathbf{R} | s^{-1} | growth rate tensor |
| R_{av} | s^{-1} | average growth rate |
| s | $\text{J kg}^{-1} \text{K}$ | specific entropy |
| S | – | saturation ratio |
| S | J K^{-1} | entropy |
| t | s | time |
| Δt | s | nucleation pulse duration |
| T | K | temperature |
| u | m s^{-1} | flow speed |
| v | m^3 | molecular volume |
| V | m^3 | volume |
| V | $\text{m}^3 \text{mol}^{-1}$ | molar volume |
| V_{RKS} | m^3 | molar volume in RKS equation |
| W | m^{-2} | width factor |
| x | m | space coordinate |
| x_i | – | liquid fraction |
| y | m | space coordinate |
| y_i | – | vapour fraction |
| x | m | space coordinate |
| Z | – | Zeldovich factor |
| Z | – | compressibility factor |
| Z_{RA} | – | Rackett compressibility factor |

Greek symbols:

| | | |
|----------|-------------------------------|-----------------------|
| α | – | “cooling coefficient” |
| α | – | size parameter |
| β | $\text{m}^{-2} \text{s}^{-1}$ | impingement rate |

| | | |
|------------|---|--|
| β | m^{-1} | extinction coefficient |
| γ | – | ratio of specific heats |
| γ | $\text{m}^{-2} \text{s}^{-1}$ | evaporation coefficient |
| δ | ° | scattering angle |
| ϵ | – | relative width of size distribution |
| θ | ° | scattering angle |
| κ | $\text{m}^3 \text{kg}^{-1}$ | Gladstone–Dale constant |
| λ | m | wavelength of light |
| λ | $\text{J m}^{-1} \text{s}^{-1} \text{K}^{-1}$ | thermal conductivity |
| μ | J | chemical potential |
| ρ | mol m^{-3} | density |
| σ | N m^{-1} | surface tension |
| φ | – | angle determining direction of saddle point flux |
| ω | – | Pitzer's acentric factor |

Subscripts:

| | |
|-----------|--|
| <i>c</i> | pertains to critical point |
| <i>eq</i> | pertains to thermodynamic equilibrium |
| <i>i</i> | pertains to component <i>i</i> |
| <i>ij</i> | pertains to an (<i>i, j</i>) cluster |
| <i>m</i> | pertains to mixture (RKS equation) |
| 1 | pertains to component 1 |
| 2 | pertains to component 2 |
| ∞ | pertains to far field |

Superscripts:

| | |
|---------------------|--|
| <i>l</i> | pertains to the liquid state |
| <i>s</i> | pertains to the surface layer |
| <i>sp</i> | pertains to the saddle point |
| <i>t</i> | pertains to the total cluster |
| <i>v</i> | pertains to the vapour state |
| * | pertains to the critical nucleus |
| $\hat{}$ | pertains to the state after shock wave passage |
| – | pertains to average |

SUMMARY

Homogeneous nucleation is the first stage of droplet formation in a supersaturated vapour in the absence of foreign condensation nuclei. This thesis describes both the experimental and theoretical study of homogeneous nucleation and the subsequent growth of droplets in the coexistence region of binary mixtures of methane and either *n*-nonane or *n*-octane at pressures up to 40 bar. Since these mixtures exhibit real gas properties at pressures above a few bar, the consequences of these real gas properties for nucleation received special attention.

The vapour-liquid phase behaviour of a mixture of methane with a small amount of a higher alkane in the gas phase shows a large similarity with the phase behaviour of natural gas of which the main component is also methane. In the $p - T$ phase diagram, at temperatures above the critical temperature of methane a coexistence region exists in which the gas phase can be in thermodynamic equilibrium with the liquid phase. Entering this region from outside the coexistence envelope by a change of the thermodynamic state results in condensation. When the thermodynamic state changes slowly, condensation will occur on the mixture's equilibrium curve or coexistence envelope or very near to it on foreign nuclei or walls. If the change of thermodynamic state proceeds rapidly, for example by a rapid expansion, homogeneous nucleation will occur inside the coexistence region. Now, the supersaturation will be large since the formation of nuclei requires the forming of a droplet surface. This process is energetically unfavourable, and therefore an energy barrier must be passed before droplets are formed. Subsequently, the droplets will continue growing as long as a state of supersaturation is maintained.

A high pressure pulse expansion tube for nucleation and droplet growth studies was designed and built. Actually, this tube is a special shock tube. The site from which nucleation and condensation are observed, is near the end plate of the high pressure section. Reflections of the initial shock wave at a local widening in the low pressure section generates a nucleation pulse at the endwall of the high pressure section. A nucleation pulse is a short time interval in which the supersaturation of the vapour is raised to a level such that considerable nucleation takes place. After the nucleation pulse, droplets grow to macroscopic sizes but without any new droplets to be formed. This is achieved by reducing the supersaturation. An important quantity is the nucleation rate, which is the number of droplets formed per unit time and volume.

Droplet detection was performed by optical means. A light extinction method provided droplet number density, droplet size was measured by a 90° Mie scattering method. Division of the droplet number density by the nucleation pulse duration then yields the nucleation rate.

The performance of the pulse expansion tube was tested by comparing experimental nucleation rates of water and *n*-nonane in nitrogen at low pressures with literature data. A good agreement was found. Measured nucleation rates are of the order of $10^8 - 10^{12} \text{ cm}^{-3}\text{s}^{-1}$. Droplet growth rates were compared with a theoretical model of Gyarmathy. A small deviation between experiment and theory was found; this was attributed to vapour adsorption on the tube walls

which altered the vapour concentration of the mixture.

A thermodynamic droplet model for the calculation of the Gibbs free energy of formation of the critical droplet, based on the Redlich–Kwong–Soave equation of state was formulated. This model was implemented in the Classical Binary Nucleation Theory. Detailed calculations were performed for the mixture *n*-nonane/methane. Raising the pressure at a fixed supersaturation and temperature resulted in an increased amount of methane in the critical droplet, a reduced surface tension, and a strongly increased nucleation rate.

High pressure nucleation experiments were performed for the binary mixtures *n*-nonane/methane and *n*-octane/methane. The nucleation pulse pressure varied from 10 bar to 40 bar, while the nucleation temperature was between 230 K and 250 K. A major experimental difficulty appeared to be the determination of the initial gas composition in the test section of the tube. The problem was solved by comparing measured droplet growth rates with a high pressure limit of a droplet growth model of Gyarmathy. The molar fraction of the heavier hydrocarbon in the mixture was determined by the best fit of the model to the measured growth rate.

The experimental results show a similar view as the calculations according to the classical nucleation theory. At higher pressure and fixed temperature the (critical) supersaturation that corresponds to nucleation rates of the order of $10^8 - 10^{12} \text{ cm}^{-3}\text{s}^{-1}$ declines strongly: this (critical) supersaturation for *n*-nonane at 240 K and 10 bar is about 30, and at 40 bar it is even less than 10. Although this tendency is observed both in theory and experiment, the quantitative agreement between both is quite poor. An improved agreement was found with a new phenomenological model at certain pressures and temperatures, but the improvement was not systematic for all measured data. An estimate of the molecular content of the critical cluster on the basis of the experimental nucleation rates showed an increasing amount of methane with increasing pressure. This confirms once more that homogeneous nucleation at high pressures in the mixtures investigated, has to be considered as a binary nucleation process, which is a direct consequence of real gas behaviour.

SAMENVATTING

Homogene nucleatie is de eerste fase van druppelvorming in een oververzadigde damp waarin geen vreemde condensatiekernen aanwezig zijn. Dit proefschrift geeft zowel een experimentele als theoretische beschrijving van homogene nucleatie en de daaropvolgende druppelgroei bij hoge drukken tot 40 bar, in het coëxistentie gebied van de binaire mengsels *n*-nonaan/methaan en *n*-octaan/methaan. Deze mengsels vertonen afwijkingen van ideaal gas gedrag indien de druk groter is dan enige malen de atmosferische druk. Een belangrijk aspect van het onderzoek betrof de invloed van deze zogenoemde reële gas effecten op het nucleatieproces.

Het damp-vloeistof fase gedrag van een mengsel bestaande uit methaan met een geringe hoeveelheid van een hogere alkaan in de gasfase, vertoont grote gelijkenis met het fase gedrag van aardgas, waarvan methaan ook de belangrijkste component is. In het $p - T$ fase diagram, bij een temperatuur boven de kritische temperatuur van methaan, bestaat een coëxistentie gebied waarin de gas fase in thermodynamisch evenwicht kan zijn met de vloeistof fase. Wanneer de thermodynamische toestand van het gasmengsel binnen dit coëxistentie gebied ligt, zal er condensatie optreden. Als de verandering van de thermodynamische toestand langzaam plaats vindt zal de condensatie optreden op of dichtbij de evenwichtscurve van het mengsel, op wanden of op aanwezige vreemde kernen. Bij een snelle toestandsverandering, bijv. door middel van een snelle expansie, zal homogene condensatie optreden in het coëxistentie gebied. De oververzadiging zal in dit geval hoog zijn omdat de kernvorming de vorming van een druppeloppervlak vereist. Aangezien dit proces energetisch niet gunstig is, moet een energiedrempel worden overwonnen alvorens er druppels worden gevormd. Daarna zullen de druppels verder groeien zolang er een oververzadigde toestand bestaat.

Een puls-expansiebuis voor onderzoek van nucleatie en druppelgroei bij hoge druk is ontworpen en gebouwd. De observatie van nucleatie en druppelgroei vindt plaats dicht bij de eindwand van de hogedruksectie. De expansiebuis is een speciale uitvoering van de schokbuis. Reflecties van de schokgolf aan een lokale verwijding in de lagedruksectie van de buis veroorzaken een nucleatiepuls aan de eindwand van de hogedruksectie. Een nucleatiepuls is een kort tijdsinterval waarin de oververzadiging van de damp zo hoog is dat nucleatie in voldoende mate optreedt. Na de nucleatiepuls zullen de gevormde druppels doorgroeien naar macroscopische afmetingen zonder dat daarbij nieuwe druppels worden gevormd. Dit wordt bereikt door de oververzadiging te verlagen. Een belangrijke grootte die het nucleatieproces kenmerkt is de nucleatiesnelheid. Dit is het aantal druppels dat wordt gevormd per eenheid van tijd en volume.

Detectie van druppels vindt plaats met behulp van optische meettechnieken. De druppelconcentratie wordt gemeten met een op licht-extinctie gebaseerde methode. De druppelgrootte wordt gemeten door middel van Mie-verstrooiing onder 90° . Door de druppelconcentratie te delen door de lengte van de nucleatiepuls wordt de nucleatiesnelheid berekend.

De puls-expansiebuis is getest door de resultaten van lage-druk nucleatie-experimenten van water in stikstof en *n*-nonaan in stikstof te vergelijken met waarden bekend uit de literatuur.

Hierbij werd een goede overeenkomst gevonden. De gemeten nucleatiesnelheden zijn van de grootteorde $10^8 - 10^{12} \text{ cm}^{-3}\text{s}^{-1}$. Druppelgroeisnelheden werden vergeleken met een theoretisch model van Gyarmathy. Hier was sprake van een klein verschil tussen experiment en theorie. Het verschil wordt veroorzaakt door adsorptie van damp op de wanden van de buis, waardoor de dampconcentratie in het mengsel verandert.

Een thermodynamisch druppelmodel voor de berekening van de Gibbs vrije energie nodig voor de vorming van een kritische druppel, gebaseerd op de Redlich-Kwong-Soave toestandsvergelijking, werd opgesteld. Dit model is geïmplementeerd in de binaire klassieke nucleatietheorie. Voor het mengsel *n*-nonaan/methaan zijn gedetailleerde berekeningen gedaan. Uit de resultaten blijkt dat wanneer bij constant gehouden oververzadiging en temperatuur de druk wordt verhoogd, de hoeveelheid opgelost methaan in de druppel toeneemt, de oppervlaktespanning daalt, en de nucleatiesnelheid sterk toeneemt.

Voor de mengsels *n*-nonaan/methaan en *n*-octaan/methaan zijn hoge-druk nucleatie-experimenten verricht. De druk in de nucleatiepuls was hierbij tussen 10 bar en 40 bar, terwijl de nucleatietemperatuur tussen 230 K en 250 K lag. Een belangrijke moeilijkheid bij deze experimenten bleek de bepaling van de beginsamenstelling in de testsectie van de buis te zijn. Dit probleem is opgelost door de gemeten druppelgroeisnelheid te vergelijken met een hoge-druk limiet van het druppelgroeimodel van Gyarmathy. De concentratie van het hoger alkaan werd bepaald door de "best fit" van het model aan de gemeten groeisnelheid.

De experimentele resultaten tonen kwalitatief eenzelfde verloop als de berekeningen volgens de klassieke nucleatietheorie. Bij constante temperatuur en toenemende druk neemt de oververzadiging die nodig is om een nucleatiesnelheid te verkrijgen van de grootte $10^8 - 10^{12} \text{ cm}^{-3}\text{s}^{-1}$ sterk af: Deze (kritische) oververzadiging voor *n*-nonaan bij 240 K en 10 bar is ongeveer 30, voor 40 bar is deze zelfs lager dan 10. Alhoewel deze tendens in experiment en theorie hetzelfde lijkt, is de kwantitatieve overeenkomst vrij slecht. Betere overeenstemming wordt gevonden wanneer het experiment wordt vergeleken met een nieuw fenomenologisch model. De verbetering geldt echter slechts bij enige drukken en temperaturen, en geldt niet systematisch voor het hele onderzochte bereik. Een schatting van het aantal molekulen in het kritische cluster op basis van gemeten nucleatiesnelheden liet zien dat de hoeveelheid methaan in het cluster toeneemt bij hogere druk. Dit bevestigt dat homogene nucleatie bij hoge druk voor de onderzochte mengsels een binair proces is, hetgeen een direct gevolg is van reële gaseigenschappen.

Nawoord

Dit proefschrift is het eindresultaat van mijn vierjarig promotieonderzoek verricht in de vakgroep Transportfysica van de Faculteit der Technische Natuurkunde aan de Technische Universiteit Eindhoven. Hoewel slechts mijn naam op de kaft staat vermeld, is dit werk tot stand gekomen dankzij de inzet van velen. Het is ondoenlijk op deze plaats iedereen die zijn of haar steentje heeft bijgedragen te noemen, echter wil ik enige mensen in het bijzonder danken voor de goede en prettige samenwerking in de afgelopen jaren.

Allereerst betreft dit Rini van Dongen die mij in de gelegenheid heeft gesteld dit onderzoek uit te voeren, en wiens steun en betrokkenheid mij de afgelopen jaren zeer geholpen hebben dit resultaat te bereiken. Verder ben ik dank verschuldigd aan de collega's van de werkeenheid Gasdynamica/aëroakoestiek Harm Jager, Eep van Voorthuisen, Louis Wasser, Bram Wijnands en Jan Willems voor hun grote bijdragen aan het realiseren van de schokbuisopstelling, en voor de vele ideeën om tot een zo goed mogelijk resultaat te komen. Hierbij mogen ook niet ontbreken Marcel Muijtens, Kris Snoeijs, Mico Hirschberg en Vitaly Kalikmanov voor de talloze suggesties, ideeën en discussies op ieder denkbaar gebied.

De afstudeerders Geert Hofmans, Pierre Kriesels en Carlo Luijten hebben allen belangrijke bijgedragen geleverd met hun arbeid, en ook het werk van de stagiair(e)s Wilbert Bosch, Karel-Joop Bosschaart, Eric Commeren, Bart Heiligenberg, Hugo Hendriks, Peter Hesen, Michael Louwers, Rob van Schaijk, Joost Smits, Serge Toussaint, Michèle van der Voorn en Chi-Ho Wong heeft het onderzoek goed vooruit geholpen.

Ik wil tevens bedanken Prof.dr.-ing. F. Peters van de Universität-Gesamthochschule Essen die mij in de gelegenheid heeft gesteld het "nucleatie vak" te leren in zijn laboratorium.

Tot slot dank ik de promotoren Prof.dr.ir. M.E.H. van Dongen en Prof.dr.ir. P.P.J.M. Schram voor het kritisch doorlezen van het manuscript en voor hun suggesties ter verbetering van dit proefschrift.

Curriculum Vitae

- 1 september 1966 geboren te Heeze
- mei 1984 diploma Atheneum B
Augustinianum Eindhoven
- augustus 1990 diploma Technische Natuurkunde
Technische Universiteit Eindhoven
- januari 1991 –
januari 1995 assistent in opleiding (AIO)
Technische Universiteit Eindhoven
Faculteit der Technische Natuurkunde
vakgroep Transportfysica
- oktober 1991 –
december 1991 verblijf aan de Universität-Gesamthochschule Essen
in de groep van Prof.dr.-ing. F. Peters

Stellingen behorende bij het proefschrift

“Homogeneous nucleation and droplet growth in the coexistence region of *n*-alkane/methane mixtures at high pressures”.

door K.N.H. Looijmans

1. De kritische oververzadiging in het binaire reële gasmengsel *n*-nonaan/methaan waarbij waarneembare homogene nucleatie optreedt, neemt af bij toenemende totaaldruk.

Dit proefschrift.

2. Binaire diffusiecoëfficiënten in gasmengsels bij hoge druk kunnen nauwkeurig worden bepaald in een puls-expansiebuis d.m.v. de meting van druppelgroeisnelheden.
3. Dichtheidsveranderingen van een gas in de adiabatistische kern van een schokbuis kunnen worden bepaald door de afbuiging te meten die een lichtbundel ondergaat welke de buis passeert door twee t.o.v. elkaar niet parallel gesitueerde vensters, zonder dat aanwezige temperatuurgrenslagen de meting beïnvloeden.
4. De door Kalikmanov en Dyadkin beschreven suspensies van hoge T_c -supergeleidende deeltjes kunnen dienen als een modelsysteem voor de studie naar collectieve verschijnselen in de vaste stof fysica.

Kalikmanov V.I. & Dyadkin I.G., (1989), *J. Phys.: Condens. Matter* **1**, 993–997.

Kalikmanov V.I., (1993), *J. Magn. Magn. Mater.* **122**, 154–158.

5. Het is mogelijk gunstige eigenschappen van de puls-expansiebuis en de zuiger-expansiekamer voor nucleatieonderzoek te combineren in een zuiger-expansiebuis.

Meyer K.A.J., (1994), Proefschrift, Universität-Gesamthochschule Essen.

6. De door Clarke en Delale geïntroduceerde “frozen” activiteitsfunctie $B_f(T)$, waarin T de absolute temperatuur is, voor de beschrijving van nucleatie heeft anders dan zij veronderstellen voor water geen fysisch realistisch minimum.

Clarke J.H. & Delale C.F., (1986), *Phys. Fluids* **29**(5), 1398–1413.

Delale C.F., Schnerr G.H., & Zierep J., (1993), *Phys. Fluids A* **5**(11), 2982–2995.

7. Doordat in de recente fenomenologische nucleatietheorieën enigszins willekeurige modelparameters worden ingevoerd die de consistentie verbreken met de clustertheorie van Fisher waarop zij gebaseerd waren, kunnen deze theorieën worden beschouwd als een aanpassing aan experimentele resultaten in een meer-dimensionale parameter-ruimte.

Dillmann A. & Meier G.E.A., (1991), *J. Chem. Phys.* **94**(5), 3872–3884.

Delale C.F. & Meier G.E.A., (1993), *J. Chem. Phys.* **98**(12), 9850–9858.

Laaksonen A., Ford I.J., & Kulmala M., (1994), *Phys. Rev. E* **49**(6), 5517–5524.

8. De beschrijving van de nucleatiekinetiek volgens Katz en Wiedersich kan worden uitgebreid naar binaire systemen.

Katz J.L. & Wiedersich H., (1977), *J. Coll. Int. Sci.* **61**(2), 351–355.

Hofmans G.C.J., (1993), *Afstudeerverslag*, Technische Universiteit Eindhoven.

9. Indien het Nucleatie Theorema beschreven door Oxtoby en Kashchiev wordt gecombineerd met de binaire klassieke nucleatietheorie volgens Wilemski kan de kinetische voorfactor in deze theorie volledig consistent worden berekend.

Oxtoby D.W. & Kashchiev D., (1994), *J. Chem. Phys.* **100**(10), 7665–7671.

Wilemski G., (1987), *J. Phys. Chem.* **91**(10), 2492–2498.

10. Een experimentator doet er goed aan de door de fabrikant opgegeven specificaties van geleverde apparatuur te wantrouwen.

Eindhoven, 16 mei 1995